Ghent University

Faculty of Sciences

Department of Inorganic and Physical Chemistry

Near Infrared Heteronanocrystals with Enhanced Electro-Optical Properties: from Synthesis to Layer Formation.

Yolanda Justo

Promotor: Prof. Dr. Ir. Z. Hens

Thesis submitted in fulfillment of the requirements of
the degree of Doctor of Science: Chemistry
2012

Promotor:

Prof. dr. ir. Zeger Hens

Jury:

Prof. dr. Annemie Adriaens (chairman)	Ghent University
Prof. dr. ir. Zeger Hens (promotor)	Ghent University
Prof. dr. Dirk Poelman	Ghent University
Prof. dr. Rik Van Deun	Ghent University
Prof. dr. Daniël Vanmaekelbergh	Utrecht University
Prof. dr. ir. Dries Van Thourhout	Ghent University
Prof. dr. ir. Edouard Brainis	Ghent University
Dr. Petra Lommens	Ghent University

Ghent University
Faculty of Sciences
Department of Inorganic and Physical Chemistry
Krijgslaan 281–S3
9000 Ghent
BELGIUM

UNIVERSITEIT GENT

Thesis submitted in fulfillment
of the requirements of the degree of
Doctor of Science: Chemistry
2012

Contents

List of Acronyms

AFM	Atomic force microscopy
BuOH	Butanol
CdOA	Cadmium oleate
DBTJ	Double barrier tunnel junction
DDT	Dodecanethiol
EDS	Energy-dispersive x-ray spectroscopy
EtOH	Ethanol
f	Volume fraction
$f_{if,abs}$	Absorption oscillator strength
$f_{if,em}$	Emission oscillator strength
FFT	Fast Fourier transform
f_{LF}	Local field factor
HAADF	High angle annular dark field
HR-TEM	High-resolution transmission electron microscopy
ICP-MS	Inductively coupled plasma mass spectrometry
IPA	Isopropanol
LB	Langmuir-Blodgett
LS	Langmuir-Schaefer
LED	Light emitting diode
μ_i	Intrinsic absorption coffcient
MeOH	Methanol
MV^{2+}	Methyl viologen
NC	Nanocrystal
NIR	Near infrared
NMR	Nuclear magnetic resonance
OA	Oleic acid
ODE	n-Octadecene
OLA	Oleylamine
PbX	lead chalcogenides

PLQY	Photoluminescence quantum yield
Q-CdSe	CdSe nanocrystal(s)
QD	Quantum dot
Q-InP	InP nanocrystal(s)
Q-PbSe	PbSe nanocrystal(s)
QR	Quantum rod
QY	Quantum yield
SILAR	Successive ionic layer addition and reaction
STEM	Scanning transmission electron microscopy
STM	Scanning transmission microscopy
STS	Scanning tunneling spectroscopy
TBP	Tributylphosphine
TEM	Transmission electron microscopy
TOP	Tri-*n*-octylphosphine
TOPO	Tri-*n*-octylphosphine oxide
UHV	Ultra high vacuum
UPS	Ultraviolet Photoemission Spectroscopy
XPS	X-ray photoelectron spectroscopy
XRD	X-ray diffraction

Chapter I

Introduction

1.1 Quantum dots

Nanoscale materials frequently show behavior which is intermediate between that of a macroscopic solid and that of an atomic or molecular system. Since the number of atoms on the crystals surface is a significant fraction of the total number of atoms, thermodynamic properties such as the melting point or the solubility in a certain solvent will depend on the diameter of a nanocrystal. A second example, relevant to this work, is the quantum size effect that occurs in semiconductor nanocrystals.[1] Size quantization can be most easily understood using the particle-in-a-box model, where a particle with mass m is confined in an infinite potential well with width L.[2] According to the Schroedinger equation, such a particle has discrete energy levels E_n, given by:

$$E_n = \frac{\hbar\pi^2}{2mL^2}n^2 \tag{1.1}$$

The equation shows that a reduction of the width of the well leads to an increase of the energy of a particle. For a particle with a mass of 0.1 m_e (a typical value for electrons in semiconductors), equation 1.1 predicts a confinement energy of 15 meV for a 5 nm well, which indicates that quantum confinement can strongly affect the energy levels in semiconductor nanocrystals. An expression for the size-dependence of the band gap of a semiconductor nanocrystals was derived in 1984 by Brus, who considered both the quantization of the electron and hole energy levels and the Coulomb attraction between electron and hole:[3]

$$E_g(QD) = E_g + \frac{\hbar^2\pi^2}{2\mu_{ex}R^2} - \frac{1.786e^2}{\epsilon R} \tag{1.2}$$

Here, R is the particle radius, μ_{ex} is the reduced exciton effective mass and ϵ the dielectric constant of the semiconductor. This equation highlights a major advantage of semiconductor nanocrystals, also known as quantum dots (QDs). Due to the dependence of the band gap on the nanocrystal radius R, optical properties can be tuned over a wide spectral range by merely varying the size of the particles. The minimum energy needed to create an electron-hole pair in a QD (an" exciton") is defined by its band gap (E_g). Light with energy lower than E_g cannot be absorbed by the QD. Since the band gap depends on the size of the QD, the onset of absorption is also size dependent.[4,5] In figure 1.1a we show a series of absorption spectra of PbSe QDs with different sizes ranging form 4 to 7 nm. The smaller QDs have an absorption spectrum that is shifted to shorter wavelengths with respect to larger QDs and to the bulk material. The position of the luminescence peak is also dependent on the average QD size. This is demonstrated by the size-dependent luminescence of colloidal CdSe QDs (figure 1.1b), which shifts from red (largest particles) to blue (smallest particles) by reducing the particle diameter from 6 to 2 nm.

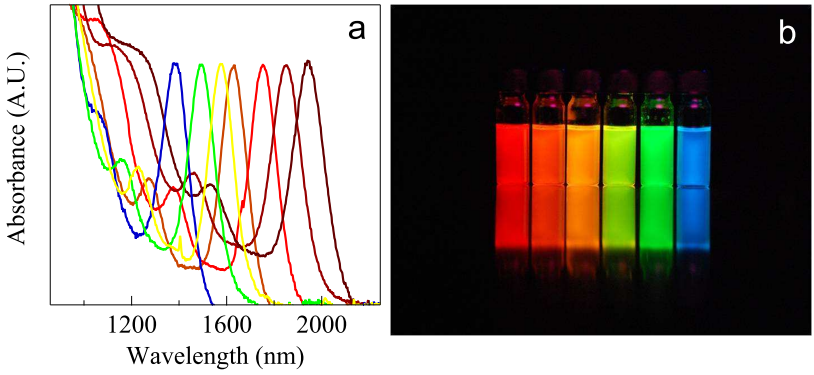

Figure 1.1: a) Series of PbSe QDs absorption spectra with sizes from 4 to 7 nm. b) Suspensions of luminescent CdSe QDs between 2 and 6 nm under UV light.

Depending on the band gap of the bulk material (table 1.1), the band gap of quantum dots can be tuned from the ultra violet to the

material	symbol	band gap (eV)
silicon	Si	1.11
germanium	Ge	0.67
silicon carbide	SiC	2.86
gallium(III) arsenide	GaAs	1.43
indium (III) phosphide	InP	1.35
zinc oxide	ZnO	3.37
zinc sulfide	ZnS	3.6
zinc selenide	ZnSe	2.7
zinc telluride	ZnTe	2.25
cadmium sulfide	CdS	2.42
cadmium selenide	CdSe	1.73
cadmium telluride	CdTe	1.49
lead (II) sulfide	PbS	0.37
lead (II) selenide	PbSe	0.26
lead (II) telluride	PbTe	0.31

Table 1.1: Electronic band gaps for different materials.

infrared part of the electromagnetic spectrum. This work focuses on QDs active in the infra red, with emission wavelengths between 800 and 2500 nm. Applications operating in this wavelength range involve for example optical data communication,[6] bio-imaging,[7] photovoltaics[8] or photodetection.[9] Key assets of colloidal QDs for all these applications are the tunability of their optical properties and their suitability for solution based processing.

1.2 Lead chalcogenide quantum dots

Among the different near infrared (NIR) active QDs, this work is focused on IV-VI lead chalcogenides (PbX, X=S, Se, Te). Bulk PbX have the rocksalt crystal structure. They are direct semiconductors with a bandgap ranging from 0.4 (PbS) to 0.25 (PbTe) eV.[10] Opposite from most III-V and II-VI semiconductors, their band gap lies at the L point instead of the Γ point of the Brillouin zone (figure 1.2a). Due to the low effective mass of both electron and hole, PbX show considerable size quantization, providing access to an exceptionally wide wavelength range (800 to 3000 nm).

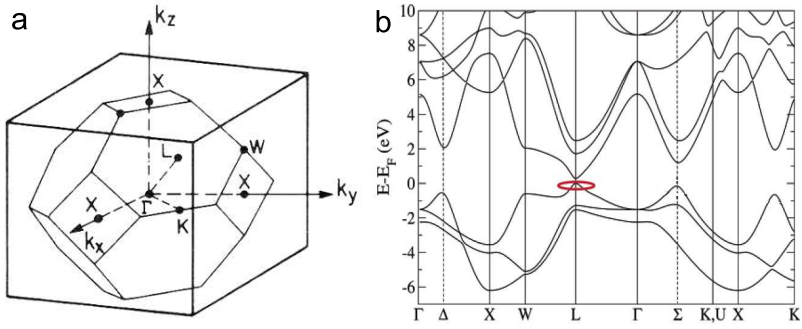

Figure 1.2: a)First Brillouin Zone for a face-centered cubic crystal lattice. b)Band structure for bulk PbSe with fundamental bandgap located at L-point.

Since size quantization occurs around the 4 L points of the Brillouin zone (figure 1.2b), the resulting first electron ($1S_e$) and hole ($1S_h$) levels are both 8-fold degenerate (including spin degeneracy) with PbX QDs. Optical gain or population inversion will therefore require 4 electron-hole pairs (excitons) in a quantum dot as compared to only one with II-VI semiconductors like CdSe.[11] This is a considerable complication since Auger recombination is a very efficient, non-radiative decay path for multiple excitons in semiconductor nanocrystals. As a result, the gain lifetime is limited to the 1-10 ps range.[12]

To overcome the limitations Auger recombination of multiple excitons imposes on optical gain with PbX QDs, one could either try to reduce the Auger rate or to lift the degeneracy of the exciton states. Reducing the Auger rate can be achieved by modifying the QD geometry[13] - larger volumes - or by the growth of core/shell heterostructures with a thick shell[14,15] and an alloyed core/shell interface as was recently demonstrated for CdZnSe/ZnSe QDs.[16] Alternatively, a so-called type II band alignment (see section 1.3) in core/shell heterostructures has been shown the lift the degeneracy of the exciton levels in the sense that the creating a biexciton requires higher energy photons than a single exciton.[17,18] These approaches – typically developed and demonstrated for II-VI QDs active in the visible – have inspired most of the synthetic work in this study.

1.3 Synthesis

The colloidal synthesis of semiconductor nanocrystals has experienced an enormous development in the past two decades. Especially the *hot injection synthesis* developed by Murray, Norris and Bawendi in 1993[5] has evolved in a method that gives access to a wide range of particles with exceptional control over their size and shape. This synthesis is based on the pyrolysis of metal-organic precursors in a hot solvents (120℃-360℃) in the presence of coordinating species. Based on the concept put forward by La Mer and Dinegar,[19] the method is based on the formation of a supersaturated reaction mixture by the rapid generation of solution-phase monomers out of the injected precursors. The supersaturation initiates a homogeneous nucleation and growth process that results under specific synthesis conditions in a monodisperse nanocrystal colloid. A scheme of the synthesis concept and an actual setup to execute a hot injection synthesis are represented in figure 1.3.

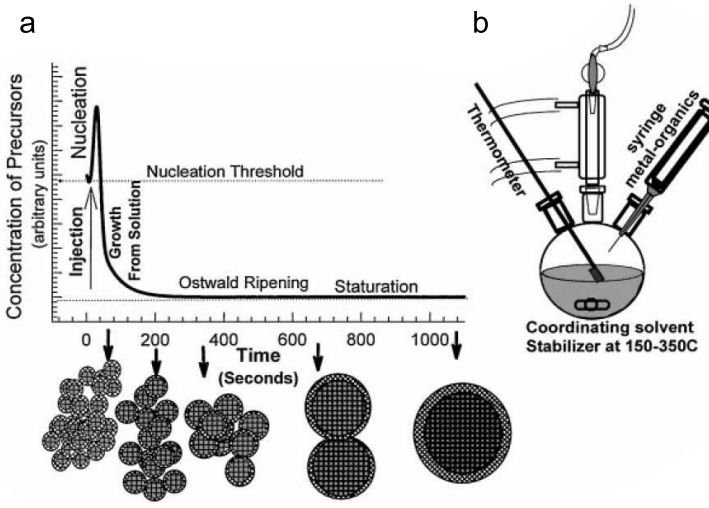

Figure 1.3: a) Scheme illustrating La Mer's model for nucleation ond growth of monodisperse colloidel QDs. b) Representation of the set-up used for QDs synthesis. Figure reprinted from Murray, C. B., Kagan, C. R., Bawendi, M. G., *Annu. Rev. Mater. Sci.*, 30, 545, 2000.

Understanding and controlling the hot injection synthesis to obtain nanocrystals with predefined sizes or shapes at low size dispersion and high chemical yield is still an area of active research.

This is however not addressed in this work. Focusing on the formation of heteronanocrystals, we adapted existing literature recipes to synthesize the initial core nanocrystals, such as quasi spherical PbX[20–22] and rod-shaped CdS nanocrystals,[23] with the practical aim of expanding the accessible size range and reducing the size dispersion.

1.4 Quantum dot heterostructures

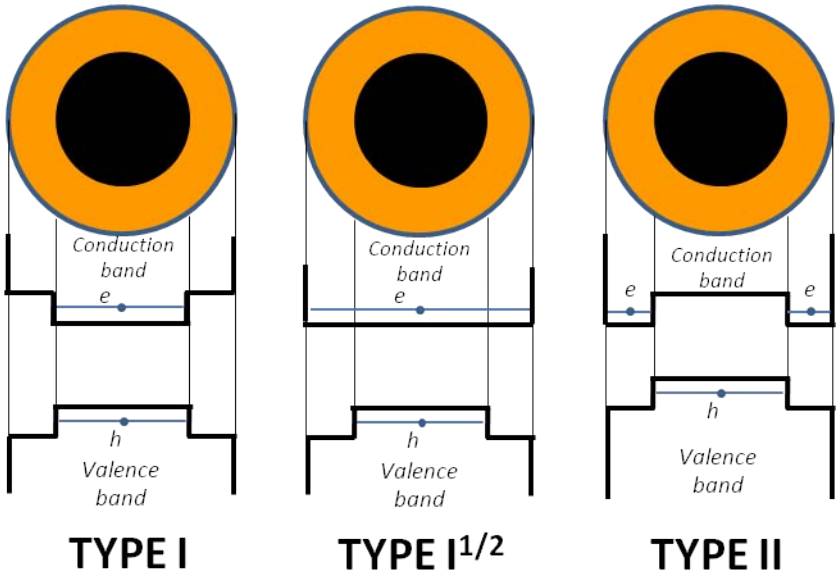

Figure 1.4: Schematic representation of the limiting charge carrier localization regimes in quantum dots core/shell heterostructures.

The ability to tune opto-electronic properties by the design of a nanocrystal can be expanded beyond size and shape effects by the formation of quantum dot heterostructures.[24] These are nanoscale objects consisting of at least two inorganic materials, for example in a concentric core/shell structure. The additional tunability in such a heteronanocrystal is imparted by the energy offsets between the valence and conduction band in both materials.[15] In the case of a core/shell structure, three different regimes of band alignment can be identified, often called type-I, type-I$^{1/2}$ and type-II. (figure 1.4)

Type I. In a type I structure, the energy bands of the shell material encompass those of the core material. As a result, an exciton remains confined within the core area and the emission energy is determined by the energy gap of the core material. Type I alignment is typically used to passivate the surface of the core QD with the goal of improving the photoluminescence quantum yield and enhancing the chemical stability of the material. A typical example of a type I structure is CdSe/ZnS.[25]

Type II. In this case, the core and the shell have staggered energy bands. As a result, an exciton will consist of spatially separated charge carriers, with one carrier mostly confined in the core, while the other is mostly confined in the shell. As compared to type I alignment, this offers an extensive tunability of the electro-optical properties which now depend both on the size of the core and the thickness of the shell. In addition, type II QDs are more suitable for photovoltaic or photoconduction applications. A typical type II core/shell nanocrystal is ZnSe/CdS.[26]

Type $I^{1/2}$. In this case, the energy offset for one of the charge carriers is too small to confine it to the core. As a consequence, one of the charge carriers will delocalize over core and shell, while the other remains confined in the core. A typical example of a type $I^{1/2}$ nanocrystal is CdSe/CdS.[27]

1.5 Quantum dot deposition

The current know-how on colloidal QDs synthesis allows for an extensive control over their size and shape.[20,28,29] Moreover, optoelectronic properties of the QDs can be engineered in view of the application. Nowadays, increasing number of research groups are taking advantage of the unique nanocrystal properties by implementing them in devices used for a broad range of applications. For example, different colloidal QDs have been successfully incorporated in efficient nanocrystal light-emitting devices[30–32] and in

field-effect transistors,[33] while Au nanocrystals have been used as catalysts for nanowire growth[34] or in sensing applications.[35] Such implementation often requires deposition of a thin film or a monolayer of nanocrystals on top of a substrate. Typically, this is achieved by techniques like drop-casting,[36] spin-coating,[30,37] Langmuir-Blodgett[38–40] (LB) and Langmuir-Schaefer[41] (LS) deposition, or layer-by-layer deposition.[42] All the different techniques have their advantages and disadvantages but among all of them, this work is focused on LB and LS depositions. These techniques have the advantage that they enable the deposition of densely packed monolayers with local ordering of QDs on almost any kind of substrate, ranging from hydrophilic mica to hydrophobic silicon and an accurate control over the thickness of the shell.

1.6 Outline of the thesis

This work is divided in eight chapters:

In chapter I, we give a general introduction about semiconductor nanocrystals, focusing on lead chalcogenides quantum dots. We also describe the synthesis method for colloidal quantum dots and how we can extend their opto-electronic properties by creating core/shell heterostructures. Finally we depict the different deposition techniques.

In chapter II, we adapt the PbS QDs synthesis described by Cademartiri *et al.* by employing TOP. This new addition extends the range of PbS QDs sizes, leading to monodisperse suspensions with an average size between 3 and 10 nm.

In chapter III, we explore the possibilities of the cationic exchange reaction to develop PbX heterostructures. We study the influence of each reaction parameter upon the thickness of the shell. Moreover, we try to find the reaction mechanism that fits better with our results.

In chapters IV and V, we study the opto-electronic properties of PbSe/CdSe and PbS/CdS QDs respectively. This includes, absorption and emission oscillator strength, intrinsic absorption

coefficient, photoluminescence quantum yield, photoluminescence lifetime and Stokes shift.

In chapter VI, we analyze the monolayer formation of PbS and PbSe cores and PbSe/CdSe core/shell QDs using Langmuir-Blodgett (LB) deposition and we compare the photoluminescence properties of these LB films.

In chapter VII, we take advantage of the excellent quality of the LB films to study the formation of different QD mono and multilayers and use them for analyzing the properties of QDs in close packed films.

In chapter VIII, we use successive cationic exchange steps to synthesize colloidal PbS/CdS heterorods with high photoluminescence quantum yield in the near infrared out of CdS quantum rods (QRs). The obtained heterostructures are formed by several PbS QDs inside of a CdS QR. The number of QDs inside depends on the length of the QRs.

Bibliography

[1] Reed, M. A.; Aggarwal, R. J.; Matyi, R. J.; Moore, T. M.; Wetsel, A. E. Observation of Discrete Electronic States in a Zero-Dimensional Semiconductor Nanostructure. *Phys. Rev. B* **1988**, *60*, 535–537.

[2] Kippeny, T.; Swafford, L. a.; Rosenthal, S. J. Semiconductor Nanocrystals: A Powerful Visual Aid for Introducing the Particle in a Box. *Journal of Chemical Education* **2002**, *79*, 1094.

[3] Brus, L. Electronic wave functions in semiconductor clusters: experiment and theory. *The Journal of Physical Chemistry* **1986**, *90*, 2555–2560.

[4] Bawendi, M. G.; Steigerwald, M. L.; Brus, L. E. The Quantum-Mechanics of Larger Semiconductor Clusters (Quantum Dots). *Annu. Rev. Phys. Chem.* **1990**, *41*, 477–496.

[5] Murray, C.; Norris, D. J.; Bawendi, M. G. Synthesis and Characterization of Nearly Monodisperse CdE (E = S, Se, Te) Semiconductor Nanocrystallites. *J* **1993**, *115*, 8706–8715.

[6] Zhukov, a. E.; Kovsh, a. R. Quantum dot diode lasers for optical communication systems. *Quantum Electronics* **2008**, *38*, 409–423.

[7] Medintz, I. L.; Uyeda, H. T.; Goldman, E. R.; Mattoussi, H. Quantum dot bioconjugates for imaging, labelling and sensing. *Nature materials* **2005**, *4*, 435–46.

[8] Sargent, E. H. Infrared photovoltaics made by solution processing. *Nature Photonics* **2009**, *3*, 325–331.

[9] Konstantatos, G.; Clifford, J.; Levina, L.; Sargent, E. H. Sensitive solution-processed visible-wavelength photodetectors. *Nature Photonics* **2007**, *1*, 531–534.

[10] Svane, a.; Christensen, N.; Cardona, M.; Chantis, a.; van Schilfgaarde, M.; Kotani, T. Quasiparticle self-consistent GW calculations for PbS, PbSe, and PbTe: Band structure and pressure coefficients. *Physical Review B* **2010**, *81*, 1–10.

[11] Efros, A.; Rosen, M.; Kuno, M.; Nirmal, M.; Norris, D.; Bawendi, M. Band-edge exciton in quantum dots of semiconductors with a degenerate valence band: Dark and bright exciton states. *Physical review. B, Condensed matter* **1996**,

54, 4843–4856.

[12] Murphy, J. E.; Beard, M. C.; Norman, A. G.; Ahrenkiel, S. P.; Johnson, J. C.; Yu, P.; Mićić, O. I.; Ellingson, R. J.; Nozik, A. J. PbTe colloidal nanocrystals: synthesis, characterization, and multiple exciton generation. *Journal of the American Chemical Society* **2006**, *128*, 3241–7.

[13] Htoon, H.; Hollingsworth, J.; Dickerson, R.; Klimov, V. Effect of Zero- to One-Dimensional Transformation on Multiparticle Auger Recombination in Semiconductor Quantum Rods. *Physical Review Letters* **2003**, *91*, 1–4.

[14] Nanda, J.; Ivanov, S.; Achermann, M.; Bezel, I.; Piryatinski, a.; Klimov, V. Light Amplification in the Single-Exciton Regime Using Exciton-Exciton Repulsion in Type-II Nanocrystal Quantum Dots. *Journal of Physical Chemistry C* **2007**, *111*, 15382–15390.

[15] De Geyter, B.; Justo, Y.; Moreels, I.; Lambert, K.; Smet, P. F.; Van Thourhout, D.; Houtepen, A. J.; Grodzinska, D.; de Mello Donega, C.; Meijerink, A.; Vanmaekelbergh, D.; Hens, Z. The different nature of band edge absorption and emission in colloidal PbSe/CdSe core/shell quantum dots. *ACS nano* **2011**, *5*, 58–66.

[16] Wang, X.; Ren, X.; Kahen, K.; Hahn, M. a.; Rajeswaran, M.; Maccagnano-Zacher, S.; Silcox, J.; Cragg, G. E.; Efros, A. L.; Krauss, T. D. Non-blinking semiconductor nanocrystals. *Nature* **2009**, *459*, 686–9.

[17] Chen, Y.; Vela, J.; Htoon, H.; Casson, J. L.; Werder, D. J.; Bussian, D. a.; Klimov, V. I.; Hollingsworth, J. a. "Giant" multishell CdSe nanocrystal quantum dots with suppressed blinking. *Journal of the American Chemical Society* **2008**, *130*, 5026–7.

[18] Vela, J.; Htoon, H.; Chen, Y.; Park, Y.-s.; Ghosh, Y.; Peter, M.; Werner, J. H.; Wells, N. P.; Casson, J. L.; Jennifer, A. Effect of shell thickness and composition on blinking suppression and the blinking mechanism in giant CdSe/CdS nanocrystal quantum dots. *J Biophotonics* **2011**, *3*, 706–717.

[19] La Mer, V. K.; Dinegar, R. H. Theory, Production and Mechanism of Formation of Monodispersed Hydrosols. *Journal of the American Chemical Society* **1950**, *72*, 4847–4854.

[20] Murray, C. B.; Sun, S. H.; Gaschler, W.; Doyle, H.; Bet-

ley, T. A.; Kagan, C. R. Colloidal synthesis of nanocrystals and nanocrystal superlattices. *Ibm Journal of Research and Development* **2001**, *45*, 47–56.

[21] Cademartiri, L.; Bertolotti, J.; Sapienza, R.; Wiersma, D. S.; von Freymann, G.; Ozin, G. a. Multigram scale, solventless, and diffusion-controlled route to highly monodisperse PbS nanocrystals. *The journal of physical chemistry. B* **2006**, *110*, 671–3.

[22] Moreels, I.; Justo, Y.; De Geyter, B.; Haustraete, K.; Martins, J. C.; Hens, Z. Size-Tunable, Bright, and Stable PbS Quantum Dots: A Surface Chemistry Study. *ACS Nano* **2011**, *5*, 2004–2012.

[23] Carbone, L. et al. Synthesis and micrometer-scale assembly of colloidal CdSe/CdS nanorods prepared by a seeded growth approach. *Nano letters* **2007**, *7*, 2942–50.

[24] de Mello Donegá, C. Synthesis and properties of colloidal heteronanocrystals. *Chemical Society reviews* **2011**, *40*, 1512–46.

[25] Dabbousi, B. O.; RodriguezViejo, J.; Mikulec, F. V.; Heine, J. R.; Mattoussi, H.; Ober, R.; Jensen, K. F.; Bawendi, M. G. (Cdse)Zns Core-Shell Quantum Dots: Synthesis and Characterization of a Size Series of Highly Luminescent Nanocrystallites. *J. Phys. Chem. B* **1997**, *101*, 9463–9475.

[26] Nemchinov, A.; Kirsanova, M.; Hewa-Kasakarage, N. N.; Zamkov, M. Synthesis and Characterization of Type II ZnSe/CdS Core/Shell Nanocrystals. *Journal of Physical Chemistry C* **2008**, *112*, 9301–9307.

[27] Li, J. J.; Wang, Y. A.; Guo, W.; Keay, J. C.; Mishima, T. D.; Johnson, M. B.; Peng, X. Large-Scale Synthesis of Nearly Monodisperse CdSe / CdS Core / Shell Nanocrystals Using Air-Stable Reagents via Successive Ion Layer Adsorption and Reaction. *J. Am. Chem. Soc.* **2003**, 933–937.

[28] Green, M. S olution routes to III V semiconductor quantum dots q. *Current Opinion in Solid State and Materials Science* **2002**, *6*, 355–363.

[29] Masala, O.; Seshadri, R. Synthesis Routes for Large Volumes of Nanoparticles. *Annual Review of Materials Research* **2004**, *34*, 41–81.

[30] Coe, S.; Woo, W.-K.; Bawendi, M.; Bulović, V. Electrolumi-

nescence from single monolayers of nanocrystals in molecular organic devices. *Nature* **2002**, *420*, 3–6.

[31] Coe-Sullivan, S.; Steckel, J. S.; Woo, W.-K.; Bawendi, M. G.; Bulović, V. Large-Area Ordered Quantum-Dot Monolayers via Phase Separation During Spin-Casting. *Advanced Functional Materials* **2005**, *15*, 1117–1124.

[32] Sargent, E. H. Infrared quantum dots. *Advanced Materials* **2005**, *17*, 515–522.

[33] Talapin, D. V.; Murray, C. B. PbSe nanocrystal solids for n- and p-channel thin film field-effect transistors. *Science* **2005**, *310*, 86–9.

[34] Huang, J.; Tao, A. R.; Connor, S.; He, R.; Yang, P. A general method for assembling single colloidal particle lines. *Nano letters* **2006**, *6*, 524–9.

[35] Nath, N.; Chilkoti, A. A colorimetric gold nanoparticle sensor to interrogate biomolecular interactions in real time on a surface. *Analytical chemistry* **2002**, *74*, 504–9.

[36] Lin, X. M.; Jaeger, H. M.; Sorensen, C. M.; Klabunde, K. J. Formation of Long-Range-Ordered Nanocrystal Superlattices on Silicon Nitride Substrates. *The Journal of Physical Chemistry B* **2001**, *105*, 3353–3357.

[37] Roither, J.; Heiss, W.; Talapin, D. V.; Gaponik, N.; Eychmuller, a. Highly directional emission from colloidally synthesized nanocrystals in vertical cavities with small mode spacing. *Applied Physics Letters* **2004**, *84*, 2223.

[38] Meldrum, F. C.; Kotov, N. A.; Fendler, J. H. Utilization of Surfactant-Stabilized Colloidal Silver Nanocrystallites in the Construction of Mono- and Multiparticulate Langmuir-Blodgett Films. *Langmuir* **1994**, *10*, 2035–2040.

[39] Lambert, K.; Wittebrood, L.; Moreels, I.; Deresmes, D.; Grandidier, B.; Hens, Z. Langmuir-Blodgett monolayers of InP quantum dots with short chain ligands. *Journal of colloid and interface science* **2006**, *300*, 597–602.

[40] Dabbousi, B. O.; Murray, C. B.; Rubner, M. F.; Bawendi, M. G. Langmuir-blodgett Manipulation of Size-selected Cdse Nanocrystallites. *Chemistry of Materials* **1994**, *6*, 216–219.

[41] Lambert, K.; Capek, R. K.; Bodnarchuk, M. I.; Kovalenko, M. V.; Thourhout, D. V.; Heiss, W.; Hens, Z.

Langmuir-Schaefer Deposition of Quantum Dot Multilayers. *Langmuir* **2010**, 6352–6353.

[42] Srivastava, S.; Kotov, N. a. Composite Layer-by-Layer (LBL) assembly with inorganic nanoparticles and nanowires. *Accounts of chemical research* **2008**, *41*, 1831–41.

Chapter II

PbS quantum dots synthesis

2.1 Introduction

Colloidal lead chalcogenide quantum dots (QDs) are an increasingly important class of nanosized materials. High quality PbS,[1,2] PbSe[3] and PbTe[4] can all be synthesized by wet chemistry techniques, which produce suspensions of monodisperse QDs (relative size dispersion $\sigma_d < 10\%$). This enables low-cost wet processing of the QDs and consequently, a variety of devices are currently pursued. PbTe QDs for instance offer prospects for enhanced thermoelectric properties, and substantial progress has been made toward the fabrication of highly conductive n- and p-type thin films.[5,6] Photonic applications involving lead chalcogenide QDs are mostly based on PbS and PbSe: QD based electroluminescent devices,[7,8] lasers,[9] solar cells[10,11] and photodetectors[12,13] have all been demonstrated. In these fields, it is not yet clear whether PbS or PbSe QDs are the more suitable. For instance, photodetectors are often PbS-based.[12,13] In contrast early solar cell applications primarily used PbSe QDs;[10] only recently Tang et al.[14] demonstrated that PbS QDs offer an enhanced stability under ambient conditions and Ma et al.[15] showed that solar cells consisting of PbS_xSe_{1-x} alloyed QDs take advantage of both an improved open circuit voltage and short circuit photocurrent.

From an optical perspective, both the absorption and luminescence properties make the materials equally attractive for photonic devices. They show a similar molar extinction coefficient at the band gap,[16,17] and both materials have a high photoluminescence quantum yield (PLQY). Values for small PbSe QDs vary between

12% and 85%,[18,19] while for PbS QDs a PLQY between 20% and 82% has been reported.[1,2,20–22] PbSe QDs have however practical disadvantages: several studies have already reported on their poor stability in air.[23–25] This is a serious drawback if one wishes to operate PbSe-based devices under ambient atmosphere. In this respect, PbS QDs may offer a suitable alternative to PbSe QDs and hence, a synthesis which produces a large size-range of bright and stable PbS QDs is higly desirable.

For PbS QDs, currently two organic synthesis routes exist. The first route is based on lead oleate reacting with bis(trimethylsilyl) sulfide in octadecene (referred to as the Hines-synthesis from here on).[1] It offers monodisperse QDs over a wide size range (2.6-7.2 nm, corresponding to an absorption peak of 825-1750 nm), and the QDs are bright,[1,20–22] yet not entirely air-stable for all sizes.[26] The second route employs lead chloride ($PbCl_2$) and elemental sulfur (S) in oleylamine (OLA) as precursors, and OLA as the solvent (Cademartiri-synthesis).[2] The available size range is substantially smaller (4.2-6.4 nm, corresponding to an absorption peak of 1200-1600 nm), yet the QDs also have a high PLQY[2] and thin films of these QDs show good optical stability.[27]

In this chapter, we further tune the Cademartiri-synthesis to produce a wide size range of PbS QDs with a high PLQY. To achieve size-tunability, tri-n-octylphosphine (TOP) is added. The resulting QDs have a PLQY of 20%–90%, depending on size. In addition, PbS QDs produced by our modified Cademartiri-synthesis are air-stable over the entire size range studied, in contrast with larger PbS QDs obtained by the Hines-synthesis.[26]

2.2 Experimental

2.2.1 PbS QD synthesis

The PbS QD synthesis is based on the procedure of Cademartiri *et al.*[2] A stock solution of 0.16 g (5 mmole) of S, dissolved in 15 ml of oleylamine (OLA) is prepared by heating the mixture under nitrogen for 30 minutes at 120 °C. For the synthesis, we typically mix 0.834 g (3 mmole) of $PbCl_2$ and 7.5 ml of OLA in a 3-neck flask. This is degassed for 30 minutes under nitrogen at 125 °C. Hereafter, we heat up or cool down the $PbCl_2$ solution to the required injection temperature, and we inject 2.25 ml of the OLA-S stock solution (0.75 mmole of S). The temperature drops approx-

imately 5-10 °C, and the resulting growth temperature is maintained throughout the reaction. After the desired growth time, the reaction is quenched by adding 10 ml of toluene and 15 ml of EtOH. After centrifugation of the suspension and decantation of the supernatant, the QDs are resuspended in 10 ml of toluene. For the samples studied here, the growth temperature is varied between 80 °C and 160 °C, although we have observed that the reaction proceeds even at room temperature. To monitor the QD growth, aliquots are taken at times ranging from 20 seconds up to 2.5 hours.

To investigate the effect of TOP on the synthesis, we repeat all syntheses with 170 µL (375 µmole, half of the amount of S) of TOP added to the 2.25 ml of OLA-S. TOP is added at room temperature and after stirring, the solution has a lighter color. As TOPS is colorless, while OLA-S is dark red, this is taken as evidence that half of the OLA-S is converted to TOPS.

2.2.2 QD characterization

Moreels et al.[17] have shown by means of transmission electron microscopy (TEM) that the PbS QDs are spherical and of uniform size. Relating the TEM diameter to the QD band gap E_0 (eV), measured with absorbance spectroscopy, we have constructed a sizing curve, which enables to determine the size d (nm) directly from the spectral position of the first absorption peak.

$$E_0 = 0.41 + \frac{1}{0.0252d^2 + 0.283d} \tag{2.1}$$

In addition, the QD molar extinction coefficient ϵ was determined. Its value at 400 nm ϵ_{400} is used to calculate the QD concentration c_0 directly from the absorbance at 400 nm A_{400} using Beer's law: $A = \epsilon.c_0.L$ (L: sample length).

$$\epsilon_{400} = 0.0234\, d^3 \quad \mathrm{cm}^{-1}/\mu\mathrm{M} \tag{2.2}$$

Samples for absorbance spectroscopy are prepared by drying a known amount of QDs and suspending them in tetrachloroethylene (C_2Cl_4).

To determine the synthesis yield, aliquots are weighed (mass: M_{aliq}) in order to calculate the amount taken from the synthesis (total mass of the synthesis: M_{tot}). After workup the QDs are suspended in a known volume V_{abs} and c_0 is determined. Taking

the PbS lattice constant a and Pb/S ratio R of the QDs into account ($R = 1.26$),[17] the number of S-atoms per QD is known and the synthesis yield Y_S, related to the amount of sulfur N_S injected, can be calculated.

$$Y_S = \frac{M_{\text{tot}}}{M_{\text{aliq}}} . V_{\text{abs}} . \frac{A_{400}}{\epsilon_{400} . L} . \frac{4\pi}{3} \left(\frac{d}{a}\right)^3 . \frac{1}{1+R} \frac{1}{N_S} \tag{2.3}$$

2.2.3 Ligand exchange

After synthesis, we observed that the QDs cannot be precipitated and resuspended more than once. A turbid suspension results, probably indicating a loss of ligands and subsequent PbS QD clustering. The OLA ligands can however easily be replaced. An exchange to OA is typically performed by adding OA to a toluene suspension of PbS QDs in a ratio of 1.5:10 OA:toluene. After precipitation with EtOH and centrifugation, the QDs are resuspended in toluene and the exchange is repeated. Finally, the QDs are precipitated one more time with EtOH to remove any excess OA. After capping exchange, the QDs can be precipitated several times, suggesting a successful exchange of the capping to OA.

2.2.4 Luminescence measurements

The steady-state photoluminescence is measured using an Edinburgh Instruments FS920 PL setup. Samples are prepared by drying a known amount of PbS QDs, followed by resuspension in 4 ml of C_2Cl_4. The absorbance at the band gap is kept below $0.05\,\text{cm}^{-1}$ to avoid reabsorption of the emitted light. The samples are excited at 400 nm using a 450 W Xenon lamp, coupled to a monochromator. The emitted light is detected using a liquid N_2 cooled Ge-detector, coupled to a monochromator. The Ge-detector limits the wavelength range to *ca.* 1700 nm, as such, we are only able to determine the PL spectrum of QDs up to 6 nm. The emission slits are set to a wavelength resolution of 3 nm. The stability of the excitation lamp and setup is checked by measuring the same sample at the beginning and at the end of the measurements. The difference between both spectra is typically less than 1%. The emitted photon flux F_λ at a given wavelength λ (nm) is corrected for detector and grating efficiency, and converted to an

flux F_{eV} on an energy scale (eV):

$$F_{eV} = F_{\lambda}\frac{\lambda^2}{1239.85} \tag{2.4}$$

The resulting F_{eV}-spectra are fitted using a sum of two Gaussian curves. The total emitted photon flux Φ_{QD} equals the area under these curves.

The photoluminescence quantum yield is defined as the ratio of the number of emitted photons to that of absorbed photons as follows.

$$\mathrm{QY}_{sample} = \frac{\text{number of photons emitted}}{\text{number of photons absorbed}} \tag{2.5}$$

We determine the PLQY by means of an integrating sphere, which is a hollow sphere that has its inner surface coated with a diffusely reflecting material. When a light-source is placed in an ideal integrating sphere, the light is redistributed isotropically over the sphere interior-surface regardless of the angular dependence of the emission. For one QD sample (the reference), we determine the PLQY (QY_{ref}) directly using the calibrated integrating sphere.[28,29] For the other samples the PLQY (QY_{sample}) is calculated relative to this reference sample, taking their respective sample transmittance T into account:

$$\mathrm{QY}_{sample} = \mathrm{QY}_{ref}\frac{\Phi_{QD,sample}}{\Phi_{QD,ref}}\frac{1-T_{ref}}{1-T_{sample}} \tag{2.6}$$

2.3 Results

2.3.1 Improving PbS synthesis

Figure 2.1(a) shows absorbance spectra for a typical Cademartiri-synthesis (table 2.1, reaction S1). Previously published conclusions[2] are confirmed by our results: a strong nucleation event is followed by a limited QD growth, leading to monodisperse QD suspensions with a mean size ranging from 4.7 nm (after 20 s) to 5.5 nm (after 12 min, spectrum not shown). Hereafter, σ_d starts to increase strongly (figure 2.1(c), ∘). To gain more insight into the reaction kinetics, we monitored the synthesis yield (i.e. the fraction of S incorporated into the QDs). Figure 7.2 (green ∘) shows that the yield is constant throughout the synthesis, averaging 54%

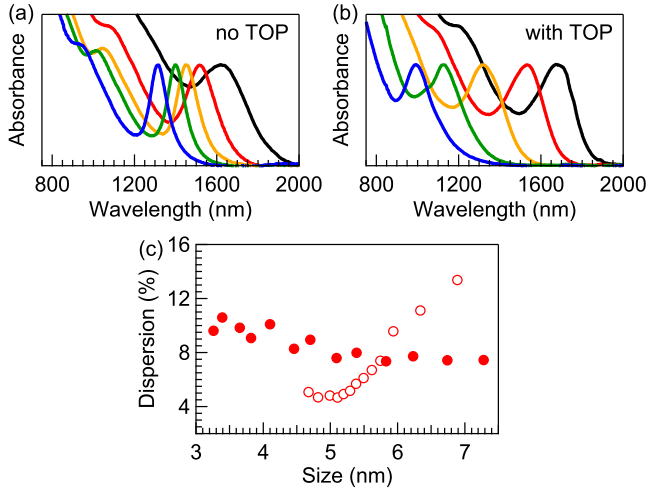

Figure 2.1: Series of absorbance spectra for PbS QDs synthesized at 120 °C, without (a) and with (b) TOP added to the synthesis. Aliquots are taken at times between 20 s (blue), 100 s (green), 450 s (yellow), 33 min (red) and 90 min (black). (c) Relative size dispersion σ_d of the aliquots for the TOP-less (○) and TOP-containing (●) synthesis.

no.	$PbCl_2$	OLA-S	TOPS
S1	0.4	0.1	0
S2	0.4	0.05	0.05
S3	0.4	0.05	0

Table 2.1: Syntheses carried out at 120 °C, using the concentrations indicated (in mol/L).

over the different aliquots taken. This remarkable result implies that even after 20 s, the QDs no longer grow by the incorporation of additional monomers (the reaction scheme most often encountered in colloidal quantum dot synthesis).-[30,31] At this stage, the synthesis must then be based on a ripening mechanism, either involving the growth of bigger particles at the expense of smaller ones (Ostwald ripening) or involving a coalescence of QDs.[32]

As a result, the Cademartiri-synthesis only offers a limited range for which monodisperse QD suspensions can be obtained, and varying the temperature (figure 2.2(a), ○) between 80 and 160 °C does not substantially increase it. To overcome this drawback, we introduce TOPS as a low-reactivity S precursor. The

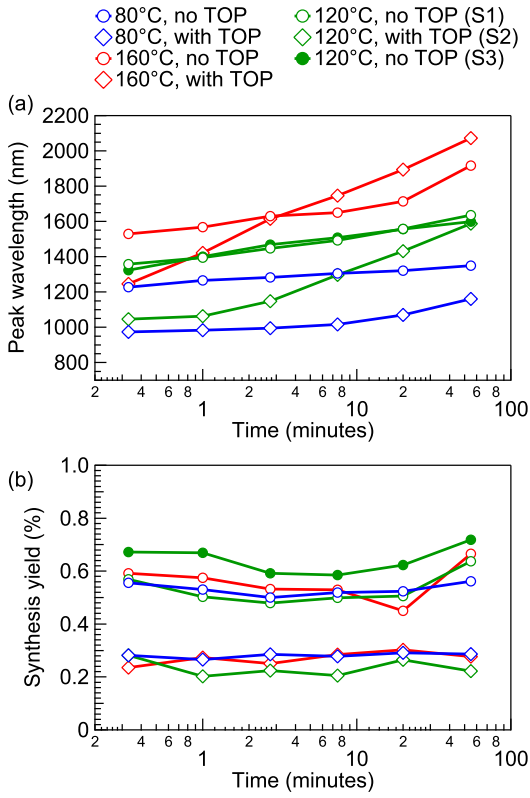

Figure 2.2: Spectral position of the QD first absorption peak as a function of time (log-scale) and temperature for syntheses with (◇) and without (○) TOP.

rationale is that a precursor with a low but non-zero reactivity could lead to prolonged QD growth after the nucleation of PbS from $PbCl_2$ and OLA-S. Hence, larger QDs should be obtainable without a strong increase in size-dispersion, similar to a secondary injection of precursors.[33] Figure 2.1(b) shows absorbance spectra of a series of aliquots for PbS QDs synthesized at 120 °C, with 170 µL of TOP added to the synthesis (figure 2.1, reaction S2, TOPS:OLA-S ratio of 1:1). As anticipated, the transformation of 50% of OLA-S to TOPS appears to extend the QD growth. For comparison: after 20 seconds we obtain 3.3 nm QDs, which grow up to 5.1 nm after 12 minutes and finally 7.3 nm after 2.5 hours. The synthesis yield drops to 23% (figure 2.2(b), ◇), again being constant as a function of time. At both higher and lower tempera-

tures, a similar result is obtained (figure 2.2(b), ◇). Although the reduced yield confirms that the addition of TOPS leads to fewer nuclei being formed (i.e. TOPS is not included during nucleation), its time-independence again hints toward a more complex reaction mechanism based on ripening. Possibly, the major role of TOPS is merely to facilitate this ripening, as the enhanced growth rate and constant yield suggests. Note that monodispersity is maintained in reaction S2 (figure 2.1(c), ●). For QDs larger than *ca.* 6 nm, this leads to an improved σ_d compared to the TOP-less synthesis (a similar behavior is observed at other temperatures). Hence, although uncommon, ripening does not necessary lead to an increase in σ_d.[2,34]

The heterogeneous synthesis described here is presently not yet fully understood. In addition, similar to the case of PbSe QDs synthesized from lead oleate and TOPSe, impurities in TOP may influence the results.[35] However, despite the need for further experimental data and theoretical modeling of this reaction, the observation that TOPS is not a mere stable, unreactive compound present during synthesis is clearly verified by a control experiment. When simply reducing the OLA-S concentration by 50%, without addition of TOPS (figure 2.1, reaction S3), we do not observe any changes in the QD growth kinetics compared to reaction S1, apart from a slight increase of the yield to 63% (figure 2.2, ●).

Using growth temperatures from 80°C to 160°C, replacement of 50% of OLA-S by TOPS consistently leads to a wider range of sizes accessible (figure 2.2(a), ◇). As a result, QDs between 3 and 10 nm can now be synthesized *via* a one-step procedure, spanning a range of band gaps going from 1.34 eV (925 nm) down to 0.59 eV (2100 nm). In figure 2.3, we display the optimal results. Full lines represent QDs synthesized using TOP; the larger sizes typically have a better σ_d when prepared with TOP, while QDs with a peak absorption below 1200 nm cannot be obtained without it. For QDs with an exciton peak between 1200 and 1600 nm, the original Cademartiri-synthesis still provides the best results (dotted lines). Note that in some cases we also observe large clusters in our suspension (figure 2.3(b)). When this occurs, we simply remove these by size-selective precipitation, adding a small amount of ethanol (EtOH) to a suspension of PbS QDs until precipitation starts. Figure 2.3(c) indeed shows that they can be efficiently removed.

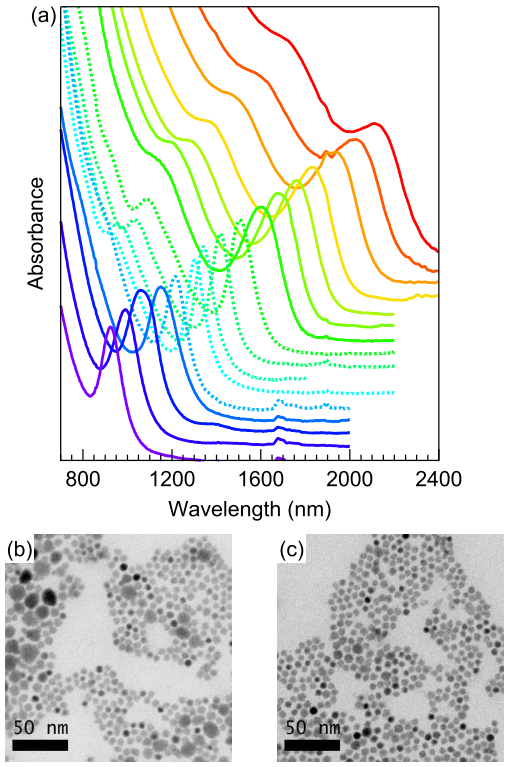

Figure 2.3: (a) Typical absorbance spectra of PbS QD suspensions. Full lines are QDs synthesized with TOP, dotted lines without TOP. (b-c) TEM images of a typical PbS QD suspension before (b) and after (c) size-selective precipitation.

2.3.2 PbS QD stability and luminescence properties

Interestingly, for the Cademartiri-synthesis, only the original work of Cademartiri et al.[2] reports on the PLQY of these QDs; they found a value of *ca.* 40%. Literature data mostly concern OA capped PbS QDs synthesized *via* the Hines-synthesis. In this case, small QDs (peak absorption of 1100–1300 nm) typically show a PLQY between 20%[1] and 60–80%.[20,21] For larger QDs (peak absorption of 1300–1600 nm), the PLQY goes down to 25-40%.[21] This is in line with the reduced PLQY observed for large PbSe QDs.[36] A more in depth study has been performed by Semonin et al.[22] where they measured the PLQY for a series of PbSe and PbS QD sizes with an integrating sphere. They confirmed the decrease of the PLQY with increasing size, and attribute it to

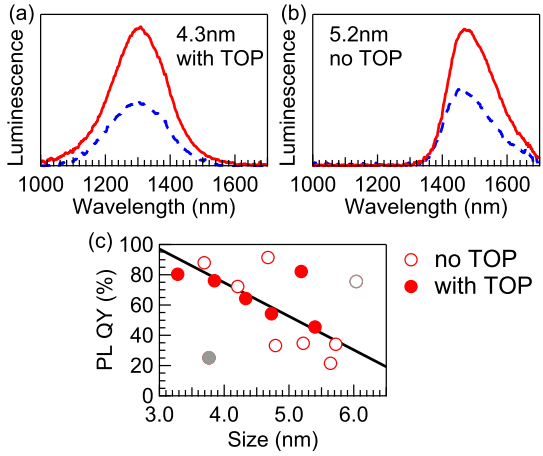

Figure 2.4: (a)-(b) Luminescence spectra of OLA (dashed curve) and OA (full curve) capped PbS QDs. After capping exchange to OA, we observe an enhancement in PLQY for both PbS QDs synthesized with (a) and without (b) TOP, respectively. (c) PLQY for several OA capped PbS QDs, synthesized either with (●) or without (○) TOP.

a quenching by localized trap states. The resulting monotonic decrease is further modulated by quenching through energy transfer to the ligands vibrational modes (Förster resonance energy transfer), which yields dips in the PLQY spectrum at wavelengths where the OA ligands show a strong absorption.
Here we demonstrate that PbS QDs prepared with the Cademartiri-synthesis also exhibit a high PLQY. First, we investigate the role of the ligands. By measuring the PL spectrum before and after OA exchange (figure 2.4(a) and (b)), we observe that the tightly bound OA ligands provide an improved electronic passivation with respect to the highly dynamic OLA, irrespective of the synthesis employed (either with our without TOP). We typically obtain a two-fold enhancement of the PL (10 samples measured, 5 synthesized with TOP and 5 without TOP). Second, the absolute PLQY is determined for a series of OA capped PbS QDs (3–6 nm, figure 2.4 (c)), synthesized both with (●) and without (○) TOP. Again, no appreciable difference is observed between both types. Fitting a line to all data except the outermost two points (grey) shows that, although individual measurements are more scattered than in the report of Semonin et al.[22] the PLQY decreases with

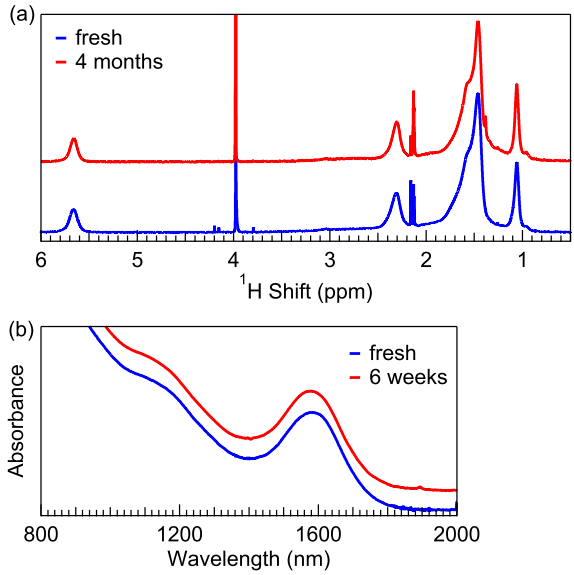

Figure 2.5: (a) ^{1}H NMR spectra of a fresh PbS QD suspension (bottom) and after 4 months (top). (b) Absorbance spectra of a fresh suspension (bottom) and after 6 weeks (top). In both cases, no changes are observed. Spectra are offset for clarity.

size in this range. However, all samples show a high PLQY, varying between 20% for the larger QDs and 90% for the smaller ones. Apart from a high luminescence yield, optical stability is also a desirable property if one wishes to apply these QDs in photonic devices. Using both NMR and absorbance spectroscopy, we demonstrate that OA capped PbS QDs are stable under ambient conditions. Figure 2.5(a) compares the ^{1}H NMR spectrum (5.6 nm QDs) of a freshly prepared PbS QD suspension with the spectrum after 4 months. The spectrum shows that, apart from a sharp singlet due to dibromomethane (CH2Br2, 3.94 ppm), a quintuplet due to residual toluene (2.09 ppm) and a singlet possibly due to methanol (2.12 ppm), no sharp signals arising from OLA-S and/or TOPS are observed. The broad resonances arise from OA ligands bound to the PbS Qdot surface. Moreover, the absence of any significant changes indicates that the ligands are unperturbed during storage. The stability of the ligand shell suggests that the surface does not oxidize. This in turn results in stable optical properties. Figure 2.5(b) shows that the absorbance

spectrum of 6.2 nm QDs is unmodified during storage for 6 weeks. We obtained similar results for smaller QDs with luminescence spectroscopy.[37] These data strongly contrast with PbSe QDs.[23–25] Here we observed both a release of OA ligands and a subsequent blue shift of the first exciton peak,[23] indicative of a fast oxidation. Interestingly, the results also differ from PbS QDs prepared *via* the Hines-synthesis, where small QDs are stable, but larger QDs exhibit a blue shift of the absorbance peak.[26] We hypothesize that the layer of Cl ions,[2,17] which constitutes the main difference between both types PbS QDs, leads to an enhanced stability of the QD surface. This has also been suggested by Cademartiri et al.[2] who observed that PbS QD thin films maintain their luminescence even after a plasma treatment.[27] These results emphasize that the synthesis method still can play an important role in the final properties of QDs with essentially the same PbS core composition.

2.4 Conclusions

By adaptation of the PbS QD synthesis described by Cademartiri et al.[2] more specifically by employing TOP during the synthesis, a strongly enlarged range of QD sizes can be synthesized. Monodisperse suspensions with an average size between 3 and 10 nm can now be prepared *via* a one-step synthesis. However, a ligand exchange is needed in order to exchange OLA by OA. The OA ligands are tightly bound to the QD surface as oleate ions, hereby strongly enhancing the luminescence yield to values of up to 90%. The PbS QDs are air-stable in suspension, offering prospects for operation of PbS QD-based photonic devices under ambient conditions.

Bibliography

[1] Hines, M.; Scholes, G. Colloidal PbS Nanocrystals with Size-Tunable Near-Infrared Emission: Observation of Post-Synthesis Self-Narrowing of the Particle Size Distribution. *Advanced Materials* **2003**, *15*, 1844–1849.

[2] Cademartiri, L.; Bertolotti, J.; Sapienza, R.; Wiersma, D. S.; von Freymann, G.; Ozin, G. a. Multigram scale, solventless, and diffusion-controlled route to highly monodisperse PbS nanocrystals. *The journal of physical chemistry. B* **2006**, *110*, 671–3.

[3] Murray, C. B.; Sun, S. H.; Gaschler, W.; Doyle, H.; Betley, T. A.; Kagan, C. R. Colloidal synthesis of nanocrystals and nanocrystal superlattices. *Ibm Journal of Research and Development* **2001**, *45*, 47–56.

[4] Murphy, J. E.; Beard, M. C.; Norman, A. G.; Ahrenkiel, S. P.; Johnson, J. C.; Yu, P.; Mićić, O. I.; Ellingson, R. J.; Nozik, A. J. PbTe colloidal nanocrystals: synthesis, characterization, and multiple exciton generation. *Journal of the American Chemical Society* **2006**, *128*, 3241–7.

[5] Urban, J. J.; Talapin, D. V.; Shevchenko, E. V.; Murray, C. B. Self-assembly of PbTe quantum dots into nanocrystal superlattices and glassy films. *Journal of the American Chemical Society* **2006**, *128*, 3248–3255.

[6] Urban, J. J.; Talapin, D. V.; Shevchenko, E. V.; Kagan, C. R.; Murray, C. B. Synergism in binary nanocrystal superlattices leads to enhanced p-type conductivity in self-assembled PbTe/Ag2 Te thin films. *Nature materials* **2007**, *6*, 115–21.

[7] Bakueva, L.; Musikhin, S.; Hines, M. a.; Chang, T.-W. F.; Tzolov, M.; Scholes, G. D.; Sargent, E. H. Size-tunable infrared (10001600 nm) electroluminescence from PbS quantum-dot nanocrystals in a semiconducting polymer. *Applied Physics Letters* **2003**, *82*, 2895.

[8] Konstantatos, G.; Huang, C.; Levina, L.; Lu, Z.; Sargent, E. H. Efficient Infrared Electroluminescent Devices Using Solution-Processed Colloidal Quantum Dots. *Advanced Functional Materials* **2005**, *15*, 1865–1869.

[9] Hoogland, S.; Sukhovatkin, V.; Howard, I.; Cauchi, S.; Levina, L.; Sargent, E. H. A solution-processed 1.53 mum quantum dot laser with temperature-invariant emission wave-

length. *Optics express* **2006**, *14*, 3273–81.

[10] Luther, J. M.; Law, M.; Beard, M. C.; Song, Q.; Reese, M. O.; Ellingson, R. J.; Nozik, A. J. Schottky solar cells based on colloidal nanocrystal films. *Nano letters* **2008**, *8*, 3488–92.

[11] Sargent, E. H. Infrared photovoltaics made by solution processing. *Nature Photonics* **2009**, *3*, 325–331.

[12] McDonald, S. a.; Konstantatos, G.; Zhang, S.; Cyr, P. W.; Klem, E. J. D.; Levina, L.; Sargent, E. H. Solution-processed PbS quantum dot infrared photodetectors and photovoltaics. *Nature materials* **2005**, *4*, 138–42.

[13] Rauch, T.; Boberl, M.; Tedde, S. F.; Furst, J.; Kovalenko, M. V.; Hesser, G. N.; Lemmer, U.; Heiss, W.; Hayden, O. Near-infrared imaging with quantum-dot-sensitized organic photodiodes. *Nature Photonics* **2009**, *3*, 332–336.

[14] Tang, J.; Wang, X.; Brzozowski, L.; Barkhouse, D. A. R.; Debnath, R.; Levina, L.; Sargent, E. H. Schottky quantum dot solar cells stable in air under solar illumination. *Advanced materials (Deerfield Beach, Fla.)* **2010**, *22*, 1398–402.

[15] Ma, W.; Luther, J. M.; Zheng, H.; Wu, Y.; Alivisatos, A. P. Photovoltaic Devices Employing Ternary PbS x Se 1-x Nanocrystals 2009. *Nano letters* **2009**, 5–9.

[16] Moreels, I.; Lambert, K.; De Muynck, D.; Vanhaecke, F.; Poelman, D.; Martins, J. C.; Allan, G.; Hens, Z. Composition and Size-Dependent Extinction Coefficient of Colloidal PbSe Quantum Dots. *Chemistry of Materials* **2007**, *19*, 6101–6106.

[17] Moreels, I.; Lambert, K.; Smeets, D.; De Muynck, D.; Nollet, T.; Martins, J. C.; Vanhaecke, F.; Vantomme, A.; Delerue, C.; Allan, G.; Hens, Z. Size-dependent optical properties of colloidal PbS quantum dots. *ACS nano* **2009**, *3*, 3023–30.

[18] Du, H.; Chen, C.; Krishnan, R.; Krauss, T. D.; Harbold, J. M.; Wise, F. W.; Thomas, M. G.; Silcox, J. Optical Properties of Colloidal PbSe Nanocrystals. *Nano* **2002**, 3–6.

[19] Wehrenberg, B. L.; Wang, C.; Guyot-Sionnest, P. Interband and Intraband Optical Studies of PbSe Colloidal Quantum Dots. *The Journal of Physical Chemistry B* **2002**, *106*, 10634–10640.

[20] Lin, W.; Fritz, K.; Guerin, G.; Bardajee, G. R.; Hinds, S.; Sukhovatkin, V.; Sargent, E. H.; Scholes, G. D.; Winnik, M. a.

Highly luminescent lead sulfide nanocrystals in organic solvents and water through ligand exchange with poly(acrylic acid). *Langmuir : the ACS journal of surfaces and colloids* **2008**, *24*, 8215–9.

[21] Abel, K. A.; Shan, J.; Boyer, J.-c.; Harris, F.; Veggel, F. C. J. M. V. Beneficial Effect of Trioctylphosphine. *Communications* **2008**, 3794–3796.

[22] Semonin, O. E.; Johnson, J. C.; Luther, J. M.; Midgett, A. G.; Nozik, A. J.; Beard, M. C. Absolute Photoluminesnence Quantum Yields of IR-26 Dye, PbS, and PbSe Qunatum Dots. *Journal of Physical Chemistry Letters* **2010**, *1*, 2445–2450.

[23] Moreels, I.; Fritzinger, B.; Martins, J. C.; Hens, Z. Surface chemistry of colloidal PbSe nanocrystals. *Journal of the American Chemical Society* **2008**, *130*, 15081–6.

[24] Dai, Q.; Wang, Y.; Zhang, Y.; Li, X.; Li, R.; Zou, B.; Seo, J.; Wang, Y.; Liu, M.; Yu, W. W. Stability study of PbSe semiconductor nanocrystals over concentration, size, atmosphere, and light exposure. *Langmuir : the ACS journal of surfaces and colloids* **2009**, *25*, 12320–4.

[25] Sykora, M.; Koposov, A. Y.; Mcguire, J. A.; Schulze, R. K.; Tretiak, O.; Pietryga, J. M.; Klimov, V. I. Effect of Air Exposure on Surface Properties , Electronic Structure , and. *ACS nano* **2010**, *4*, 2021–2034.

[26] Tang, J.; Brzozowski, L.; Barkhouse, D. A. R.; Wang, X. H.; Debnath, R.; Wolowiec, R.; Palmiano, E.; Levina, L.; Pattantyus-Abraham, A. G.; Jamakosmanovic, D.; Sargent, E. H. Quantum Dot Photovoltaics in the Extreme Quantum Confinement Regime: The Surface-Chemical Origins of Exceptional Air- and Light-Stability. *Acs Nano* **2010**, *4*, 869–878.

[27] Cademartiri, L.; von Freymann, G.; Arsenault, A. C.; Bertolotti, J.; Wiersma, D. S.; Kitaev, V.; Ozin, G. a. Nanocrystals as precursors for flexible functional films. *Small (Weinheim an der Bergstrasse, Germany)* **2005**, *1*, 1184–7.

[28] de Mello, J.; Wittmann, H.; Friend, R. An Improved Experimental Determination of External Photoluminiscence Quantum Efficiency. *Advanced Materials* **1997**, *9*, 230–232.

[29] Porrès, L.; Holland, A.; På lsson, L.-O.; Monkman, A. P.; Kemp, C.; Beeby, A. Absolute measurements of photolumi-

nescence quantum yields of solutions using an integrating sphere. *Journal of fluorescence* **2006**, *16*, 267–72.

[30] Bullen, C. R.; Mulvaney, P. Nucleation and Growth Kinetics of CdSe Nanocrystals in Octadecene. *Nano Letters* **2004**, *4*, 2303–2307.

[31] Rempel, J. Y.; Bawendi, M. G.; Jensen, K. F. Insights into the kinetics of semiconductor nanocrystal nucleation and growth. *Journal of the American Chemical Society* **2009**, *131*, 4479–89.

[32] Zheng, H.; Smith, R. K.; Jun, Y.-W.; Kisielowski, C.; Dahmen, U.; Alivisatos, a. P. Observation of single colloidal platinum nanocrystal growth trajectories. *Science (New York, N.Y.)* **2009**, *324*, 1309–12.

[33] Peng, X.; Wickham, J.; Alivisatos, a. P. Kinetics of II-VI and III-V Colloidal Semiconductor Nanocrystal Growth: Focusing of Size Distributions. *Journal of the American Chemical Society* **1998**, *120*, 5343–5344.

[34] Talapin, D. V.; Rogach, A. L.; Haase, M.; Weller, H. Evolution of an Ensemble of Nanoparticles in a Colloidal Solution: Theoretical Study. *The Journal of Physical Chemistry B* **2001**, *105*, 12278–12285.

[35] Evans, C. M.; Evans, M. E.; Krauss, T. D. Mysteries of TOPSe revealed: insights into quantum dot nucleation. *Journal of the American Chemical Society* **2010**, *132*, 10973–5.

[36] Pietryga, J. M.; Schaller, R. D.; Werder, D.; Stewart, M. H.; Klimov, V. I.; Hollingsworth, J. a. Pushing the band gap envelope: mid-infrared emitting colloidal PbSe quantum dots. *Journal of the American Chemical Society* **2004**, *126*, 11752–3.

[37] Justo, Y.; Moreels, I.; Lambert, K.; Hens, Z. Langmuir Blodgett monolayers of colloidal lead chalcogenide quantum dots : morphology and photoluminescence. *Nanotechnology* **2010**, *21*, 295606.

Chapter III

Core/shell PbX/CdX quantum dots by cationic exchange.

3.1 Introduction

Nanoparticles can be categorized into cores, formed by a single material and core/shell structures, composed of two or more materials. Core/shells can consist of a wide range of different combinations, including inorganic/inorganic, inorganic/organic, organic/inorganic and organic/organic materials.[1] In recent years, the synthesis of core/shell nanocrystals has achieved a remarkable control over the size and the shape, yielding a variety of forms like the ones shown in Figure 3.1.

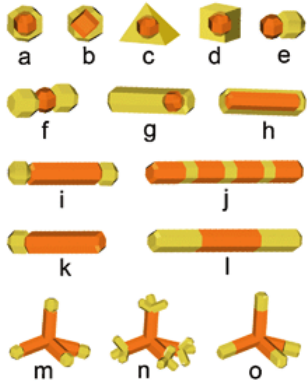

Figure 3.1: Scheme of different core/shell QDs shapes

In the case of semiconductors nanocrystals, core/shell configurations (figure 3.1a-d, g) attract more and more attention since they are highly functional materials with modified properties.[2–6] Overcoating of core quantum dots (QDs) by a shell leads to an overall increase of the stability and allows for a further tuning of the opto-electronic properties.[7] Research on applications of different core/shell nanoparticles has been summarized in a review article by Kalele et al.[8] and includes biomedical,[9] pharmaceutical applications,[10] catalysis,[11] electronics,[12] enhanced luminescence,[13] etc.

Regarding the synthesis, depending on the type of semiconductor, shell growth can be achieved by several methods. In the case of II-VI semiconductors, there are multiple studies about synthesis of CdSe/ZnS,[14] CdSe/CdS, CdSe/CdS/ZnS core/shell nanocrystals among which, the successive ionic layer adsorption and reaction procedure (SILAR), has been receiving the spotlight.[15] This layer-by-layer procedure involves the consecutive growth of anionic and cationic monolayers on the particles, until the desired shell thickness is reached, maintaining an excellent size dispersion.

IV-VI semiconductors, on which this thesis is focused, are characterized by the rocksalt structure and mainly lead-based QDs have been studied in the form of core/shell systems. These compounds have small bandgaps and therefore, they are good candidates for the design of near-infrared emitters. Lifshitz and coworkers reported the synthesis of PbSe/PbS and PbSe/$PbSe_xS_{1-x}$ core/shell QDs emitting in the range of 1-2 μm with QYs of 40-50% and 65%, respectively.[16–18] The SILAR method, previously mentioned in the case of CdSe/CdS, has been applied for the synthesis of PbSe/PbS QDs.[19] Talapin et al.[20] recently synthesized PbSe/PbS core/shell spheres and nanowires, tailoring the morphology of the core QDs by addition of co-surfactants (e.g., alkylamines, alkylphosphonic acids). Hollingsworth and co-workers developed PbSe/CdSe core/shell QDs by the exchange of surface lead ions by cadmium.[3] A strongly improved stability of the optical properties was observed, which can further be enhanced by the subsequent overgrowth of the core/shell system with an additional ZnS shell.

In this chapter we focus on cationic exchange reaction, studying the parameters to control the process and giving possible explanations to understand the mechanism of the exchange.

3.2 Cation exchange in literature

3.2.1 Basic concepts of cationic exchange

Several research groups have demonstrated that the composition of nanocrystals can be altered after synthesis by exchanging either the cation or the anion by means of an exchange reaction.[21–26] The first and most studied system is CdSe-Ag_2Se, where the following cationic exchange reaction is typically used:[21]

$$\mathrm{CdSe}_{toluene} + 2\mathrm{Ag}^{+}(\mathrm{MeOH}) + 2\mathrm{NO}_3^{-}(\mathrm{MeOH}) \rightarrow$$

$$\mathrm{Ag_2Se}_{toluene} + \mathrm{Cd}^{2+}(\mathrm{MeOH}) + 2\mathrm{NO}_3^{-}(\mathrm{MeOH})$$

$$\mathrm{Ag_2Se}_{toluene} + \mathrm{Cd}^{2+}(\mathrm{MeOH}) + 2\mathrm{NO}_3^{-}(\mathrm{MeOH}) + 2\mathrm{TBP}_{toluene} \rightarrow$$

$$\mathrm{CdSe}_{toluene} + 2\mathrm{Ag}^{+}(\mathrm{TBP}) + 2\mathrm{NO}_3^{-}(\mathrm{MeOH})$$

Subscripts indicate suspensions, whereas the parentheses denote solvation. In this case, Ag^+ for Cd^{2+} exchange takes place at room temperature and is surprisingly fast (<1 s). Such fast kinetics are considered to be mainly due to a low activation barrier and a favorable thermodynamic driving force. These exchange reactions can be qualitatively understood in terms of hard-soft acid-base theory, where the monovalent Ag^+ cation is softer than the divalent Cd^{2+} cation.[27] Thus, MeOH, a hard base, preferentially binds Cd^{2+} cations, while the soft base, TBP, binds strongly to Ag^+ cations. It can bind to both Ag^+ ions in the shell and Cd^{2+} ions in solution, forming intermediate complexes. The stronger interaction between TBP and Ag^+ however leads to the replacement of Ag^+ by Cd^{2+} in the Ag_2Se nanocrystal. Methanol is also required for cationic exchange reactions. It may be involved in the formation of intermediate complexes.
The effectiveness of the CdSe → Ag_2Se exchange can also be explained based on the crystal structures of Ag_2Se and CdSe. The anion sublattice in Ag_2Se (orthorhombic) and CdSe (wurtzite) have a topotactic relationship, meaning that the a and b axes of Ag_2Se are almost the same as the a and c axes of CdSe. As a result, the anions stay on the same positions facilitating the in-and-out diffusion of cations though the lattice. The topotactic relationship is not essential to achieve the cationic exchange but

it might explain why in non-topotactic cases, higher temperatures are required.

3.2.2 Cation exchange with lead chalcogenides

A partial cationic exchange was applied by Pietryga et al.[28] to exchange Pb^{2+} by Cd^{2+} in PbSe QDs and create PbSe/CdSe core/shell QDs. The bulk lattice parameters of cubic PbSe (rock-salt) and CdSe (zinc-blende) differ by ≈1 %, increasing the probability of a smooth, low-defect interface between both materials. Rather than using conditions to promote the exchange, such as selective solvation conditions or an appropriate binding agent, which can easily lead to a total replacement of cations, these authors use milder reaction conditions to achieve a core/shell structure.
They made use of a less reactive cadmium precursor (cadmium oleate (CdOA)) and a non coordinating solvent (toluene) so that the reaction takes place under more controlled conditions. The reaction is carried out at 100℃ using a large excess of cadmium. The exchange is applicable to a wide range of sizes (from 5 to 11 nm) but the reaction does not proceed beyond a certain shell thickness (around 1.5 nm) even using larger excess of cadmium and longer reaction times.
The same reaction was applied by Lambert et al.[29] on PbTe QDs to form PbTe/CdTe QDs. They observed the structures of the core and the shell by high-resolution transmission electron microscopy (HR-TEM). They discovered that the mechanism of exchange is anisotropic, leading to a strong increase of the heterogeneity of the nanocrystals, in terms of the geometry (core size and shape, position of the core in the core/shell particle), but also in terms of crystallography of the core/shell structure. To exemplify this, figure 3.2 shows two core/shell structures made in the same reaction. One clearly sees that specific crystal facets separate core and shell and that both size and position of the core can differ strongly from nanocrystal to nanocrystal.
The same principle as for the system CdSe-Ag_2Se, was applied by Luther et al.[22] to other systems like CdS → Cu_2S → PbS. Analogous to the example described above, the exchange of CdS with Cu^+ is promoted with methanol. After purification of the product, the exchange of Pb^{2+} with Cu_2S nanocrystals (QDs) is promoted by adding some TBP to reaction mixture. The ex-

change follows the reaction in the scheme below:

$$CdS_{toluene} + 2Cu^{+}(MeOH) + 2PF_6^{-}(MeOH) \rightarrow$$

$$Cu_2S_{toluene} + Cd^{2+}(MeOH) + PF_6^{-}(MeOH)$$

$$Cu_2S_{toluene} + Pb^{2+}(MeOH) + 2OAc(MeOH) + 2TBP_{toluene} \rightarrow$$

$$PbS_{toluene} + 2Cu^{+}(TBP) + 2OAc^{-}(MeOH)$$

Here, PF_6^{-} is the hexafluorophosphate anion of the copper salt, OA^{-} is the acetate anion of the lead salt. Subscripts indicate suspensions, whereas the parentheses denote solvation. This system will be explained in more detail in chapter VIII.

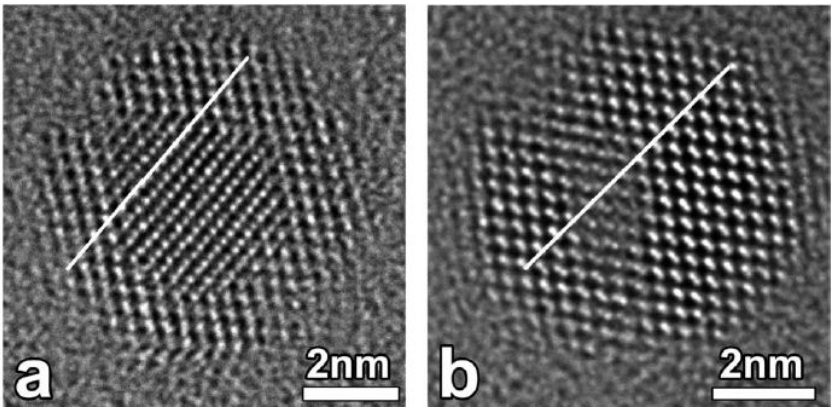

Figure 3.2: HR-TEM images of PbTe/CdTe core/shell particles in the ⟨110⟩ direction. In some particles, the lattice at one end of the core is shifted with respect to the lattice at the other end.

3.3 Shell thickness tuning

The extent of the cationic exchange reaction can be influenced by different parameters, such as the reaction time, the excess of Cd, the QD size and the reaction temperature. Here, we investigated for both PbS and PbSe QDs the effect of each parameter on the thickness of the resulting CdS and CdSe shell.

3.3.1 Shell thickness determination

The shell thickness itself is calculated from the absorption spectrum, where the wavelength of the first exciton peak is used to calculate the core diameter using the sizing curves of PbS and PbSe, respectively.[30,31] The accuracy of this method will be explained in chapters IV and V. The total size of the particle does not change due to the exchange. Therefore, we obtain the diameter of the QDs (d_{tot}) from the absorption spectrum of the initial sample. Likewise, we obtain the diameter of the PbS cores (d_{core}) from the absorption spectrum of the different core/shells. The shell thickness (δ) is calculated by means of equation 3.1.

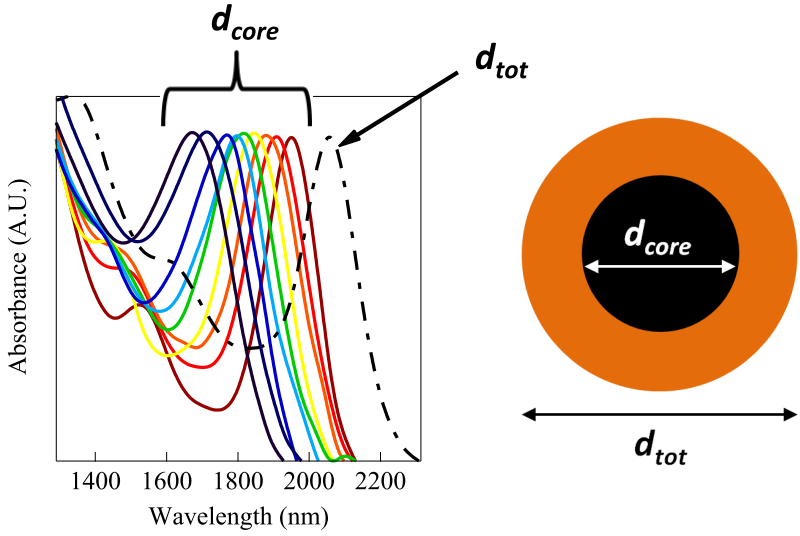

Figure 3.3: Core/shell time series. The absorption peak shifts towards shorter wavelengths as the shell thickness increases.

$$\delta = \frac{d_{tot} - d_{core}}{2} \tag{3.1}$$

3.3.2 Influence of the reaction time

Reaction time is a parameter related to the kinetics of the shell formation. However, an exhaustive study about the influence of the time on the shell growth is still required. Herein, we studied

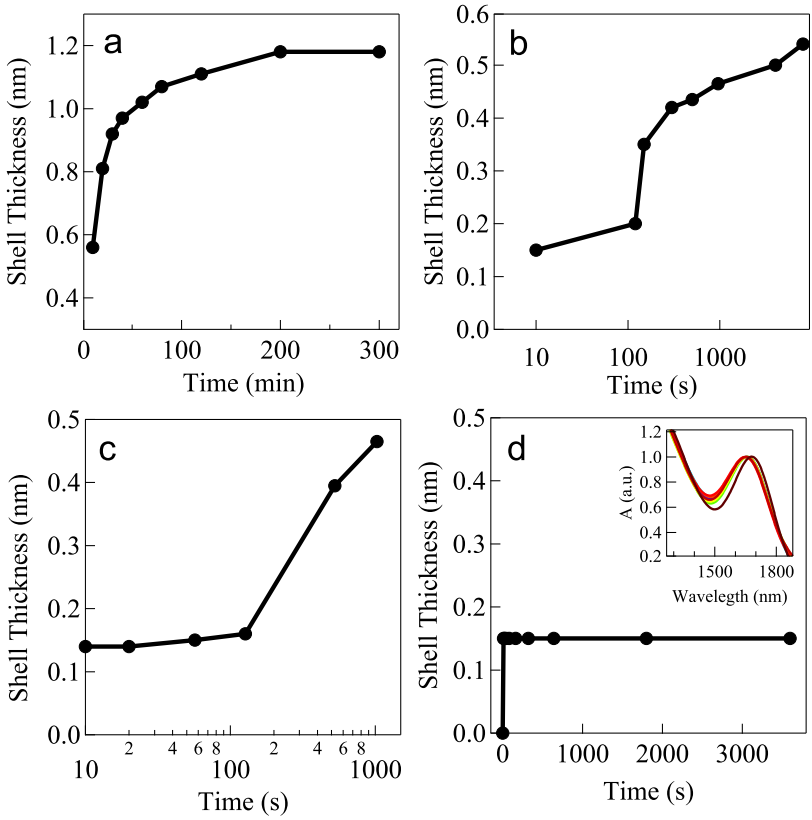

Figure 3.4: a) Evolution of the shell thickness as a function of time for 4.5 nm PbSe QDs exchanged at 100°C and 10:1 Cd:Pb from 10 min to 5 h reaction. b) Evolution of the shell thickness as a function of time for 7 nm PbS QDs exchanged at 100°C and 10:1 Cd:Pb from 10 s to 2 h reaction. Reaction time plotted on a logarithmic scale for facilitating the outlook at short reaction times. c) Evolution of the shell thickness for 7 nm PbS QDs exchanged at 100°C and 10:1 Cd:Pb at shorter reaction times, from 10 s to 15 min. Reaction time plotted on a logarithmic scale for facilitating the outlook at short reaction times. d) Evolution of the shell thickness for 7 nm PbS QDs exchanged at 40°C and 10:1 Cd:Pb.

the evolution of the shell as a function of time. To do so, we carried out exchange reactions at 100℃ and ratio 10:1 Cd:Pb, taking aliquots at different reaction times.
In the case of PbSe QDs, figure 3.4a shows the gradual change in shell thickness for 4.5 nm QDs. During the first 10 min the shell augments by roughly 0.5 nm, and it further grows to reach about 1 nm after 40 min and 1.2 nm after 200 min. For longer times, no appreciable increase in shell thickness is found, i.e., it seems that the exchange reaction comes to an end after a certain reaction time.
In the case of PbS QDs, we proceeded in the same way, yet we also took aliquots at shorter reaction times (10 s to 2 h). The result is displayed in figure 3.4b, which shows a plateau between 10 s and 2 min of reaction, followed by a stronger increase of the shell thickness and ending by a slower growth after 5 min reaction. Eventually, the exchange leads to considerable thinner shells (around 0.5 nm).
In order to fully understand the initial plateau, find out what happens at shorter reaction times and determine when the reaction starts, we repeated the exchange while taking extra aliquots at short reaction times (from 10 s to 15 min). Figure 3.4c shows that after 10 s the reaction leads to a shell thickness of 0.15 nm, which stays constant for around 2 min. Hereafter, the strong increase of the shell begins. We found this result intriguing and in order to understand it better, we repeated the reaction decreasing the temperature to 40℃. Figure 3.4d shows that even at such a low temperature, we obtain a shell thickness of about 0.15 nm. However, the exchange does not progress beyond this point. Moreels et al.[30] proved that PbSe QDs are composed of a quasi-stoichiometric PbSe core terminated by a Pb surface shell. Hence, the 0.15 nm shell could correspond to the Pb surface shell that has been exchanged. This result indicates that the exchange of the atoms in the surface is almost spontaneous. However, to proceed beyond this point, the reaction needs extra energy, obtained from the increase in temperature.

3.3.3 Influence of the cadmium excess

The excess of Cd is one of the parameters that has to be taken into account to carry out cationic exchange reactions. Pietryga et al.[28] suggested that a certain excess of Cd was essential to promote the

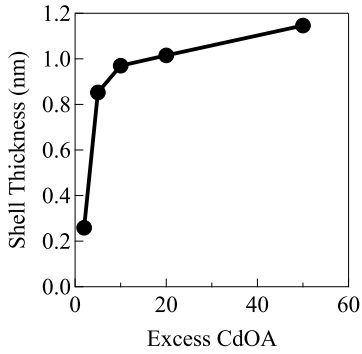

Figure 3.5: Shell thickness obtained on PbSe QDs using different ratios Cd:Pb.

exchange but without clarifying the effect of varying this parameter upon the reaction. To elucidate this, we carried out cationic exchange reactions on 6 nm PbSe QDs at 100°C for 40 min using different excess of Cd. Figure 3.5 shows the effect of increasing the ratio Cd:Pb over the shell thickness. The shell thickness increases dramatically when the excess of Cd is augmented form 2:1 to 5:1 Cd:Pb, however increasing the excess more than 5 times only leads to a slight increment on the thickness. This result indicates that a certain excess is needed to achieve the exchange at relatively fast speed but beyond that threshold, an increase on the amount of Cd does not lead to a remarkable effect on the kinetics of the reaction.

3.3.4 Influence of the nanocrystal size

Nanocrystal size could be a factor to take into account when carrying out a cationic exchange reaction. A difference in size means a difference in surface to volume ratio, therefore the kinetics of the reaction might be altered by changing this factor. To study this effect, we carried out cationic exchange reactions at 100°C and a 10-fold excess of Cd. We used four different sizes of PbSe QDs, from 4.5 nm to 8 nm. Figure 3.6a shows that the smaller the QD, the faster the shell grows. This can be attributed to the fact that smaller QDs have smaller surface, so the Cd atoms can diffuse faster to exchange the next atomic layer. However, regardless of the initial diameter, the reaction does not proceed beyond 1-1.2 nm. This result suggests that the saturation of the shell thickness is independent of the QD size.

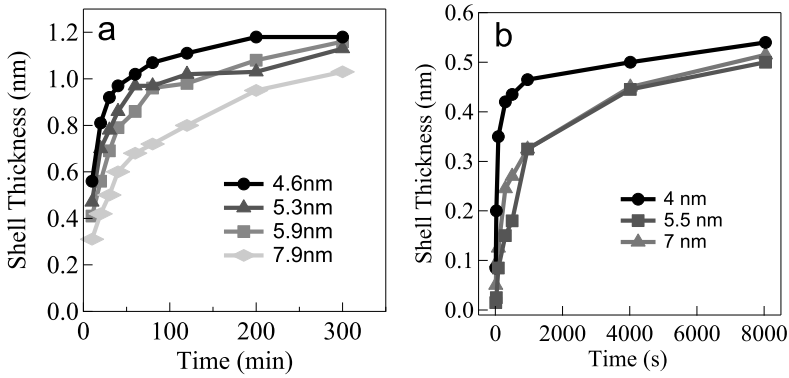

Figure 3.6: a) Shell thickness as a function of time for four different sizes of PbSe QDs, from 4.5 to 8 nm exchanged at 100℃ and 10:1 Cd:Pb. b) Shell thickness as a function of time for three different sizes of PbS QDs, from 4 to 7 nm exchanged at 100℃ and 10:1 Cd:Pb.

In the case of PbS QDs, the size dependent behavior is not so pronounced. The same reaction kinetics is observed for 7 nm and 5.5 nm QDs. Only 4 nm PbS QDs show faster kinetics but likewise, all the sizes end up with the same shell thickness, in this case 0.5 nm. (figure 3.6b).

3.3.5 Influence of the reaction temperature

Temperature is an essential factor to carry out a cationic exchange reaction. In section 3.3.1 we showed that exchange reactions at 40℃ do not proceed beyond 0.15 nm. Whereas at 100℃ the exchange leads to shell thickness between 0.5 and 1.2 nm depending on the material. Therefore, in this section we wanted to study further the influence of this parameter.
To do so, we exchanged 7.3 nm PbSe QDs using temperatures between 100℃ and 155℃ and following the effect on the shell thickness. Figure 3.7a shows how the shell gets considerably thicker by gradually increasing the temperature. The shell augments from 1 nm at 100℃ to beyond 2 nm at 155℃. Further increase of the temperature results in fully exchanged CdSe QDs.
In the case of PbS QDs, exchanges carried out at 130℃ lead to a shell thickness close to 1 nm for 4 and 5.5 nm QDs. Whereas for 7 nm, the shell obtained is only 0.6 nm thick. In the latter, we

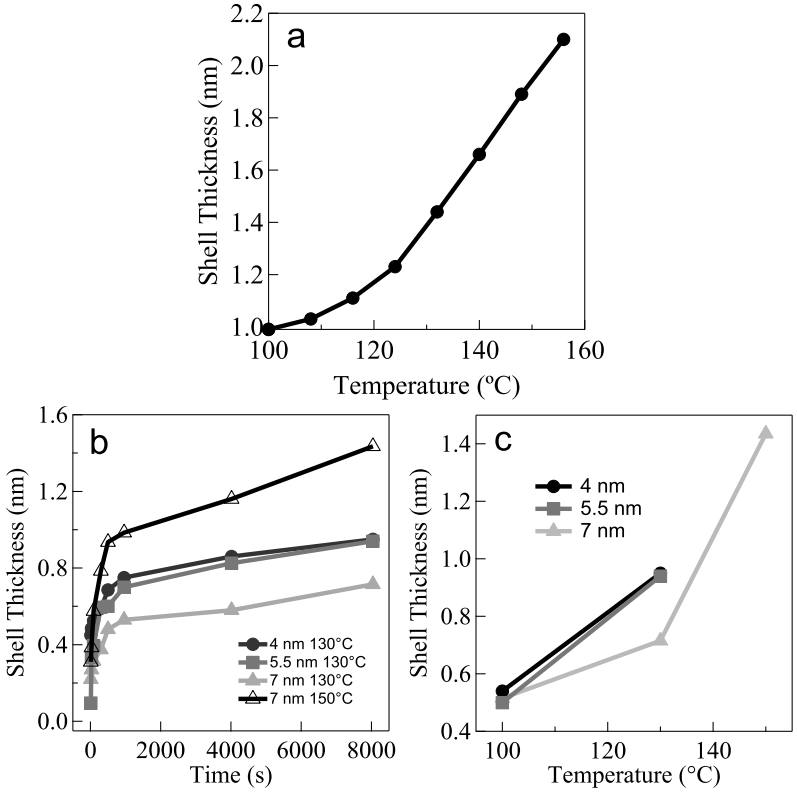

Figure 3.7: a) Increase of the shell thickness as a function of the temperature for 7 nm PbSe QDs exchanged using 10:1 Cd:Pb. b) Increase of the shell thickness as a function of time for three different sizes of PbS QDs, ratio 10:1 Cd:Pb and different temperatures. c) Increase of the shell thickness as a function of temperature for three different sizes of PbS QDs exchanged using 10:1 Cd:Pb.

had to rise the temperature to 150℃ to induce a more dramatic increase on the thickness. The results obtained for both type of QDs, indicates that the temperature is the limiting factor of the reaction. Basically, only temperature can be used to increase the thickness of the shell beyond a threshold which varies depending on the type of PbX QD.

3.3.6 Summary

Summarizing the results explained in the previous section, both materials, PbSe and PbS QDs behave similarly in view of the cationic exchange reaction. Nevertheless, under same reaction conditions, PbSe QDs obtain thicker shells as compared to PbS QDs. A certain excess of Cd atoms is essential to perform the exchange, although beyond 10 times more Cd than Pb, augmenting the excess only leads to slightly thicker shells. Different QDs sizes exhibit different reaction kinetics and smaller sizes get thicker shells at short reaction times but when the reaction saturates, all sizes end up with similar shell thickness. Increasing the temperature appears as essential to increase this limiting shell thickness.

3.4 Exploring the mechanism of the cationic exchange reaction

Understanding the mechanism that controls the cationic exchange reaction is not straightforward. In literature, there are only few attempts to give a plausible explanation for the cation exchange reaction. In this section we analyze several mechanisms, comparing them with our experimental data in order to find the mechanism that fits better to our empirical results.

3.4.1 Equilibrium model

As it was already explained in this chapter, the addition of an excess of Cd^{2+} to a heated solution of PbX QDs leads to the exchange of the outermost Pb atoms by Cd^{2+}.[3] The exchange of ions proceeds until the shell thickness reaches a limiting value. A first possibility that explains this limiting shell thickness is that it results from a balance between the forward exchange of Pb^{2+} to Cd^{2+} and the backward exchange of Cd^{2+} to Pb^{2+}:

$$\mathrm{Cd}(l) + \mathrm{Pb}(s) \rightleftharpoons \mathrm{Cd}(s) + \mathrm{Pb}(l) \tag{3.2}$$

For this equilibrium reaction we can derive the equilibrium constant K, using the following mass balance table:

n	n_{Pb}	n_{Cd}	n_{PbX}	n_{CdX}
0	0	$n_{Cd,i}$	$n_{PbX,i}$	0
α	α	$n_{Cd,i} - \alpha$	$n_{PbX,i} - \alpha$	α

Here, $n_{Cd,i}$ denotes the initial amount of cadmium (in moles) injected into the reaction mixture, α is the number of moles that have been exchanged. As the activity of a solid phase is one, and we work under conditions of a large Cd excess (*i.e.* $n_{Cd,i} \gg \alpha$).

so:

$$K = \frac{n_{Pb}}{n_{Cd}} = \frac{\alpha}{n_{Cd,i} - \alpha} \simeq \frac{\alpha}{n_{Cd,i}} \tag{3.3}$$

From where we can then derive:

$$\begin{aligned} \alpha &= K n_{Cd,i} \\ \Rightarrow n_{CdX} &= K n_{Cd,i} \\ \Rightarrow \frac{n_{CdX}}{n_{PbX,i}} &= K \frac{n_{Cd,i}}{n_{PbX,i}} \\ \Rightarrow x_{CdS} &= K e_{Cd/Pb} \end{aligned} \tag{3.4}$$

Here we have defined the relative fraction of Cd in the QD x_{CdS} and the Cd excess added to the reaction mixture $e_{Cd/Pb}$. Since we can extract the fraction of Cd in the QDs by means of the PbS or PbSe sizing curve (see chapters IV and V), we can derive the equilibrium constant K for different reaction temperatures.

Figure 3.8a depicts the values of $\ln(K)$ of the samples prepared at the same temperature but using different excess of Cd from figure 3.5. The obtained values of $\ln(K)$ are different for each excess. This result is not in line with the experiments, which showed in section 3.3 that the exchange was independent of the excess of Cd.

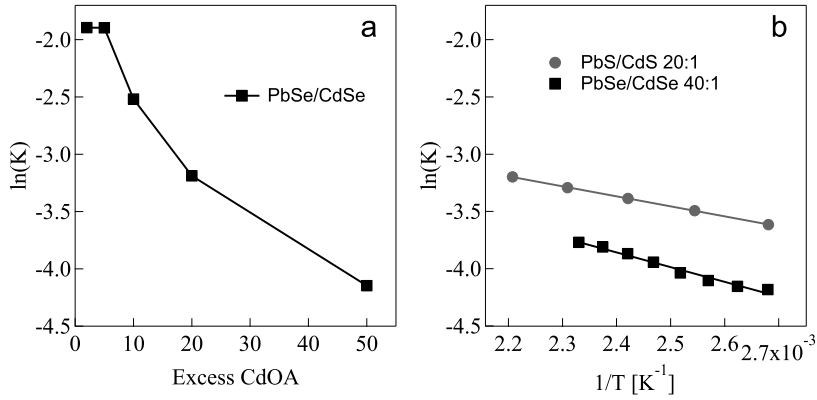

Figure 3.8: a) $ln(K)$ of the PbSe/CdSe samples from figure 3.5 as a function of the excess of Cd. b) $ln(K)$ *vs.* $1/T$ derived from the amount of exchanged Cd on PbS/CdS QDs (full circles) and PbSe/CdSe QDs (full squares) at different reaction temperatures.

On the other hand, figure 3.8b shows that $\ln(K)$ thus obtained scales with $1/T$, for both PbS/CdS and PbSe/CdSe, as expected if the standard reaction enthalpy and entropy are temperature independent. As could be expected from the large excess of cadmium needed in the exchange, we infer from these values that cationic exchange from PbX to CdX is thermodynamically unfavorable. As such the reverse reaction, where we add excess of Pb to a CdX suspension should be thermodynamically favorable. This is however not what we observe experimentally. Even at elevated temperatures, this reaction does not take place. Moreover, the shell thickness of PbX/CdX does not decrease again when decreasing the temperature of the reaction mixture. Therefore, we can conclude that this model is not plausible to explain the cation exchange reaction.

3.4.2 Diffusion model

Several research groups have based their assumptions about cationic exchange on diffusion, such as Casavola et al.[26] They attributed the exchange of PbSe/CdSe QDs to a vacancy-assisted migration in the cation sublattice. They presumed that vacancies are formed at the surface and they diffuse through the CdSe shell to the PbSe/CdSe interface. Subsequently, Pb atoms can jump

into the vacancies and be exchanged at the at surface by Cd atoms.
Likewise, Ethayaraja *et al.*[32] proposed another model where diffusion is also the limiting factor of the exchange. The reaction that they modeled is the following:

$$CdS + Pb^{2+} \rightarrow PbS + Cd^{2+}$$

They claimed that the cationic exchange consisted of three processes, 1) diffusion of Pb^{2+} from the solvent to the CdS QD, 2) diffusion of Pb^{2+} through the growing PbS shell layer and 3) exchange reaction at the core/shell (CdS-PbS) interface. They neglected the interparticle interactions since they based the model on diffusion and reaction in a single QD. Taking into account all these processes, the equation that they used to calculate to molar rate of transport is the following:

$$J = \frac{C_B}{\frac{1}{4\pi D_1 R_0} + \frac{R_0 - R}{4\pi D_2 R_0 R} + \frac{1}{4\pi R^2 k_r}} \tag{3.5}$$

In the equation above, C_B is the concentration of precursor, D_1 is the diffusivity of Pb^{2+} in the solvent, R_0 is the diameter of the particle, R is the core radius, D_2 is the solid state diffusivity of Pb^{2+} in the PbS shell and k_r is the exchange reaction rate constant.
The three terms in the denominator of the equation 3.5 are the three resistances to the transport of Pb^{2+}; diffusion in the solvent, diffusion in the PbS shell and the exchange reaction, respectively. The first term can be neglected in comparison to the second one because the diffusivity of Pb^{2+} in water is much higher as compared to that in the crystal lattice. Moreover, they point out that the activation energy barrier for diffusion in a solid (ca. 100 kJ mol^{-1}) is much higher as compared to that of the exchange reaction (which they estimate at ca. 10 kJ mol^{-1}). Therefore, they also neglect the third term of the equation. In conclusion, the solid-state diffusion step (second term of the equation), is the slowest and the rate controlling step, simplifying equation 3.5 into:

$$J' = 4\pi D_2 \frac{R R_0}{R_0 - R} C_B \tag{3.6}$$

On the other hand, the molar rate of conversion of CdS to PbS is the following:

$$J" = -4\pi R^2 \rho_A \frac{dR}{dt} \tag{3.7}$$

Here, ρ_A is the molar density of CdS. Both equations 3.6 and 3.7 can be equated and simplified for large excess of precursor, leading to an expression that represents the reaction time as a function of the core radius.

$$t = \theta_{lim} \left[1 - 3 \left(\frac{R}{R_0} \right)^2 + 2 \left(\frac{R}{R_0} \right)^3 \right] \tag{3.8}$$

where

$$\theta_{lim} = \frac{\rho_A R_0^2}{6 D_2 C_{B0}} \tag{3.9}$$

The parameter θ_{lim} is the time constant for the complete conversion of CdS QDs into PbS QDs.
In order to see whether a diffusion-limited growth model agrees with our experimental data, we fitted the data on shell thickness as a function of time to the predictions of this model for a fixed value of the diffusivity (D) and reaction rate constant k. Figure 3.9 depicts the evolution of the shell thickness as a function of time for two different sizes of PbSe QDs and their corresponding fit. The initial value for the shell thickness is chosen to be 0.15 nm. This refers to the experiment carried out at 40°C from section 3.3, which indicated a fast ($\sim$ 10s) exchange of the Pb surface shell.
As can be observed in the graph, the fits are in line with the experimental data for short reaction times ($\leq$ 40 min). However, the simulated curves do not level off for longer reaction times as the experimental values do. This suggests that the beginning of the reaction is indeed governed by a diffusion based mechanism. However, a simple diffusion limited model cannot account for the saturation of the shell thickness with increasing reaction time. Hence, additional factors should be introduced in the model to understand this.

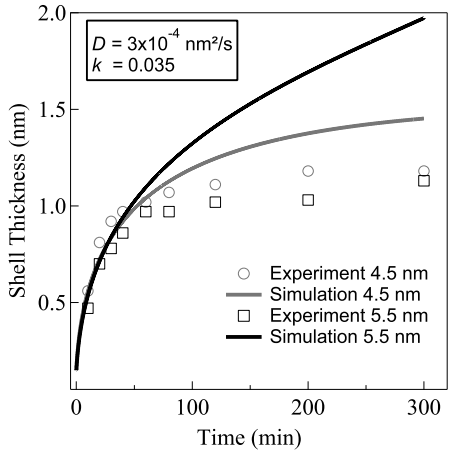

Figure 3.9: Shell thickness as a function of time for two different PbSe QDs sizes, 4.6 and 5.3 nm. Solid lines are fits based on a diffusion model, open squares and open circles are experimental values.

3.5 Discussion

We have so far reviewed some models in an attempt to understand the extent of the cationic exchange process. We started by considering a model based on thermodynamic equilibrium, but it was rejected since it yields equilibrium constants that depend on the excess. Moreover, the reverse process - as implied by thermodynamics - does not seem to happen.
On the other hand, diffusion through the crystal lattice has been considered as the rate limiting step in the exchange reaction. Fitting the shell thickness predicted by this diffusion model to our experimental data (figure 3.9) shows a reasonable correspondence at the beginning of the reaction. However, the fact that the reaction stops at a temperature dependent limiting shell thickness is not accounted for. This implies that another limiting factor has to be taken into account.
The fact that the exchange stops at a given depth into the QD could mean that, either the diffusion coefficient or the reaction rate constant for the Cd-Pb exchange gets altered as the reaction extends deeper in the PbX core. Variations on the diffusion coefficient could be caused by a steric hindrance of the diffusion process. Diffusion of ions might require certain crystal lattice dislocation which could get hampered as the same time as the reaction goes

deeper into the QD.
On the other hand, according to several research groups[33–36] the mean square displacement of atoms at the surface of the crystal lattice differs from that of the bulk atoms. Moreover, the mean square displacement approaches the bulk value very rapidly as going in from the surface. Therefore, this could be a possible explanation for variations in the reaction rate constant. This variation could halt the reaction after exchanging 2 or 3 layers.
The saturation of the shell thickness can be overcome by increasing the reaction temperature. Higher temperatures cause that the lattice atoms vibrate around the equilibrium lattice sites. Therefore, the probability that an atom in the bulk acquires sufficient energy to leave the lattice site augments. Hence, the exchange could progress deeper into the QD, leading to thicker shells.

3.6 Conclusions

Core/shell semiconductor nanocrystals have been receiving the spotlight due to their functionality and interesting opto-electronic properties. Several research groups have demonstrated that the composition of the nanocrystals can be altered by means of a cationic exchange reaction. This process can be tuned to obtain fully or only partially exchanged nanocrystals. Focusing on the latter and more specifically on PbX/CdX core/shell QDs, we can tuned the the thickness of the shell by modifying several reaction parameters. Variations on the reaction time or the excess of Cd lead to a certain shell thickness which reaches a saturation value after exchanging few atomic layers. Temperature is the only parameter that can be tuned to get thicker shells.
There are several attempts to explain the mechanism of the exchange reaction. After exploring them, we ruled out the one based on an equilibrium model since it predicted an excess depended reaction and it is proven not to be the case. On the other hand, a model based on diffusion is only valid for the first few atomic layers since it does not level off, for long reaction times, as the experimental data. This results indicates that another limiting factor has to be taken into account. In conclusion, we propose a diffusion model whose diffusion coefficient or reaction rate constant get altered as the reaction gets deeper into the QD. This could be cause by a a steric hindrance of the diffusion process or a

difference in mean square displacement between the atoms at the surface and that of the inner ones. An increase in temperature overcomes this drawback leading to thicker shells.

Bibliography

[1] Ghosh Chaudhuri, R.; Paria, S. Core/shell nanoparticles: classes, properties, synthesis mechanisms, characterization, and applications. *Chemical reviews* **2012**, *112*, 2373–433.

[2] Reiss, P.; Protière, M.; Li, L. Core/Shell semiconductor nanocrystals. *Small (Weinheim an der Bergstrasse, Germany)* **2009**, *5*, 154–68.

[3] Pietryga, J. M.; Werder, D. J.; Williams, D. J.; Casson, J. L.; Schaller, R. D.; Klimov, V. I.; Hollingsworth, J. A. Utilizing the lability of lead selenide to produce heterostructured nanocrystals with bright, stable infrared emission. *Journal of the American Chemical Society* **2008**, *130*, 4879–4885.

[4] Chin, P. T. K.; Donega, C. D. M.; van Bavel, S. S.; Meskers, S. C. J.; Sommerdijk, N. a. J. M.; Janssen, R. a. J. Highly luminescent CdTe/CdSe colloidal heteronanocrystals with temperature-dependent emission color. *Journal of the American Chemical Society* **2007**, *129*, 14880–6.

[5] Shi, W.; Zeng, H.; Sahoo, Y.; Ohulchanskyy, T. Y.; Ding, Y.; Wang, Z. L.; Swihart, M.; Prasad, P. N. A general approach to binary and ternary hybrid nanocrystals. *Nano letters* **2006**, *6*, 875–81.

[6] Talapin, D. V.; Nelson, J. H.; Shevchenko, E. V.; Aloni, S.; Sadtler, B.; Alivisatos, a. P. Seeded growth of highly luminescent CdSe/CdS nanoheterostructures with rod and tetrapod morphologies. *Nano letters* **2007**, *7*, 2951–9.

[7] Oldenburg, S.; Averitt, R.; Westcott, S.; Halas, N. Nanoengineering of optical resonances. *Chemical Physics Letters* **1998**, *288*, 243–247.

[8] Kalele, S.; Gosavi, S. W.; Urban, J.; K, K. S. Kalele_2006.pdf. *Current Science* **2006**, *91*, 1038–1052.

[9] Balakrishnan, S.; Bonder, M. J.; Hadjipanayis, G. C. Chemical reduction synthesis and ac field effect of iron based core-shell magnetic nanoparticles. *Journal of Physics D: Applied Physics* **2009**, *42*, 245005.

[10] Caruso, F. Nanoengineering of Particle Surfaces. *Advanced Materials* **2001**, *13*, 11–22.

[11] Daniel, M.-C.; Astruc, D. Gold nanoparticles: assembly, supramolecular chemistry, quantum-size-related properties,

and applications toward biology, catalysis, and nanotechnology. *Chemical reviews* **2004**, *104*, 293–346.

[12] Kortan, A. R.; Opila, R. L.; Bawendi, M. G.; Steigerwald, M. L.; Carroll, P. J.; Brus, L. E. Nucleation and Growth of CdSe on ZnS Quantum Crystallite Seeds , and Vice Versa , in Inverse Micelle Media u l l. *J. Am. Chem. Soc.* **1990**, *112*, 1327–1332.

[13] Mews, A.; Eychmiiller, A.; Giersig, M.; Schooss, D.; Weller, H. Preparation , Characterization , and Photophysics of the Quantum Dot Quantum Well System CdS/HgS/CdS. *J. Phys. Chem.* **1994**, *98*, 934–941.

[14] Hines, M. a.; Guyot-Sionnest, P. Synthesis and Characterization of Strongly Luminescing ZnS-Capped CdSe Nanocrystals. *The Journal of Physical Chemistry* **1996**, *100*, 468–471.

[15] Li, J. J.; Wang, Y. A.; Guo, W.; Keay, J. C.; Mishima, T. D.; Johnson, M. B.; Peng, X. Large-Scale Synthesis of Nearly Monodisperse CdSe / CdS Core / Shell Nanocrystals Using Air-Stable Reagents via Successive Ion Layer Adsorption and Reaction. *J. Am. Chem. Soc.* **2003**, 933–937.

[16] Brumer, M.; Kigel, a.; Amirav, L.; Sashchiuk, a.; Solomesch, O.; Tessler, N.; Lifshitz, E. PbSe/PbS and PbSe/PbSexS1-x Core/Shell Nanocrystals. *Advanced Functional Materials* **2005**, *15*, 1111–1116.

[17] Lifshitz, E.; Brumer, M.; Kigel, a.; Sashchiuk, a.; Bashouti, M.; Sirota, M.; Galun, E.; Burshtein, Z.; Le Quang, a. Q.; Ledoux-Rak, I.; Zyss, J. Air-stable PbSe/PbS and PbSe/PbSexS1-x core-shell nanocrystal quantum dots and their applications. *The journal of physical chemistry. B* **2006**, *110*, 25356–65.

[18] Sashchiuk, a.; Langof, L.; Chaim, R.; Lifshitz, E. Synthesis and characterization of PbSe and PbSe/PbS coreshell colloidal nanocrystals. *Journal of Crystal Growth* **2002**, *240*, 431–438.

[19] Xu, J.; Cui, D.; Zhu, T.; Paradee, G.; Liang, Z.; Wang, Q.; Xu, S.; Wang, A. Y. Synthesis and surface modification of PbSe/PbS coreshell nanocrystals for potential device applications. *Nanotechnology* **2006**, *17*, 5428–5434.

[20] Talapin, D.; Yu, H.; Shevchenko, E.; Lobo, a.; Murray, C. Synthesis of Colloidal PbSe/PbS Core-Shell Nanowires and

PbS/Au Nanowire-Nanocrystal Heterostructures. *Journal of Physical Chemistry C* **2007**, *111*, 14049–14054.

[21] Son, D. H.; Hughes, S. M.; Yin, Y. D.; Alivisatos, A. P. Cation exchange reactions-in ionic nanocrystals. *Science* **2004**, *306*, 1009–1012.

[22] Luther, J. M.; Zheng, H.; Sadtler, B.; Alivisatos, a. P. Synthesis of PbS nanorods and other ionic nanocrystals of complex morphology by sequential cation exchange reactions. *Journal of the American Chemical Society* **2009**, *131*, 16851–7.

[23] Deka, S.; Miszta, K.; Dorfs, D.; Genovese, A.; Bertoni, G.; Manna, L. Octapod-shaped colloidal nanocrystals of cadmium chalcogenides via "one-pot" cation exchange and seeded growth. *Nano letters* **2010**, *10*, 3770–6.

[24] Robinson, R. D.; Sadtler, B.; Demchenko, D. O.; Erdonmez, C. K.; Wang, L.-W.; Alivisatos, a. P. Spontaneous superlattice formation in nanorods through partial cation exchange. *Science (New York, N.Y.)* **2007**, *317*, 355–8.

[25] Li, H.; Zanella, M.; Genovese, A.; Povia, M.; Falqui, A.; Giannini, C.; Manna, Sequential Cation Exchange in Nanocrystals : Preservation of Crystal Phase and Formation of Metastable Phases. *Nano Lett.* **2011**, *11*, 4964–4970.

[26] Casavola, M.; Huis, M. A. V.; Bals, S.; Lambert, K.; Hens, Z.; Vanmaekelbergh, D. Anisotropic Cation Exchange in PbSe/CdSe Core/Shell Nanocrystals of Different Geometry. *Chemistry of Materials* **2012**, *24*, 294–302.

[27] Martell, A. E.; Hancock, R. D. Metal Complexes in Aqueous Solutions. In *Plenum Press: New York*; 1996.

[28] Pietryga, J. M.; Werder, D. J.; Williams, D. J.; Casson, J. L.; Schaller, R. D.; Klimov, V. I.; Hollingsworth, J. a. Utilizing the lability of lead selenide to produce heterostructured nanocrystals with bright, stable infrared emission. *Journal of the American Chemical Society* **2008**, *130*, 4879–85.

[29] Lambert, K.; De Geyter, B.; Moreels, I.; Hens, Z. PbTelCdTe CorelShell Particles by Cation Exchange, a HR-TEM study. *Chemistry of Materials* **2009**, *21*, 778–780.

[30] Moreels, I.; Lambert, K.; De Muynck, D.; Vanhaecke, F.; Poelman, D.; Martins, J. C.; Allan, G.; Hens, Z. Composition and Size-Dependent Extinction Coefficient of Colloidal PbSe Quantum Dots. *Chemistry of Materials* **2007**, *19*, 6101–6106.

[31] Moreels, I.; Lambert, K.; Smeets, D.; De Muynck, D.; Nollet, T.; Martins, J. C.; Vanhaecke, F.; Vantomme, A.; Delerue, C.; Allan, G.; Hens, Z. Size-dependent optical properties of colloidal PbS quantum dots. *ACS nano* **2009**, *3*, 3023–30.

[32] Ethayaraja, M.; Bandyopadhyaya, R. Model for CoreShell Nanoparticle Formation by Ion-Exchange Mechanism. *Industrial & Engineering Chemistry Research* **2008**, *47*, 5982–5985.

[33] Maradudin, A. A.; Melngailis J, Some dynamical properties of surface atoms. *Physical Review* **1964**, *133*, 1188–1193.

[34] Rich, M. Resonant gamma absorption near crystal surfaces. *Physics letters* **1963**, *4*, 153–155.

[35] Goodman, R. M. Mean Displacement of Surface Atoms in Palladium and Lead Single Crystals. *The Journal of Chemical Physics* **1968**, *48*, 1046.

[36] Wallis, R. F. Surface effects on lattice vibrations. *Surface science* **1964**, *2*, 146–155.

Chapter IV

Optical properties of PbSe/CdSe core/shell quantum dots.

4.1 Introduction

As compared to core quantum dots (QDs), core/shell QDs offer an enhanced stability and tunability of the optical and electronic properties. The additional tunability arises from the spatial distribution of the electron and hole wave function in QD heterostructures. Based on the bulk band alignment, three regimes of core/shell QDs can be distinguished in a quantum confined heterostructure, depending on the localization of the charge carrier wave functions (see figure 4.1) in an excited QD.

- In a type-I localization regime, where the band gap of the shell encompasses that of the core, the electron and hole are both localized in the core, resulting in chemically stable and well passivated QDs with high photoluminescence (PL) quantum yield (QY).

- In a type-II regime, characterized by a staggered band alignment, the electron and hole are spatially separated.

- In a quasi-type-II[1] localization regime, one of the carriers is fully delocalized over the core/shell heterostructure, while the other remains localized in the core.

As amply demonstrated with QD heterostructures emitting in the visible, this opens up new possibilities for engineering the intrinsic

opto-electronic properties of QDs. For instance, a five-fold reduction of the gain threshold was found with CdS/ZnSe dots, due to repulsive biexciton interaction of spatially separated excitons.[2] Similar effects, combined with a decrease in the Auger recombination rate were observed for CdTe/CdSe QDs.[3,4] For CdSe/CdTe heteronanocrystals[5,6] and ZnTe/ZnSe QDs,[7] long radiative lifetimes, indicative of charge separation, and a strong redshift of the exciton transitions were reported.

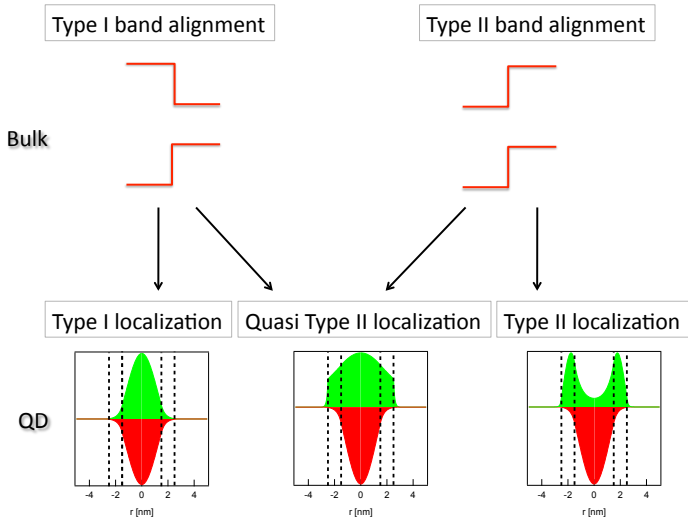

Figure 4.1: Core/shell QDs can be divided in three types, depending on the localization of the electron and hole wave function. In type-I, electron and hole are confined in the same region (either core or shell), in type-II, they are spatially separated. In a quasi-type-II one carrier is fully delocalized over the entire volume and one is localized in one region.

Previous work on colloidal type-II heteronanocrystals has focused primarily on compositions emitting in the visible spectral range. Colloidal core/shell heterostructures active in the near-infrared wavelength range (1000-3000 nm, NIR) have been scarcely investigated. For example, it has been recently shown that PbSe/PbS core/shell QDs with outer diameters below 10 nm behave like single composition QDs, where electron and hole are delocalized over the entire heterostructure.[8] Colloidal synthesis techniques were recently extended to concentric PbX/CdX (X=S,

Se, Te) core/shell QDs.[9,10] In this work we focus on PbSe/CdSe QDs, investigating their carrier distribution by absorption and photoluminescence (PL) spectroscopy and attempt to understand the electronic nature of the lowest absorbing and emitting states.

4.2 Experimental

4.2.1 Synthesis

PbSe synthesis Monodisperse colloidal PbSe QDs were synthesized based on the procedure developed by Murray et al.[11] It is carried out under a nitrogen atmosphere to avoid oxidation. In a three neck flask we add 26 ml of diphenyl eter and 1.8 mmol of lead oleate. The mixture is heated until the injection temperature, typically between 120 and 160℃, when we inject 5.7 mmol of TOPSe. To prepare this precursor, a mixture of TOP:Se in a 2:1 molar ratio is heated at 150℃ for 1 hour. Following the injection of the cold precursor solution, the temperature drops by approximately 10 ℃. The choice of the growth temperature is based on the final QD diameter aimed at. This temperature is maintained for 6 min. Hereafter, the reaction is quenched by addition of 10 ml of butanol (BuOH) and 5 ml of methanol (MeOH). This not only reduces the temperature to 70 ℃ it also induces the precipitation of the PbSe QDs formed. The precipitate is collected by centrifugation and decantation. To further remove impurities, the PbSe QDs are resuspended in 1 ml of toluene and 2 ml of methanol is added to precipitate the particles again. After a second centrifugation and decantation step, the QDs are suspended in 1 ml of toluene and stored under nitrogen. The ligand shell consists of oleic acid moieties (OA), as shown by nuclear magnetic resonance spectroscopy.[12]

PbSe/CdSe cation exchange PbSe/CdSe core-shell QDs were synthesized starting from PbSe core QDs by means of a cation exchange reaction.[9] In this reaction, an excess of Cd-oleate (0.3 M stock solution) is added to a PbSe QD suspension in toluene heated to a temperature between 100 and 160 ℃ . After reaching the desired reaction time (between 10-300 min), the reaction is quenched using a mixture of MeOH and BuOH (1:2) and precipitated twice. (see chapter III for the relation between reaction conditions and shell thickness)

4.2.2 Determination of the core diameter and concentration

Absorbance spectra are measured with a Perkin-Elmer Lambda 950 UV/VIS/NIR spectrophotometer. We use a black walled cuvet with a path length $L = 1$ cm. The QD diameter is determined from the spectral position of the first absorption peak and the PbSe sizing curve.[13] For the determination of the molar extinction coefficient (ϵ), care is taken to recover all QD material from the cation exchange step and to resuspend the resulting PbSe/CdSe core/shell QDs in the same volume. We assume the concentration of this suspension to be identical to that of the PbSe QD parent suspension. Equal volumes of PbSe and PbSe/CdSe QDs are taken, dried and dissolved in C_2Cl_4 to measure the absorbance A. After converting the absorption spectrum to a molar extinction coefficient spectrum, the first absorption peak was integrated on an energy scale between its low energy onset and its maximum. This value was doubled to obtain the values for ϵ_{gap}. Once ϵ_{gap} is determined, we are able to calculate concentration and absorption oscillator strength ($f_{if,abs}$) of any PbSe/CdSe QDs directly from its absorption spectrum.

4.2.3 Steady-state PL

The steady state photoluminescence (PL) is measured using an Edinburgh Instruments FS920 PL setup by excitation at 400 nm using a 450W Xenon lamp, coupled to a monochromator. The emitted light intensity is measured using a liquid N_2 cooled Ge detector, coupled to a monochromator. The PL spectra are corrected for detector and grating efficiency. The absorbance at 400 nm is kept below 0.1 cm^{-1} to avoid inhomogeneous spatial excitation and reabsorption.

4.2.4 Time-resolved PL

Luminescence decay curves were recorded under pulsed excitation with a Spectra-Physik LPD3000 dye laser at 480 nm pumped by a Lambda Physik LPX excimer laser. The Multi Channel Scaling (MCS) option integrated in the FLS920 spectrofluorometer was used to record the luminescence decay curves, using the IR-sensitive Hamamatsu R5509-72 photomultiplier tube. We measured 7 different PbSe/CdSe samples in C_2Cl_4. The samples

stemmed from three PbSe QD parent suspensions with diameter of 4.6 nm, 5.8 nm and 6.1 nm. The core diameters ranged between 2.5 and 4.2 nm. The average shell thickness was between 0.8 and 1.4 nm. With the lattice constant of cubic CdSe (0.6077 nm), this agrees with 2 to 4 monolayers of CdSe.

4.2.5 Determination of the Stokes shift

The PL spectrum was converted to an energy scale using the equation that relates wavelength and energy $E = \frac{hc}{\lambda}$ and fitted using a Gaussian curve. The absorption spectrum was fitted on an energy scale using a Gaussian curve and a polynomial background function. The Stokes shift was determined as the difference between the absorption energy and the luminescence energy from the fitting procedures.

4.3 Results

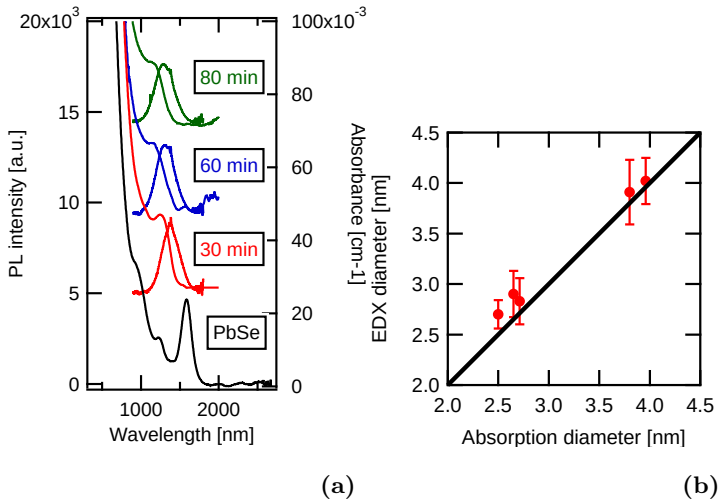

Figure 4.2: (a) Absorption and luminescence spectra of PbSe/CdSe QDs in C_2Cl_4 for increasing exchange times. (b) Diameter determined from EDX vs. diameter determined from the position of the first absorption peak, using the PbSe sizing curve. The black line indicates a 1-to-1 relationship.

4.3.1 Relation between absorption energy and core diameter

Knowledge of the core diameter and shell thickness is important for the present study of the QD optical and electronic properties. Although HR-TEM can be used for this purpose, it is not a practical technique for the analysis of a large number of samples in a short time span. Moreover, even when the boundary between core and shell can be distinguished, it is not clear whether to place it on a cation or anion plane. Therefore, we measured the Pb/Se ratio of the original PbSe core QDs and of the derived PbSe/CdSe QDs by TEM-based energy dispersive x-ray spectroscopy (EDX). Since the Se-content stays constant, we can thus calculate the amount of Pb in the PbSe/CdSe core, taking the nonstoichiometry [13,14] of the parent PbSe QDs into account. Since the stoichiometry of the PbSe core in PbSe/CdSe QDs is not known, we assume that it is terminated by Pb-planes and therefore has the stoichiometry of a PbSe QD with the same diameter. The resulting effective diameter of the PbSe core, determined with EDX, proves to be in good agreement with the diameter determined using the PbSe QD sizing curve [13] (see figure 4.2b). It shows that the Pb content of the PbSe/CdSe QD determines the bandgap. We thus conclude that the PbSe QD sizing curve can be used to estimate an effective diameter for the PbSe cores in PbSe/CdSe core/shell QDs.

4.3.2 Absorption oscillator strength

The first exciton transition is characterized by its energy and its oscillator strength $f_{if,abs}$. To obtain the oscillator strength, the spectrum of the absorbance (A) must be converted into the spectrum of the molar extinction coefficient ϵ. For this, the QD concentration c and the cuvette length L are needed (Beer's law):

$$\epsilon = \frac{A}{cL}$$

Under the assumption that the concentration of PbSe QDs before exchange, which can be calculated from the absorption spectrum, [13] does not change during shell growth, the spectrum of ϵ is readily obtained from the absorbance spectrum of a PbSe/CdSe suspension.

Having the ϵ spectrum for PbSe/CdSe QDs with different shell-volume-to-total-QD-volume ratios (V_{sh}/V_{QD}), $f_{if,abs}$ can be calcu-

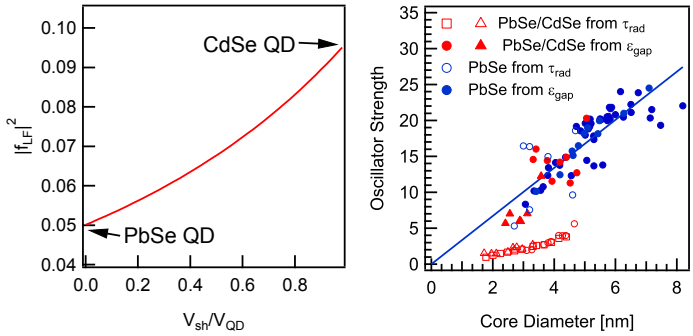

(a) **(b)**

Figure 4.3: (a) Local field factor at the band edge for PbSe/CdSe QDs as a function of the ratio V_{sh}/V_{QD}. (b) Absorption oscillator strength $f_{if,abs}$ for PbSe QDs (full blue markers) and PbSe/CdSe QDs (full red markers) and emission oscillator strength $f_{if,em}$ for PbSe QDs(empty blue markers) and PbSe/CdSe QDs (empty red markers) as a function of the core diameter. The red squares are values for PbSe/CdSe with a total diameter of 6.09 nm, the red dots a total diameter of 5.83 nm and the red triangles a total diameter of 4.57 nm.

lated from the energy-integrated molar extinction coefficient ϵ_{gap} of the first exciton transition. In analogy with calculations for PbSe[13] and PbS[15] QDs, $f_{if,abs}$ is obtained from the relation:

$$f_{if,abs} = \frac{2\epsilon_0 c m_e n_s}{\pi N_A \hbar e} \frac{1}{|f_{LF}|^2} \ln(10)\epsilon_{gap} \tag{4.1}$$

Here, ϵ_0 stands for the permittivity of the vacuum, c is the speed of light, m_e the electron mass, n_s the solvent refractive index (1.53 for C_2Cl_4), N_A Avogadro's constant, $\hbar$ Planck's constant, e the unit charge, f_{LF} the local field factor. Neeves and Birnboim[16] provide the following expression for $|f_{LF}|^2$ in the case of a core/shell particle:

$$|f_{LF}|^2 = \left| \frac{9\epsilon_{sh}\epsilon_s}{\epsilon_{sh}\epsilon_a + 2\epsilon_s\epsilon_b} \right|^2$$

with

$$\epsilon_a = \epsilon_c(3 - 2\frac{V_{sh}}{V_{QD}}) + 2\epsilon_{sh}\frac{V_{sh}}{V_{QD}}$$
$$\epsilon_b = \epsilon_c\frac{V_{sh}}{V_{QD}} + \epsilon_{sh}(3 - \frac{V_{sh}}{V_{QD}}) \tag{4.2}$$

Using the real part of the bulk permittivity of PbSe $\epsilon_c = 25.7$[17] and CdSe $\epsilon_{sh} = 8.3$,[18] we find that $|f_{LF}|^2$ gradually increases from the value for PbSe QDs to the value for CdSe QDs with increasing shell thickness (see figure 4.3a). Because of the significant broadening of the first exciton peak at long reaction times, ϵ_{gap} is obtained by fitting a series of Gaussian functions with a polynomial background function to the ϵ spectrum and taking the area under the first Gaussian function. The combination of $|f_{LF}|^2$ with the values for ϵ_{gap} enables us to calculate $f_{if,abs}$ of PbSe/CdSe QDs. Figure 4.3b shows that in the size range of 2.5 to 5 nm, we obtain similar values as a function of core diameter d_c as for PbSe QDs. This correspondence confirms that the nature of the first absorption feature remains largely unchanged when adding a shell of CdSe.

4.3.3 Steady-state and time-resolved PL

Next to the absorbance spectrum, figure 4.2a shows the PL spectrum for three different suspensions of PbSe/CdSe QDs. Due to the lack of efficient and reliable infrared reference dyes, the quantum yield (QY) is hard to determine. However, we can compare the total emission intensity of oleic acid capped PbSe/CdSe QDs with the total emission intensity of oleic acid capped PbSe QDs,[12] making sure to normalize them relative to the absorbance at the excitation wavelength and keeping all settings of the spectrofluorometer the same. This enables a relative comparison of the QY of different samples, without knowing its exact value (see figure 5.4). The QY for PbSe/CdSe QDs and PbSe QDs is comparable. Although a trend of increasing QY with decreasing core size is present for PbSe/CdSe QDs, the large scatter on these data suggests that sample preparation and surface quality have a large influence on the observed QY for PbSe/CdSe QDs.

We complemented the steady state PL results with PL lifetime measurements for different samples of PbSe/CdSe QDs, suspended

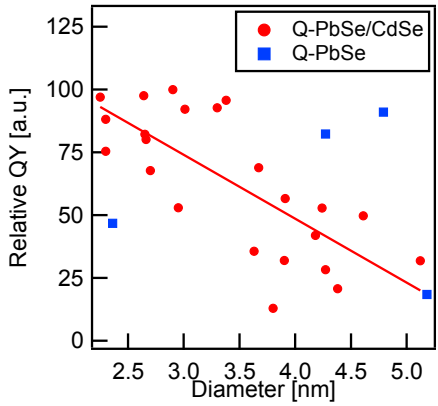

Figure 4.4: Relative QY for PbSe/CdSe (dots) and PbSe (squares) as a function of the core diameter. The line is a guide to the eye.

in C_2Cl_4. The steady-state PL spectrum was broadened considerably for all samples to about 250 nm (full width at half maximum). Hence each sample was probed at several wavelengths. Figure 4.5a shows a typical decay curve for PbSe/CdSe QDs and its PbSe QD parent. From this logarithmic plot, we clearly see that the PbSe QD decay is monoexponential. It is considerably faster than the decay of PbSe/CdSe QDs, which is not monoexponential.

From a single exponential fit to the decay curves of a 4.6 nm PbSe QD sample (see figure 4.5a), we obtain an experimental lifetime τ_0 of 0.969 ± 0.002 μs, 0.979 ± 0.002 μs and 1.067 ± 0.002 μs respectively at a wavelength of 1375, 1425 and 1500 nm. These results agree with the 1.04 μs measured by Kigel et al.[19] for 4.7 nm PbSe QDs in chloroform. The decay curves of the different PbSe/CdSe QD samples were fitted with a double exponential, a stretched exponential function and a lognormal distribution of decay rates.[20] The stretched exponential function and the lognormal distribution resulted in a much poorer fit than the double exponential function. For all samples, the double exponential fit yields two decay constants differing by about a factor of 10. However, the intensity (area under decay curve) of the slow decay was 5 to 20 times higher than the intensity of the fast decay. For this reason, we will focus our analysis on the slow component of the decay.

Figure 4.5b shows the results of the fit procedure (full green

squares, open red and blue markers). The lifetime differs significantly for different samples, ranging from 1.5 to 7 μs. The fact that PbSe/CdSe QDs from different suspensions, yet with comparable core diameters and shell thicknesses yield strongly different lifetimes suggests that the experimental lifetime τ_0 depends on the QY of each sample. In that case, the radiative lifetime τ_{rad} follows from:

$$\tau_0 = (\tau_{rad}^{-1} + \tau_{nrad}^{-1})^{-1} = \tau_{rad} QY \tag{4.3}$$

Since we are not able to determine the absolute QY, we cannot determine the τ_{rad} of the QDs. However, the relative QY allows us to rescale the values of τ_0, so we can compare the lifetimes of different QD suspensions. In figure 4.5b the arrows illustrate that by rescaling the lifetime of each of the open red and open blue markers to the QY of the sample with full green squares, we obtain a one-to-one relation between core size and lifetime. We note that these values, between 4 and 7 μs, are a lower limit of τ_{rad}. From figure 4.5b, we see that the lifetime decreases with increasing core diameter. This was predicted by Moreels et al.[15] using the molar extinction coefficient at the band gap for PbSe QDs up to 5 nm. Kigel et al.[19] measured a similar decreasing trend. For all wavelengths, the values are at least 4 to 6 times higher for PbSe/CdSe QDs than for PbSe QDs.[19,21,22]

From the lower limit of the radiative lifetime obtained above for PbSe/CdSe QDs and literature values for PbSe QDs,[19,21] we can calculate an upper limit of the oscillator strength $f_{if,PbSe/CdSe,em}$ and $f_{if,PbSe,em}$ of the emitting transition.

$$f_{if,em} = \frac{2\pi\epsilon_0 c^3 m_e}{e^2} \frac{g}{n_s |f_{LF}|^2 \omega^2} \tau_{rad}^{-1} \tag{4.4}$$

Dielectric screening will affect the radiative lifetime. Therefore we correct for this local field effect with f_{LF}. To compare the numbers calculated for $f_{if,em}$ with the oscillator strength obtained from the absorbance spectrum ($f_{if,abs}$), one should realize that $f_{if,abs}$ is the sum of the transition strengths of all g exciton states f_k:

$$f_{if,abs} = \sum_{k=1}^{g} f_k \tag{4.5}$$

The emission oscillator strength on the other hand is a Boltzmann

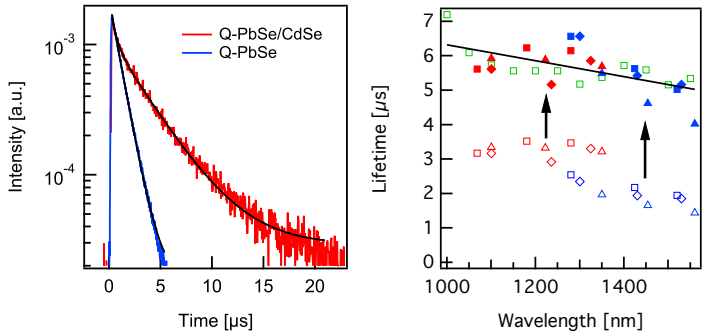

Figure 4.5: (a) Typical decay curve for PbSe/CdSe QDs and their PbSe QD parent, shown on a logarithmic scale. A single exponential fit is shown for PbSe and a biexponential fit for PbSe/CdSe. (b) Lifetime for 7 samples of PbSe/CdSe QDs. Each sample is probed at different wavelengths (markers with equal colour and symbol). Green squares have a PbSe QD parent diameter of 6.09 nm, blue markers a PbSe QD parent diameter of 5.83 nm and red markers a parent diameter of 4.57 nm. Open symbols give the decay constant for the slow component obtained from a bi-exponential fit to experimental decay curves. Closed symbols give the fitted values rescaled according to the QY of each individual sample, taking the sample with open green squares as the standard.

weighted average of the transition strength of each exciton state:[23]

$$f_{if,em} = g\frac{\sum_{k=1}^{g} f_k e^{\frac{-\Delta E_k}{kT}}}{\sum_{k=1}^{g} e^{\frac{-\Delta E_k}{kT}}} \tag{4.6}$$

Effectively, this yields the average transition strength of the states that contribute to emission. Since emission comes from radiative decay of a single exciton, which occupies only one of all possible ground exciton states, and absorption involves all exciton states, we multiply in 4.6 by the total number of exciton states $g = 64$ to obtain a total emission oscillator strength. One sees that $f_{if,em}$ should by equal to $f_{if,abs}$ as soon as $\Delta E_k \ll k_B T$.

The resulting values for $f_{if,PbSe/CdSe,em}$ and $f_{if,PbSe,em}$ are represented by the open markers in red and blue respectively in figure 4.3b. One sees that values smaller by at least 75% are found for the emission oscillator strength $f_{if,PbSe/CdSe,em}$.

4.3.4 PL quenching

The quantitative analysis of the absorption and luminescence data yields contradictory outcomes. While the energy and the absorption oscillator strength of the band gap transition in PbSe/CdSe are indicative of a type-I localization regime, the sensitivity of the emission QY and the increase in exciton lifetime associated with a decrease in emission oscillator strength suggest that one of the carriers is delocalized over the entire QD (quasi-type-II) or even localized in the CdSe shell (type-II). To pinpoint the localization regime, we added dodecanethiol (DDT), a well-known hole scavenger for CdSe[24,25] and PbSe[26,27] and methyl viologen (MV^{2+}), an electron scavenger,[28,29] to PbSe/CdSe suspensions and analyzed their effect on the photoluminescence.

Adding DDT (150μM) to a PbSe/CdSe suspension does not affect the QY (figure 4.6a). It redshifts the emission spectra by 20-40 nm (see figure 4.6b), indicating interaction of at least one of the charge carriers with the surface.[30,31] In contrast, addition of DDT to a PbSe QD sample resulted in significant quenching of the PL. Methylviologen dichloride was dissolved in isopropanol (IPA) and the MV^{2+}/IPA mixture was added in a 1:33 (v:v) ratio to obtain a 150μM MV^{2+} concentration. As a reference, we added the same amount of pure IPA to an identical QD sample, which resulted in a 50% drop of the QY. Adding the MV^{2+} mixture however

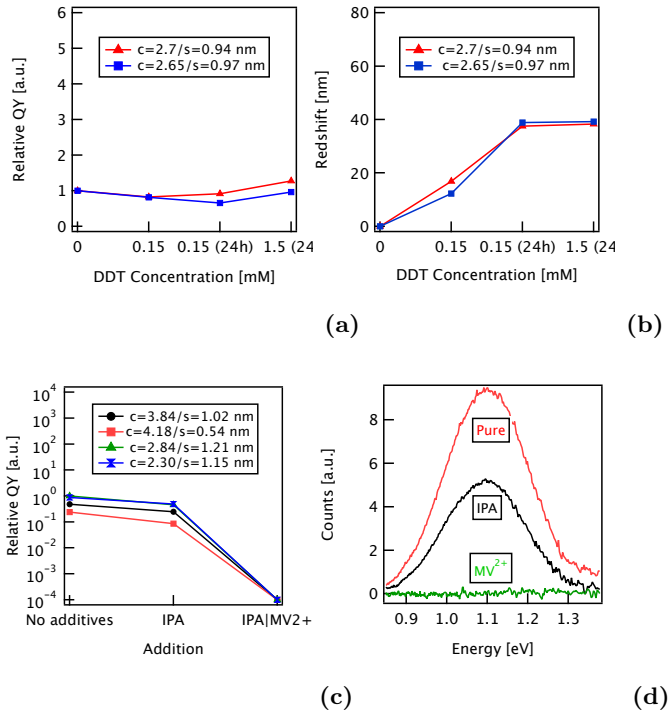

Figure 4.6: (a) Relative QY and (b) PL redshift before and after adding thiols (c) Relative QY (log-scale) and (d) PL spectra before and after adding IPA and MV^{2+}/IPA.

immediately quenches the PL signal to values below the detection limit (figures 4.6c and 4.6d). The same result was obtained for a PbSe QD reference sample. This shows that PbSe/CdSe QDs emit from a state in which the electron wave function reaches the surface and the hole wave function is well confined to the core. The delocalization of the electron will reduce the wavefunction overlap to some extent. However, these measurements are not sufficient to conclude that this reduction in overlap fully accounts for the reduction in emission oscillator strength. In addition, they do not explain why the absorption oscillator strength essentially remains unchanged.

4.3.5 Stokes shift

A splitting of the band edge in a lower energy dark and higher energy bright state due to the exchange interaction was predicted for

PbSe QDs by An et al.[23] This so-called exchange splitting however is only between 0 and 20 meV. Hence, at room-temperature these states are both populated due to thermal excitation, resulting in similar values for $f_{if,PbSe,abs}$ and $f_{if,PbSe,em}$. According to An *et al.*, the exchange splitting, together with the intervalley splitting, explains the non-resonant Stokes shift in PbSe QDs. Figure 4.7 shows the Stokes shift of PbSe QDs (blue squares) and PbSe/CdSe QDs (red dots) as a function of absorption energy or core size. Our values for PbSe QDs extrapolate well to the theoretical values reported for small QDs.[23,32,33]

Like the band gap energy, the PbSe/CdSe QD Stokes shift depends only on the core size, but it exceeds that for PbSe QDs by 50 to 100 meV. For small cores, it reaches a value of 200 meV. The molar extinction coefficient at energies well above the bandgap is typically volume dependent for colloidal QDs. Therefore a broad size distribution can result in a shift in the PL spectrum, because larger particles are excited more than smaller particles. For PbSe/CdSe QDs, De Geyter *et al*[34] already showed that the molar extinction coefficient is largely dependent on the total QD volume. Since the total volume and total size dispersion remain constant for these QDs throughout the exchange procedure,[9] we expect an increase in the Stokes shift due to non-uniform excitation of maximum 10 meV for the most broadened sample. The large Stokes shift is therefore not an artefact of size broadening, but due to an intrinsic physical effect.

Increased splitting in the fine structure will according to Boltzmann statistics result in an increased Stokes shift. This fine structure cannot be understood without extensive modelling. The nature of the interface, both in the real and in the reciprocal lattice (the band edge states are around the L-point for PbSe and the Γ-point for CdSe) probably has a strong influence on the electronic properties of these heterostructures. This could result in increased exchange and intervalley splitting, or might induce states at the PbSe/CdSe interface. For PbTe/CdTe however, theoretical calculations did not yield such interfacial states,[35] because the atomic structure of the lattice at the interface is virtually unperturbed.

Our results indicate that PbSe/CdSe QDs might have potential for applications in near infrared light sources, provided that further theoretical and experimental work reveals more of the intrinsic physical properties. In PbSe QDs the multi-exciton emis-

sion from the band edge, which at room temperature is essentially 8-fold degenerate, competes with the ps non-radiative Auger process. In PbSe/CdSe QDs, the emission apparently comes from lower energy states with a reduced oscillator strength. If these states are non-degenerate, like the lowest dark state of PbSe,[23] it would allow population inversion with less than one exciton per QD. This could mean a reduction in the continuous wave lasing threshold of up to 10^{-4}.

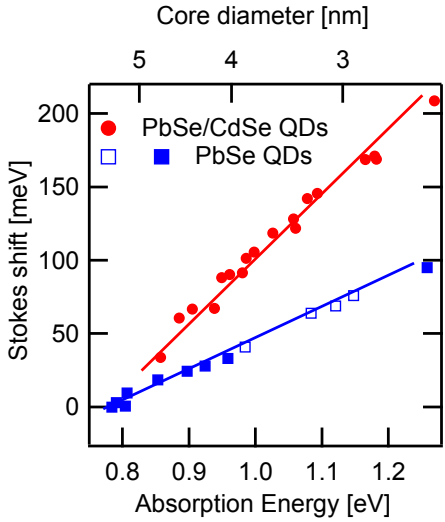

Figure 4.7: Stokes shift for PbSe QD (full and open blue squares)

4.4 Conclusion

In conclusion, we show that both the energy and the absorption oscillator strength of the first absorption peak in PbSe/CdSe quantum dots follow the same trend with core diameter as PbSe QDs. On the other hand, PL lifetime measurements yield an oscillator strength in emission that is reduced by at least 75%, compared to the PbSe/CdSe oscillator strength from absorption and the PbSe QD oscillator strength in absorption and emission. Moreover, the addition of an electron scavenger leads to a complete quenching of the PbSe/CdSe QD PL, while a hole scavenger does not. They show that the absorbing states essentially remain unchanged by the addition of a CdSe shell. However, they do not explain the

reduction of the oscillator strength of the band gap emission. In combination with the significantly increased Stokes shift, we conclude that the band gap emission in PbSe/CdSe QDs comes from fundamentally different states with lower oscillator strength that are energetically well separated from the absorbing states at room temperature. Moreover, these emitting states are different than the emitting states in PbSe QDs. Depending on the degeneracy of the emitting states, these binary heterostructures could allow lasing in the NIR wavelength range using single excitons.

Bibliography

[1] Ivanov, S. A.; Piryatinski, A.; Nanda, J.; Tretiak, S.; Zavadil, K. R.; Wallace, W. O.; Werder, D.; Klimov, V. I. Type-Ii Core/Shell Cds/Znse Nanocrystals: Synthesis, Electronic Structures, and Spectroscopic Properties. *J. Am. Chem. Soc.* **2007**, *129*, 11708–11719.

[2] Klimov, V. I.; Ivanov, S. A.; Nanda, J.; Achermann, M.; Bezel, I.; McGuire, J. A.; Piryatinski, A. Single-Exciton Optical Gain in Semiconductor Nanocrystals. *Nature* **2007**, *447*, 441–446.

[3] Oron, D.; Kazes, M.; Banin, U. Multiexcitons in Type-II Colloidal Semiconductor Quantum Dots. *Phys. Rev. B* **2007**, *75*, 35330.

[4] Dorfs, D.; Franzl, T.; Osovsky, R.; Brumer, M.; Lifshitz, E.; Klar, T. A.; Eychmueller, A. Type-I and Type-II Nanoscale Heterostructures Based on CdTe Nanocrystals: A Comparative Study. *Small* **2008**, *4*, 1148–1152.

[5] Jones, M.; Kumar, S.; Lo, S. S.; Scholes, G. D. Exciton Trapping and Recombination in Type II CdSe/CdTe Nanorod Heterostructures. *J. Phys. Chem. C* **2008**, *112*, 5423–5431.

[6] de Mello Donegá, C. Formation of Nanoscale Spatially Indirect Excitons: Evolution of the Type-II Optical Character of CdTe/CdSe Heteronanocrystals. *Phys. Rev. B* **2010**, *81*, 165303.

[7] Bang, J. et al. ZnTe/ZnSe (Core/Shell) Type-II Quantum Dots: Their Optical and Photovoltaic Properties. *Chem. Mater.* **2010**, *22*, 233–240.

[8] Bartnik, A. C.; Wise, F. W.; Kigel, A.; Lifshitz, E. Electronic Structure of PbSe/PbS Core-Shell Quantum Dots. *Phys. Rev. B* **2007**, *75*, 245424.

[9] Pietryga, J. M.; Werder, D. J.; Williams, D. J.; Casson, J. L.; Schaller, R. D.; Klimov, V. I.; Hollingsworth, J. a. Utilizing the lability of lead selenide to produce heterostructured nanocrystals with bright, stable infrared emission. *Journal of the American Chemical Society* **2008**, *130*, 4879–85.

[10] Zhang, Y.; Dai, Q.; Li, X.; Cui, Q.; Gu, Z.; Zou, B.; Wang, Y.; Yu, W. W. Formation of PbSe/CdSe Core/Shell Nanocrystals for Stable Near-Infrared High Photoluminescence Emission.

Nanoscale Res. Lett. **2010**, *5*, 1279–1283.

[11] Murray, C. B.; Sun, S. H.; Gaschler, W.; Doyle, H.; Betley, T. A.; Kagan, C. R. Colloidal Synthesis of Nanocrystals and Nanocrystal Superlattices. *IBM J. Res. Dev.* **2001**, *45*, 47–56.

[12] Moreels, I.; Fritzinger, B.; Martins, J. C.; Hens, Z. Surface Chemistry of Colloidal PbSe Nanocrystals. *J. Am. Chem. Soc.* **2008**, *130*, 15081–15086.

[13] Moreels, I.; Lambert, K.; De Muynck, D.; Vanhaecke, F.; Poelman, D.; Martins, J. C.; Allan, G.; Hens, Z. Composition and Size-Dependent Extinction Coefficient of Colloidal PbSe Quantum Dots. *Chem. Mater.* **2007**, *19*, 6101–6106.

[14] Dai, Q.; Wang, Y.; Li, X.; Zhang, Y.; Pellegrino, D. J.; Zhao, M.; Zou, B.; Seo, J.; Wang, Y.; Yu, W. W. Size-Dependent Composition and Molar Extinction Coefficient of PbSe Semiconductor Nanocrystals. *ACS Nano* **2009**, *3*, 1518–1524.

[15] Moreels, I.; Lambert, K.; Smeets, D.; De Muynck, D.; Nollet, T.; Martins, J. C.; Vanhaecke, F.; Vantomme, A.; Delerue, C.; Allan, G.; Hens, Z. Size-Dependent Optical Properties of Colloidal PbS Quantum Dots. *ACS Nano* **2009**, *3*, 3023–3030.

[16] Neeves, A.; Birnboim, M. Composite Structures for the Enhancement of Nonlinear-Optical Susceptibility. *J. Opt. Soc. Am. B* **1989**, *6*, 787–796.

[17] Suzuki, N.; Sawai, K.; Adachi, S. Optical Properties of PbSe. *J. Appl. Phys.* **1995**, *77*, 1249–1255.

[18] Ninomiya, S.; Adachi, S. Optical Properties of Cubic and Hexagonal Cdse. *J. Appl. Phys.* **1995**, *78*, 4681–4689.

[19] Kigel, A.; Brumer, M.; Maikov, G. I.; Sashchiuk, A.; Lifshitz, E. Thermally Activated Photoluminescence in Lead Selenide Colloidal Quantum Dots. *Small* **2009**, *5*, 1675–1681.

[20] van Driel, A. F.; Nikolaev, I. S.; Vergeer, P.; Lodahl, P.; Vanmaekelbergh, D.; Vos, W. L. Statistical Analysis of Time-Resolved Emission from Ensembles of Semiconductor Quantum Dots: Interpretation of Exponential Decay Models. *Phys. Rev. B* **2007**, *75*, 35329.

[21] Schaller, R. D.; Crooker, S. A.; Bussian, D. A.; Pietryga, J. M.; Joo, J.; Klimov, V. I. Revealing the Exci-

ton Fine Structure of PbSe Nanocrystal Quantum Dots Using Optical Spectroscopy in High Magnetic Fields. *Phys. Rev. Lett.* **2010**, *105*, 67403.

[22] Oron, D.; Aharoni, A.; Donega, C. d. M.; van Rijssel, J.; Meijerink, A.; Banin, U. Universal Role of Discrete Acoustic Phonons in the Low-Temperature Optical Emission of Colloidal Quantum Dots. *Phys. Rev. Lett.* **2009**, *102*, 177402.

[23] An, J. M.; Franceschetti, A.; Zunger, A. The Excitonic Exchange Splitting and Radiative Lifetime in Pbse Quantum Dots. *Nano Lett.* **2007**, *7*, 2129–2135.

[24] Aldana, J.; Wang, Y. A.; Peng, X. G. Photochemical Instability of CdSe Nanocrystals Coated by Hydrophilic Thiols. *J. Am. Chem. Soc.* **2001**, *123*, 8844–8850.

[25] Wuister, S. F.; Donega, C. D.; Meijerink, A. Influence of Thiol Capping on the Exciton Luminescence and Decay Kinetics of CdTe and CdSe Quantum. *J. Phys. Chem. B* **2004**, *108*, 17393–17397.

[26] Wang, C.; Kwon, K.-W.; Odlyzko, M. L.; Lee, B. H.; Shim, M. Pbse Nanocrystal/TiOx Heterostructured Films: A Simple Route to Nanoscale Heterointerfaces and Photocatalysis. *J. Phys. Chem. C* **2007**, *111*, 11734–11741.

[27] Luther, J. M.; Law, M.; Song, Q.; Perkins, C. L.; Beard, M. C.; Nozik, A. J. Structural, Optical, and Electrical Properties of Self-Assembled Films of PbSe Nanocrystals Treated with 1,2-Ethanedithiol. *ACS Nano* **2008**, *2*, 271–280.

[28] Burda, C.; Green, T. C.; Link, S.; El-Sayed, M. A. Electron Shuttling across the Interface of Cdse Nanoparticles Monitored by Femtosecond Laser Spectroscopy. *J. Phys. Chem. B* **1999**, *103*, 1783–1788.

[29] Matylitsky, V. V.; Dworak, L.; Breus, V. V.; Basche, T.; Wachtveitl, J. Ultrafast Charge Separation in Multiexcited CdSe Quantum Dots Mediated by Adsorbed Electron Acceptors. *J. Am. Chem. Soc.* **2009**, *131*, 2424–2425.

[30] Koole, R.; Luigjes, B.; Tachiya, M.; Pool, R.; Vlugt, T. J. H.; Donega, C. D. M.; Meijerink, A.; Vanmaekelbergh, D. Differences in Cross-Link Chemistry between Rigid and Flexible Dithiol Molecules Revealed by Optical Studies of CdTe Quantum Dots. *J. Phys. Chem. C* **2007**, *111*, 11208–11215.

[31] Talgorn, E.; Moysidou, E.; Abellon, R. D.; Savenije, T. J.;

Goossens, A.; Houtepen, A. J.; Siebbeles, L. D. A. Highly Photoconductive CdSe Quantum-Dot Films: Influence of Capping Molecules and Film Preparation Procedure. *J. Phys. Chem. C* **2010**, *114*, 3441–3447.

[32] Leitsmann, R.; Bechstedt, F. Characteristic Energies and Shifts in Optical Spectra of Colloidal IV-VI Semiconductor Nanocrystals. *ACS Nano* **2009**, *3*, 3505–3512.

[33] Franceschetti, A. Structural and Electronic Properties of PbSe Nanocrystals from First Principles. *Phys. Rev. B* **2008**, *78*, 75418.

[34] De Geyter, B.; Hens, Z. The Absorption Coefficient of PbSe/CdSe Core/shell Colloidal Quantum Dots. *Appl. Phys. Lett.* **2010**, *97*, 161908.

[35] Leitsmann, R.; Bechstedt, F.; Groiss, H.; Schaeffler, F.; Heiss, W.; Koike, K.; Harada, H.; Yano, M. Structural and Electronic Properties of PbTe (Rocksalt)/CdTe (Zinc-Blende) Interfaces. *Appl. Surf. Sci.* **2007**, *254*, 397–400.

Chapter V

Optical properties of PbS/CdS core/shell quantum dots

5.1 Introduction

Colloidal near-infrared (NIR) emitting quantum dots (QDs) are very attractive in a variety of potential applications, such as lasing,[1] photovoltaics[2,3] and biological labeling.[4] For most of the practical applications it is essential that the QDs have a high photoluminescence quantum yield (QY) and a long term chemical stability. Simple core lead chalcogenide (PbX, X=S, Se or Te) QDs however show a progressive blueshift of their photoluminescence (PL) and a reduction of the PLQY when continuously exposed to ambient conditions, which is a strong indication of surface oxidation.[5]

As initially demonstrated with CdSe/ZnS, the growth of an inorganic shell is a viable method to protect a core QD from oxidation and increase and stabilize its PLQY.[6] In the case of PbSe, CdSe shell growth by cationic exchange was demonstrated for the first time by Pietryga et al.[7] and the resulting PbSe/CdSe core/shell QDs have been extensively discussed in chapter III of this thesis. Importantly, we found that shell growth not only stabilizes the QDs but it also alters the opto-electronic properties of the original PbSe QDs.[8,9]

In this chapter, we extend the analysis of the optical properties to PbS/CdS QDs. Again, we find that the PbS sizing curve can be used for an accurate estimation of the PbS core diameter in PbS/CdS core/shell QDs and that the PbS/CdS absorption

coefficient at short wavelengths coincides with the value predicted using the Maxwell-Garnett model in the local field approximation. Using this as a starting point, we compare the oscillator strength of the PbS/CdS bandgap transitions as obtained from absorption and luminescence lifetime measurements. In this case, no marked differences between PbS and PbS/CdS QDs are observed, which leads us to the conclusion that CdS shell growth around a PbS core leads to a simple type I core/shell structure.

5.2 Experimental

5.2.1 Synthesis

PbS synthesis Oleylamine (OLA) capped PbS QDs were synthesized using a procedure adapted to the one originally developed by Cademartiri et al.[10] and described in detail in Chapter II.

PbS/CdS cation exchange PbS/CdS core-shell QDs were synthesized starting from PbS core QDs by means of a cation exchange reaction initially proposed by Pietryga et al.[7] The reaction conditions are explained in detail in Chapter III.

5.2.2 Characterization

Absorption spectroscopy The absorbance of the colloidal solutions and thin films was determined by means of a Perkin Elmer Lambda 950 UV-vis-NIR spectrophotometer

Photoluminescence spectroscopy For measuring photoluminescence (PL) spectra, a FS920 luminescence spectrofluorometer (Edinburgh Instruments) was used. Samples were excited at 400 nm.

Time-resolved photoluminescence Luminescence decay curves were recorded with a Spectra-Physik LPD3000 dye laser at 480 nm pumped by a Lambda Physik LPX excimer laser. The Multi Channel Scaling (MCS) option integrated in the FLS920 spectrofluorometer was used to record the luminescence decay curves, using the IR-sensitive Hamamatsu R5509-72 photomultiplier tube.

ICP-MS measurements Inductively coupled plasma mass spectrometry (ICP-MS) measurements were performed with a PerkinElmer SCIEX Elan 5000 inductively coupled plasma mass spectrometer. ICP-MS measurements were performed by Karen Van Hoecke at the A&MS (Atomic and mass spectrometry) unit of Prof. Dr. Frank Vanhaecke at Ghent University.

5.3 Results

5.3.1 ICP-MS measurements

Similar to PbSe/CdSe QDs, knowledge of the shell thickness is essential to understand the opto-electronic properties of PbS/CdS QDs. As mentioned in the previous chapter, HR-TEM can be used to analyze the shell thickness, yet it is laborious and not very accurate due to the difficulty to distinguish the end of the core and the beginning of the shell.[11] Here we use elemental analysis by ICP-MS to determine the amount of Pb and Cd in a sample of core/shell QDs. From these amounts, core diameter and shell thickness are calculated, assuming that the core/shell particle consists of a spherical core with a concentric, spherical shell.

For elemental analysis, seven ICP-MS samples were prepared by drying a known amount of PbS/CdS QDs under a nitrogen flow and digesting them in 15 mL of HNO_3. We determined both the Pb (C_{Pb}) and the Cd (C_{Cd}) weight concentrations in these samples. Based on the resulting values, equations 5.1 and 5.2 were used to calculate the volume of the CdS shell ($V_s = V_{\mathrm{CdS}}$) and the total volume of PbS and CdS ($V_{tot} = V_{\mathrm{CdS}} + V_{\mathrm{PbS}}$) in the sample. To calculate V_{CdS} and V_{PbS}, we assume that the CdS shell is stoichiometric, while the core has a fixed (size-independent) Pb:S ratio of 1.2:1. Subsequently, the shell thickness δ was calculated from the ratio V_s/V_{tot} and equation 5.3. Table 5.1 summarizes the results.

$$V_{\mathrm{CdS}} = V_s = V_{\mathrm{Cd}} + V_{\mathrm{S}_{(\mathrm{Cd})}} = \frac{a^3}{4} N_{\mathrm{Cd}} \tag{5.1}$$

$$V_{\mathrm{PbS}} = V_{\mathrm{Pb}} + V_{\mathrm{S}_{(\mathrm{Pb})}} = \frac{a^3}{8} N_{\mathrm{Pb}} + \frac{a^3}{8} \frac{N_{\mathrm{Pb}} - 0.2 N_{\mathrm{Cd}}}{1.2} \tag{5.2}$$

d (nm)	Temp ℃	C_{Pb}(mg)	C_{Cd}(mg)	V_s/V_{tot}	δ (nm)
4	100	98.75	137.98	0.64	0.57
4	130	44.5	149.56	0.84	0.92
5.5	100	81.75	71.96	0.51	0.58
5.5	130	70	140.25	0.73	0.97
7	100	87.5	58.86	0.44	0.62
7	130	70	68.49	0.54	0.81
7	150	36.75	69.35	0.71	1.21

Table 5.1: ICP-MS results on seven PbS/CdS QDs samples with different diameters and ratio V_s/V_{tot}. Shell thickness values obtained from the ICP-MS measurements.

In equations 5.1 and 5.2, $V_{\mathrm{S}_{(\mathrm{Cd})}}$ and $V_{\mathrm{S}_{(\mathrm{Pb})}}$ are the volumes of sulfur bound to either Cd or Pb. N_{Cd} and N_{Pb} are the number of Cd and Pb atoms, a is the CdS or PbS lattice constant and d is the diameter of the entire nanocrystal.

$$\delta = \left(1 - \left(1 - \frac{V_s}{V_{tot}}\right)^{1/3}\right)\frac{d}{2} \tag{5.3}$$

5.3.2 Relation between absorption energy and core diameter

The difference between the nanocrystal diameter d and the shell thickness δ as determined according to equation 5.3 yields the diameter of the PbS core for each of the samples analysed by ICP-MS. Alternatively, the core diameter can be estimated using the wavelength of the first exciton transition in combination with the PbS sizing curve.[12] In figure 5.1, we plot the latter (absorption diameter) as a function of the former (ICP-MS diameter). The figure shows that both diameters are in good agreement. Hence, the PbS core diameter of PbS/CdS QDs can be accurately determined from the QD absorption spectrum by using the PbS sizing curve.

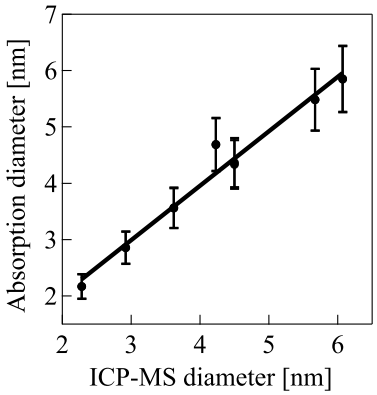

Figure 5.1: Diameter determined from ICP-MS vs diameter determined from the absoption peak, using PbS sizing curve.

5.4 The absorption coefficient of PbS/CdS

The intrinsic absorption coefficient μ_i relates the volume fraction f occupied by the QDs in a dispersion to the absorbance A of that dispersion:

$$\mu_i = \frac{A \ln(10)}{fL} \tag{5.4}$$

Here, L denotes the optical pathlength through the sample. If the volume V_{QD} of a single QD is known, equation 5.4 can be rewritten to yield the QD concentration [QD] (N_A: Avogadro's number):

$$[\mathrm{QD}] = \frac{A \ln(10)}{\mu_i N_A V_{QD} L} \tag{5.5}$$

From the ICP-MS data, the volume fraction of QDs f can be calculated and thus, using equation 5.4, values for μ_i can be determined. The resulting experimental values at 400 and 350 nm are plotted in figure 5.2 as a function of the ratio V_s/V_{tot}.

For core/shell QDs, a theoretical expression for the intrinsic absorption coefficient in the case of small QD volume fractions

has been proposed by Neeves *et al.*[13]

$$\mu_i = \frac{2\pi}{\lambda n_s} Im(3\epsilon_s \beta)$$

$$with \qquad \beta = \left(\frac{\epsilon_{sh}\epsilon_a - \epsilon_s \epsilon_b}{\epsilon_{sh}\epsilon_a + 2\epsilon_s \epsilon_b} \right),$$

$$\epsilon_a = \epsilon_c \left(3 - 2\frac{V_s}{V_{tot}} \right) + 2\epsilon_{sh} \frac{V_s}{V_{tot}}$$

$$\epsilon_b = \epsilon_c \frac{V_s}{V_{tot}} + \epsilon_s \left(3 - \frac{V_s}{V_{tot}} \right) \tag{5.6}$$

The expression shows that in the case of core/shell QDs, μ_i depends on V_s/V_{tot} and on the dielectric functions of the core (ϵ_c), the shell (ϵ_{sh}) and the surroundings (ϵ_s). For various core QDs, it has been shown that the experimental absorption coefficient agrees well with a theoretical value calculated using the dielectric function of the bulk material. In the same way, we calculate a theoretical absorption coefficient for PbS/CdS QDs at 400 and 350 nm using the dielectric function of bulk PbS and bulk CdS in equation 5.6.[14,15] The results are represented by the full lines in figure 5.2. For thin shells, we find that μ_i slightly increases. After reaching a maximum value at $V_s/V_{tot} \approx 0.2$, it rapidly decreases for thicker shells. Clearly, a good agreement is obtained between these theoretical values and the experimental data based on ICP-MS analysis. We therefore recommend to use $\mu_{400,th}$ as a function of V_s/V_{tot} to calculate the volume fraction or the concentration of dispersed PbS/CdS core/shell QDs.

5.5 Steady-state and time-resolved photoluminescence

Figure 5.3 shows the absorption and emission spectra of 5.5 nm PbS QDs and two samples of PbS/CdS core/shell QDs made from it. Both the absorption and emission peak of the PbS/CdS core/shell QDs shift towards shorter wavelengths as the shell gets thicker. The PLQY of the PbS and PbS/CdS QDs was determined

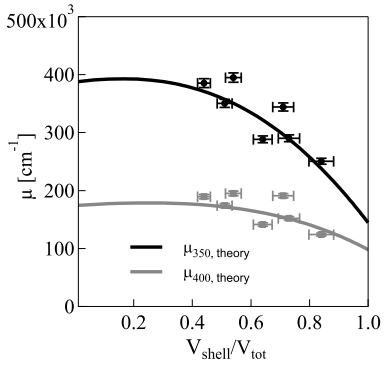

Figure 5.2: Intrinsic absorption coefficient at 350nm and 400nm for PbS/CdS core/shell QDs as predicted by theory (line) and as measured (squares and circles)

by means of an integrating sphere.[16?] As for PbSe, figure 5.4 shows that the QY for PbS/CdS QDs is comparable to that of PbS QDs. Despite the large scatter on the data, the trend shows that the PLQY decreases with the increasing core size. We also studied the luminescence lifetime of different PbS and PbS/CdS samples. Figure 5.5 shows a typical decay curve for PbS and PbS/CdS QDs plotted on a logarithmic scale. Both decays fit to a single exponential function, making the analysis of the results easier than for PbSe/CdSe QDs. The lifetime of several samples of PbS and PbS/CdS QDs with different PbS core diameters is summarized in figure 5.6a. Typical values range between 1 and 3 μs, where both for PbS and PbS/CdS QDs, smaller cores yield longer lifetimes. Moreover, the coinciding lifetimes of PbS and PbS/CdS QDs with identical PbS cores indicates that the electron and hole in a PbS/CdS core/shell QD are both confined inside the PbS core in a type-I regime.

In figure 5.6a, radiative lifetimes are plotted without dividing by the PLQY to correct for possible non-radiative decay paths. If applied, this correction introduces considerable scatter on the radiative lifetimes (5.6b). This indicates that the assumptions behind this correction - a homogeneous sample where radiative and non-radiative decay compete in each nanocrystal - is not correct. Since samples with considerably different PLQY yield similar lifetimes, we conclude that the radiative lifetime is directly measured in this case, possible since samples are a mixture of non-emitting QDs and QDs with a PLQY of 100%.

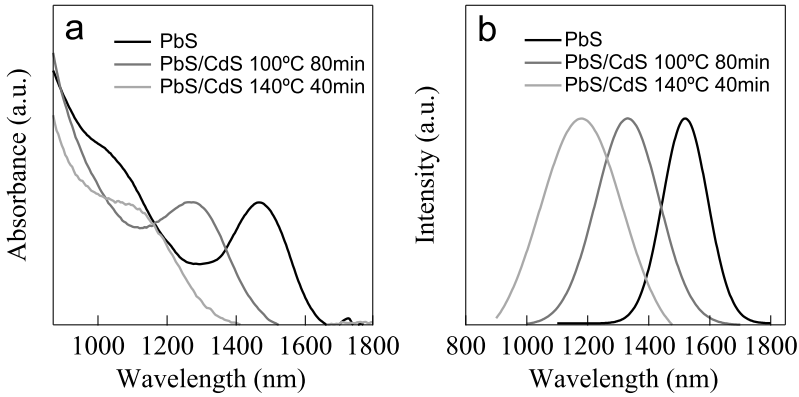

Figure 5.3: a) Absorption spectra of PbS and PbS/CdS QDs. b) Emission spectra of PbS and PbS/CdS QDs.

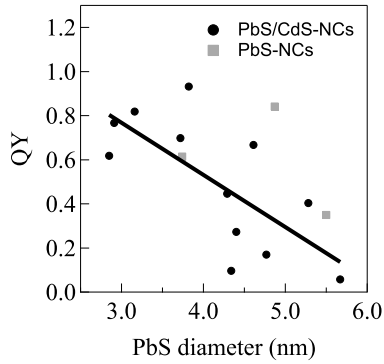

Figure 5.4: Quantum yield of PbS and PbS/CdS QDs as a function of PbS diameter.

5.6 Oscillator strength

5.6.1 Absorption oscillator strength.

Two key characteristics of the first exciton transition are its energy and its oscillator strength ($f_{if,abs}$). To obtain $f_{if,abs}$, both the spectrum of the absorption coefficient and the QD diameter or the QD volume must be known:

$$f_{if,abs} = \frac{2\epsilon_0 c m_e n_s}{e\pi\hbar} \frac{V_{QD}}{|f_{LF}|^2} \mu_{i,gap} \tag{5.7}$$

Here, ϵ_0 stands for the permittivity of the vacuum, c is the speed of

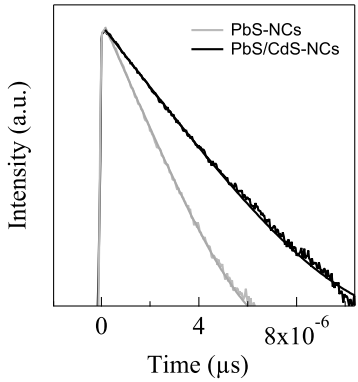

Figure 5.5: Quantum yield of PbS and PbS/CdS QDs as a function of PbS diameter.

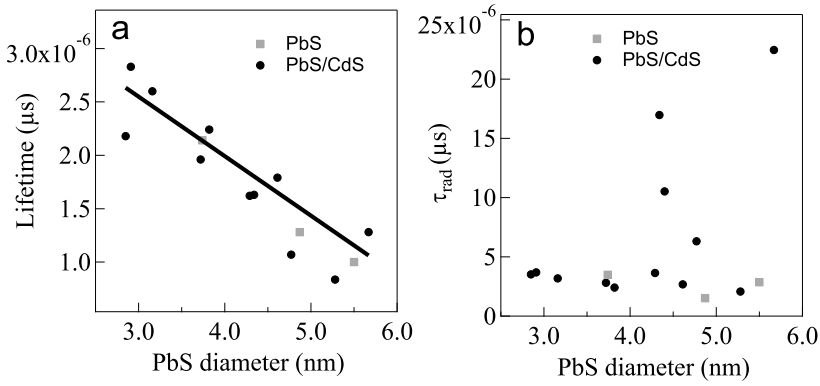

Figure 5.6: Quantum yield of PbS and PbS/CdS QDs as a function of PbS diameter.

light, m_e the electron mass, n_s the solvent refractive index (1.53 for C_2Cl_4), $\hbar$ Planck's constant, e the unit charge, f_{LF} the local field factor and $\mu_{i,gap}$ is the energy integrated absorption coefficient of the first exciton transition. To calculate $|f_{LF}|^2$ at 400 nm, the same expression as in chapter IV is used. As for PbSe/CdSe QDs, we find that $|f_{LF}|^2$ increases with the shell thickness (figure 5.7). To obtain $\mu_{i,gap}$, the spectrum of A must be converted into the spectrum of the intrinsic absorption coefficient (μ_i) by multiplying it by the ratio $\mu_{400,th}/A_{400}$ for each V_s/V_{tot} (figure 5.2).

The thus calculated absorption oscillator strength $f_{if,abs}$ of PbS/CdS core/shell QDs is plotted in figure 5.8a, showing higher

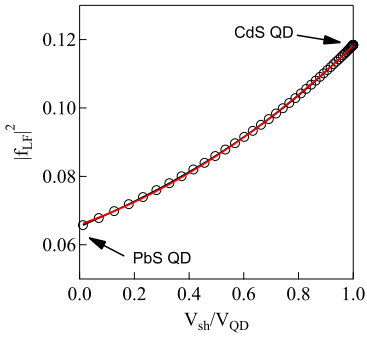

Figure 5.7: Local field factor for PbS/CdS at 400 nm as a function of V_{sh}/V_{QD}.

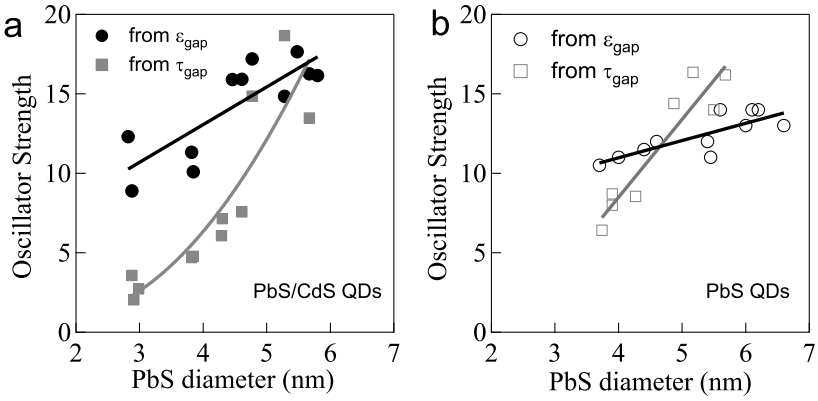

Figure 5.8: a) $f_{if,abs}$ and $f_{if,em}$ of PbS/CdS core/shell QDs. b) $f_{if,abs}$ and $f_{if,em}$ of PbS QDs.

values for larger core sizes. A comparison with literature values for PbS[12] (figure 5.8b) shows that similar values, albeit slightly larger for PbS/CdS, are obtained. This could be due to the fact that the more pronounced peak broadening in the case of PbS/CdS leads to an overestimation of $f_{if,abs}$.

5.6.2 Emission oscillator strength.

The radiative lifetime of the first exciton can also be linked to the oscillator strength of the bandgap transition. Under the assumption that all fine structure levels of the first exciton are equally accessible, the oscillator strength of the emitting transition – de-

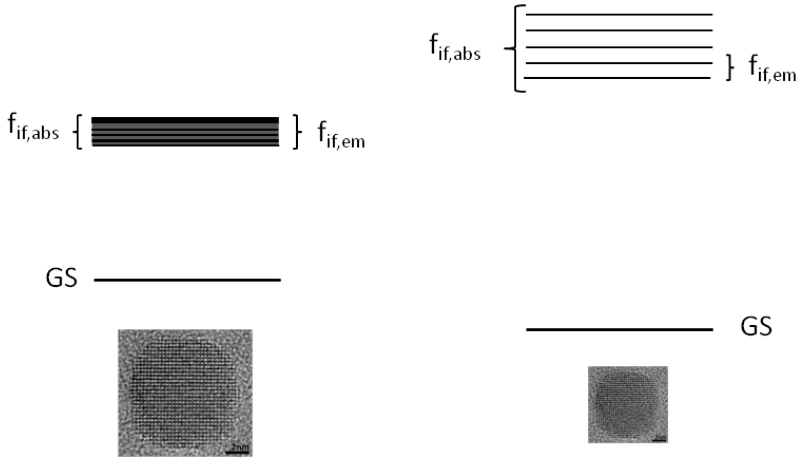

Figure 5.9: Scheme of the interpretation of the results on $f_{if,abs}$ and $f_{if,em}$.

noted as $f_{if,em}$ – is obtained as:

$$f_{if,em} = \frac{2\pi\epsilon_0 c^3 m_e}{e^2} \frac{g}{n_s \left|f_{LF}\right|^2 \omega^2} \tau_{rad}^{-1} \tag{5.8}$$

Here, $|f_{LF}|^2$ corrects the measured radiative lifetime for the dielectric screening by the shell and the solvent. Since in absorption all possible exciton states are addressed in parallel, while the emission occurs from one particular exciton state, the radiative recombination rate is multiplied by the degeneracy g of the first exciton. Doing so, a value is obtained that can be compared directly to $f_{if,abs}$.

Figure 5.8a shows $f_{if,em}$ for PbS/CdS QDs as obtained from the radiative lifetime. For diameters smaller than 5 nm, $f_{if,em}$ is markedly smaller than $f_{if,abs}$. In contrast, both values coincide for diameters larger than 5 nm. Returning to equation 5.8, the coincidence $f_{if,em}$ and $f_{if,abs}$ indicates that for these larger sizes, the energy spacing between the different first exciton levels is comparable to or smaller than thermal energy, *i.e.*, all first exciton states are equally accessible (see figure 5.9a). On the other hand, for sizes smaller than 5 nm, the increasing level spacing results in an exciton trapped in a subset of first exciton states with a smaller oscillator strength (see figure 5.9b). A similar trend is found for PbS QDs, although the reduction of $f_{if,em}$ is less pronounced. This again confirms that CdS shell growth leaves

the optical properties of the PbS core largely unchanged.

5.7 Conclusions

In this chapter we studied the optical properties of PbS/CdS QDs. The results show, as for PbSe/CdSe QDs, that the PbS sizing curve can be used to estimate the diameter of the core and therefore, to obtain the shell thickness. The intrinsic absorption coefficient, predicted using the Maxwell-Garnett model, and calculated as a function of V_s/V_{tot}, coincides with that of the experimental samples whose f has been obtained by ICP-MS. Therefore, we can use $\mu_{400,th}$ as a function of V_s/V_{tot} to calculate the volume fraction or the concentration of dispersed PbS/CdS core/shell QDs. Regarding the time-resolved PL, for PbS and PbS/CdS QDs, smaller cores yield longer lifetimes with typical values between 1 and 3 μs. $f_{if,abs}$ and $f_{if,em}$ values coincide for PbS/CdS QDs with d>5 nm. However, for smaller sizes, $f_{if,em}$ is markedly smaller than $f_{if,abs}$. This indicates that the exciton is trapped in states with lower oscillator strength due to an increase on level spacing. A similar trend, although less pronounced, is also found for PbS QDs.
In summary, the coinciding lifetimes of PbS and PbS/CdS QDs with identical PbS cores and similar oscillator strength trends, indicate that the electron and hole in a PbS/CdS core/shell QD are both confined inside the PbS core. Hence, we can conclude that the CdS shell growth around the PbS core leads to a simple type-I regime.

Bibliography

[1] Hoogland, S.; Sukhovatkin, V.; Howard, I.; Cauchi, S.; Levina, L.; Sargent, E. H. A solution-processed 1.53 mum quantum dot laser with temperature-invariant emission wavelength. *Optics express* **2006**, *14*, 3273–81.

[2] Tang, J.; Kemp, K. W.; Hoogland, S.; Jeong, K. S.; Liu, H.; Levina, L.; Furukawa, M.; Wang, X.; Debnath, R.; Cha, D.; Chou, K. W.; Fischer, A.; Amassian, A.; Asbury, J. B.; Sargent, E. H. Colloidal-quantum-dot photovoltaics using atomic-ligand passivation. *Nature materials* **2011**, *10*, 765–71.

[3] Ma, W.; Luther, J. M.; Zheng, H.; Wu, Y.; Alivisatos, A. P. Photovoltaic Devices Employing Ternary PbS x Se 1-x Nanocrystals 2009. *Nano letters* **2009**, 5–9.

[4] Medintz, I. L.; Uyeda, H. T.; Goldman, E. R.; Mattoussi, H. Quantum dot bioconjugates for imaging, labelling and sensing. *Nature materials* **2005**, *4*, 435–46.

[5] Moreels, I.; Fritzinger, B.; Martins, J. C.; Hens, Z. Surface chemistry of colloidal PbSe nanocrystals. *Journal of the American Chemical Society* **2008**, *130*, 15081–6.

[6] Qin, W.; Shah, R. a.; Guyot-Sionnest, P. CdSeS/ZnS alloyed nanocrystal lifetime and blinking studies under electrochemical control. *ACS nano* **2012**, *6*, 912–8.

[7] Pietryga, J. M.; Werder, D. J.; Williams, D. J.; Casson, J. L.; Schaller, R. D.; Klimov, V. I.; Hollingsworth, J. A. Utilizing the lability of lead selenide to produce heterostructured nanocrystals with bright, stable infrared emission. *Journal of the American Chemical Society* **2008**, *130*, 4879–4885.

[8] De Geyter, B.; Hens, Z. The Absorption Coefficient of PbSe/CdSe Core/shell Colloidal Quantum Dots. *Appl. Phys. Lett.* **2010**, *97*, 161908.

[9] De Geyter, B.; Justo, Y.; Moreels, I.; Lambert, K.; Smet, P. F.; Van Thourhout, D.; Houtepen, A. J.; Grodzinska, D.; de Mello Donega, C.; Meijerink, A.; Vanmaekelbergh, D.; Hens, Z. The different nature of band edge absorption and emission in colloidal PbSe/CdSe core/shell quantum dots. *ACS nano* **2011**, *5*, 58–66.

[10] Cademartiri, L.; Montanari, E.; Calestani, G.; Migliori, A.;

Guagliardi, A.; Ozin, G. a. Size-dependent extinction coefficients of PbS quantum dots. *Journal of the American Chemical Society* **2006**, *128*, 10337–46.

[11] Lambert, K.; Geyter, B. D.; Moreels, I.; Hens, Z. PbTe—CdTe Core—Shell Particles by Cation Exchange, a HR-TEM study. *Chemistry of Materials* **2009**, *21*, 778–780.

[12] Moreels, I.; Lambert, K.; Smeets, D.; De Muynck, D.; Nollet, T.; Martins, J. C.; Vanhaecke, F.; Vantomme, A.; Delerue, C.; Allan, G.; Hens, Z. Size-dependent optical properties of colloidal PbS quantum dots. *ACS nano* **2009**, *3*, 3023–30.

[13] Neeves, A.; Birnboim, M. Composite Structures for the Enhancement of Nonlinear-Optical Susceptibility. *J. Opt. Soc. Am. B* **1989**, *6*, 787–796.

[14] Suzuki, N.; Sawai, K.; Adachi, S. Optical Properties of PbSe. *J. Appl. Phys.* **1995**, *77*, 1249–1255.

[15] Ninomiya, S.; Adachi, S. Optical Properties of Cubic and Hexagonal Cdse. *J. Appl. Phys.* **1995**, *78*, 4681–4689.

[16] Porrès, L.; Holland, A.; På lsson, L.-O.; Monkman, A. P.; Kemp, C.; Beeby, A. Absolute measurements of photoluminescence quantum yields of solutions using an integrating sphere. *Journal of fluorescence* **2006**, *16*, 267–72.

Chapter VI

Langmuir films: processing

6.1 Introduction

In recent years, we have seen an increasing interest in photonic applications based on colloidal quantum dots (QDs). Using a variety of semiconductor QD materials, visible and near-infrared LEDs,[1,2] lasers,[3–5] solar cells[6] and photodetectors[7,8] have all been demonstrated. In order to fabricate these devices, the QDs must be often deposited as a thin film or a monolayer on a substrate, the choice of substrate depending on the requirements of the application. As a result, the formation of QD thin films or monolayers has become an important part of nanotechnology based on nanocrystals like QDs, also since they are of use for the study of the electronic properties of colloidal QDs by means of, for instance, scanning transmission microscopy (STM)[9] or Ultraviolet Photoemission Spectroscopy (UPS).[10]

In general, deposition of QDs is achieved by several methods, like evaporation-induced self-assembly,[11,12] drop casting,[13] template-patterning[14,15] and Langmuir-Blodgett (LB) or Langmuir-Schaeffer deposition.[9,16–19] The latter techniques have the advantage that they enable the deposition of densely packed monolayers with local ordering of QDs on almost any kind of substrate, ranging from hydrophilic mica to hydrophobic silicon.[20] LB layer formation and deposition has been studied for several metallic nanocrystals[17,18] and semiconductor QDs.[21] In addition, the technique is not restricted to the coating of flat substrates and it can be combined with optical lithography to obtain a micropatterned film.[16] Possible drawbacks that may hamper the use of

the technique concern the effect that the contact with water has on QD properties (e.g., photoluminescence) and, more in general, the lack of understanding as to why certain QDs yield excellent Langmuir films, while others fail to do so.[22,23]

In this chapter, we investigate the formation of Langmuir-Blodgett films of PbSe and PbS core QDs and of PbSe/CdSe core/shell QDs on a scale of square centimetres. We pay attention to the correlation between the surface pressure–area ($\pi - A$) isotherm and the film morphology and define the conditions to form densely packed monolayers for each of these systems. In order to assess their use in light-emitting devices, this study is complemented with an analysis of the photoluminescence of the QD monolayers after LB deposition. In the case of PbSe QDs, Langmuir-Blodgett processing leads to a complete loss of the photoluminescence. In spite of the additional CdSe shell, the same conclusion holds for PbSe/CdSe QDs. On the other hand, Langmuir-Blodgett monolayers of PbS QDs maintain their photoluminescence, even though the films slowly oxidize upon exposure to air.

6.2 Experimental

6.2.1 Synthesis of colloidal quantum dots

Monodisperse colloidal PbSe QDs were synthesized by a high-temperature synthesis developed by Murray et al.[24] as described in detail in ref. 25. The ligand shell consists of oleic acid moieties (OA), as shown by nuclear magnetic resonance spectroscopy.[26] After synthesis, the QD concentration in suspension is determined from the QD absorbance spectrum, using the molar extinction coefficient ϵ_{400} at 400 nm.[25] PbSe/CdSe core-shell QDs were synthesized starting from PbSe core QDs by means of a cation exchange reaction,[27,28] as described in detail in chapter III. Oleylamine (OLA) capped PbS QDs were synthesized using the procedure described by Cademartiri et al.[29] and described in detail in chapter II. After synthesis, the OLA ligand shell is substituted by OA. The QD concentration in suspension is again determined from the QD absorbance spectrum using ϵ_{400}.[30] In the case of PbS, transmission electron microscope (TEM) indicated the presence of a small fraction of large particles or aggregates. In that case, samples were further purified by means size-selective precip-

itation using acetonitrile as a non-solvent.

6.2.2 Fabrication of LB films

First, a known amount of QDs was dried and redispersed in 50 μL of chloroform (typical QD concentration: 4-5 μM). Then, this QD solution was gently dropped onto a LB through (Nima 312D), which was previously filled with ultra pure water. Also other liquids than water can be used, e.g. ethylene glycol or diethylene glycol. After evaporation of the chloroform the QDs cluster into 2D islands and form a submonolayer. The particles do not enter the water phase due to their hydrophobic ligand shell (e.g. oleic acid molecules). The QD layer was compressed by closing the barriers at a rate of 10 cm^2/min. The QD Langmuir film was deposited on the substrate of choice (e.g., mica or glass) by vertically pulling it out of the water at a rate of 5 mm/min (Langmuir-Blodgett) or by dipping of the substrate (Langmuir-Schaefer). The latter is a more suitable method for multilayer deposition, just by multiple dipping of the substrate.
Using a Wilhelmy plate, the process is monitored by continuous measurements of the surface pressure π:

$$\pi = \gamma^o - \gamma \tag{6.1}$$

With γ the surface tension of the water surface containing the particles and γ^o the surface tension of the pure air-water interface. As with any surfactant, formation of a monolayer causes a decrease in the surface tension, thus an increase in surface pressure. The compression of the Langmuir film can then be followed in a surface pressure π - surface area A isotherm, which contains different regimes. At large areas, the particles form isolated islands and the surface pressure remains constant at zero. Upon compression, a steep rise occurs when the islands are touching each other. When the pressure is too high, the isotherm slope decreases, indicative of layer collapse. Monolayer deposition occurs within the steep regime of the isotherm, but below the collapse pressure. A scheme of the process is shown in figure 6.1

6.2.3 Characterization

The LB monolayers were evaluated with atomic force microscopy (AFM, Molecular Imaging, PicoPlus). This technique provides

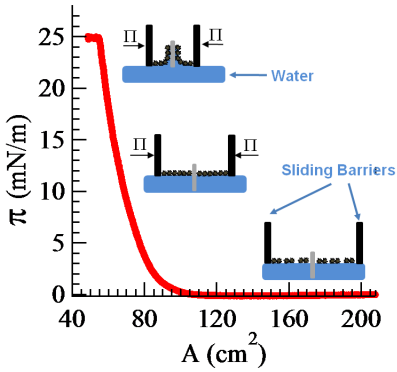

Figure 6.1: Scheme of the different steps of the Langmuir-Blodgett process along the isotherm. QDs deposition, followed by compresion by closing the barriers and finally pulling out of the substrate.

a view on the overall morphology of the monolayers (presence of micron-sized voids and cracks). On a smaller scale, the local packing of the monolayers was studied with transmission electron microscopy (TEM, Jeol, FE2200). Samples for TEM were prepared by transferring the Langmuir film to a polymer coated TEM grid by direct stamping. The absorbance of the colloidal solutions and thin films was determined by means of UV-vis-NIR spectrophotometry (Perkin Elmer Lambda 950). For measuring photoluminescence (PL) spectra, a FS920 luminescence spectrofluorometer (Edinburgh Instruments) was used. Luminescence spectra from colloidal solutions and thin films were obtained by exciting the samples at 400 nm.

6.3 Results and discussion

6.3.1 Investigation of the QD assembly kinetics

Figure 6.2 shows a typical $\pi - A$ isotherm of PbSe and PbS QDs. Clearly, both isotherms are different. In the case of PbSe QDs, the pressure does not change until a threshold area is reached, after which it rises steeply. On the other hand, PbS QDs show a more gentle rise in pressure. Around 18 mN/m we even observe a small bump in the isotherm. Hereafter, the pressure increases steeply.

In order to see if the different isotherms correspond to a differ-

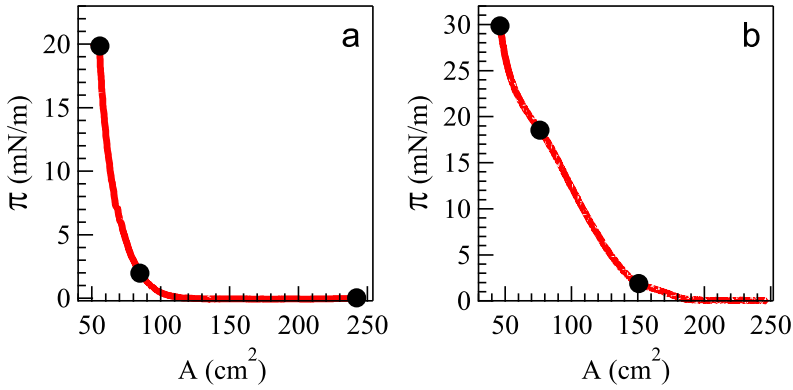

Figure 6.2: ($\pi-$A) isotherms obtained during monolayer compression of (a) PbSe QDs and (b) PbS QDs. LB depositions are carried out at the indicated pressures.

ent layer morphology, depositions were performed at the pressures marked in Figure 6.2. The profiles of the deposited QD layers were measured by means of AFM. They show two kinds of regions, with a difference in height of approximately 9.5 nm in the case of PbSe QDs (figure 6.3d) and 9 nm in the case of PbS QDs (figure 6.3d). Since these values are in fair agreement with the diameter of a single QD (6.3 and 5.7 nm, respectively), incremented by twice the OA shell thickness (1.5–2.0 nm),[26] we conclude that these images show a (sub) monolayer of QDs. The AFM topography images demonstrate that PbSe (figure 6.3) and PbS QD LB layers (figure 6.4) indeed have a different morphology. PbSe forms big islands of densely packed QDs, even at zero pressure. Clearly, the surface area can be reduced without a substantial increase in pressure until these islands touch. We observe that the islands close almost completely at pressures as low as 2 mN/m (figure 6.3b). At this point, π increases sharply while the remaining (small) holes in the layer are closed. As a result, a homogeneous close-packed monolayer is deposited at 20 mN/m (figure 6.3c). In contrast, PbS QDs initially form a sponge-like structure rather than big, densely packed islands (figure 6.4a). Closing the voids in this structure requires much larger surface pressures. At 16 mN/m, a mixture of small and larger voids is still present (figure 6.4b), and only at 30 mN/m a close-packed monolayer is deposited (figure 6.4c).

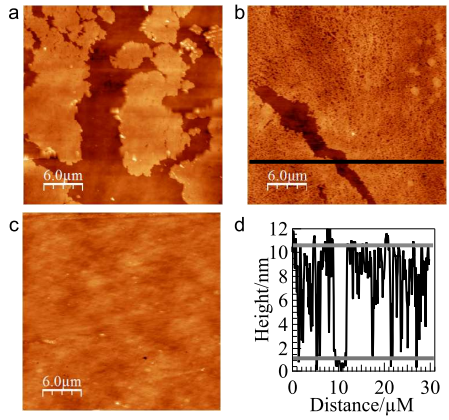

Figure 6.3: AFM images of the LB films of PbSe QDs, formed under different pressures (a) 0 mN/m, (b) 2 mN/m, (c) 20 mN/m. (d) Profile of the line shown in (b). Two levels can be distinguished, with a height difference of around 9.5 nm. The lower level corresponds to the mica substrate and the higher level is formed by PbSe QDs.

6.3.2 Investigation of the LB films on a smaller scale with TEM

Unlike the results obtained using AFM, TEM enables the investigation of local order in the LB monolayers. Figure 6.5 shows images obtained on PbSe and PbS QDs, deposited at 12 mN/m and 30 mN/m, respectively. In the case of PbSe QDs, we observe a remarkable fusion of QDs in the LB layer. While with a freshly prepared PbSe sample, the majority of the QDs still appear as individual particles (figure 6.5a), a considerable fraction of the QDs is part of a larger structure with older, more oxidized samples (figure 6.5b). Possibly, this is related to the loss of ligands upon oxidation of PbSe QDs.[26] As demonstrated by the high resolution image in figure 6.5c, fused particles show a continuation of the PbSe lattice planes over several QDs, that form in fact small quantum rods. This phenomenon closely resembles to oriented attachment of PbSe QDs to form nanowires.[31,32]

In contrast, figures 6.5d and 6.5e show that PbS QDs form a homogeneous monolayer of isolated QDs, without indication of QD fusion. The LB layer is densely packed and shows locally hexagonal ordering. Using TEM overview images, we find that the remaining voids – excluding points defects – amount to approxi-

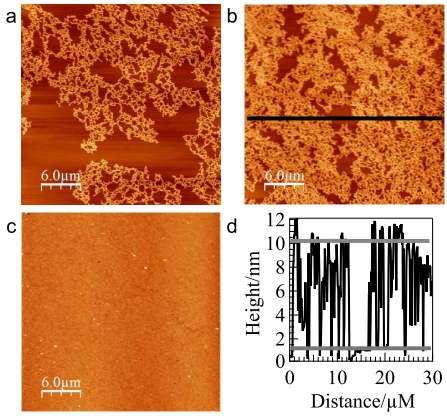

Figure 6.4: AFM images of the LB films of PbS QDs, formed under different pressures (a) 2 mN/m, (b) 16 mN/m, (c) 30 mN/m. (b) Profile of the line shown in (b). Two levels can be distinguished, with a height difference of 9 nm.

mately 2% of the layer area. We conclude that the LB technique is more suitable for the deposition of PbS QDs, where it leads to densely packed, large area monolayers of individual QDs.

6.3.3 Avoiding QD fusion – PbSe/CdSe QD monolayers

If the fusion of PbSe QDs in the Langmuir film is due to the oxidation of the QD surface, it might be prevented by the growth of a protective shell of CdSe around the PbSe QDs. After shell growth, we indeed observe (figure 6.6) that the typical blue shift of the first absorption peak upon storage of PbSe QDs under ambient conditions is strongly reduced, indicating that oxidation is strongly suppressed by the growth of a CdSe shell.

In order to form LB layers, these PbSe/CdSe QDs were suspended in chloroform and dropped on the LB trough, after which the film was compressed. The resulting $\pi - A$ isotherm is comparable to that of PbSe QDs, i.e., it remains flat down to a threshold surface area, and then rises sharply. An AFM image (figure 6.7) of a PbSe/CdSe QD LB layer, deposited on a mica substrate at a pressure of 25 mN/m, shows that the QDs yield the same flat and homogeneous layer as previously seen with PbSe and PbS. Examining the LB layer at a smaller scale using TEM, we observe that the PbSe/CdSe QDs form a densely packed monolayer with

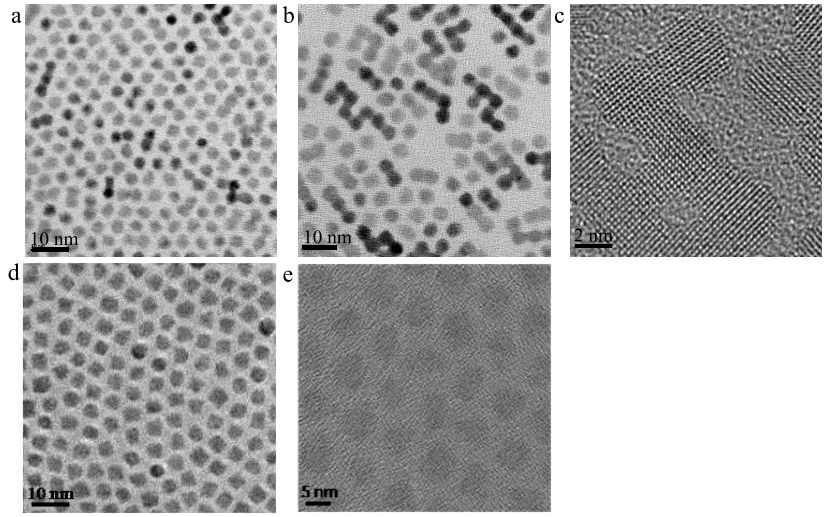

Figure 6.5: TEM images of LB depositions at different magnifications of PbSe QDs(a, b and c) and PbS QDs (d and e).

local hexagonal ordering. Excluding point defects, TEM overview images show that the voids in these layers only amount to 0.5% of the overall layer area. These results strongly contrast with the PbSe core QDs, indicating that the prevention of oxidation indeed avoids the fusion of the QDs.

6.3.4 Investigation of the optical properties of the LB films

It has been demonstrated that high quality PbS and PbSe/CdSe QD monolayers can be made by LB deposition. However, to be of use for photonic devices based on the QD luminescence, the monolayers must retain their luminescence quantum yield after deposition. To evaluate the QD photoluminescence, we compare the luminescence of the LB films to that of a colloidal solution, both normalized to their absorbance at the excitation wavelength of 400 nm. Figure 6.8 shows the resulting photoluminescence spectra of PbSe, PbSe/CdSe and PbS QDs. As could be anticipated, the luminescence of the PbSe QDs is totally quenched after deposition. Despite the improved layer morphology of PbSe/CdSe core/shell QDs, also this system loses its luminescence almost completely after LB processing. In contrast, PbS QDs maintain their

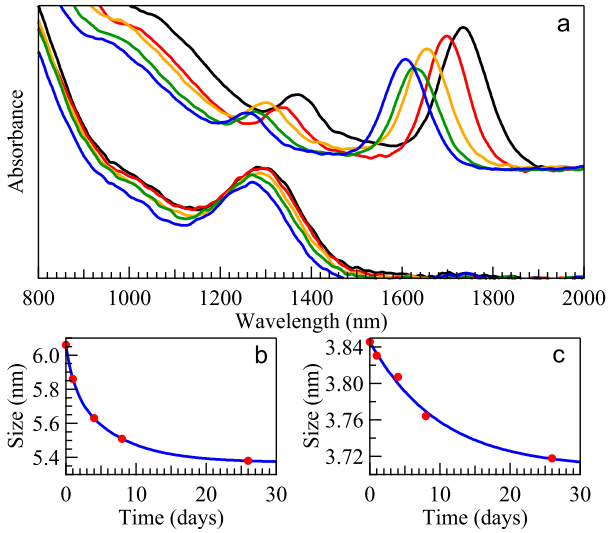

Figure 6.6: (a) Series of PbSe core (top) and PbSe/CdSe core-shell (bottom) QD absorbance spectra, taken at different times during storage under ambient conditions. We observe a strong blue shift for the core QDs, in contrast with the core-shell QDs. (b) The decrease in effective size for PbSe QDs equals 0.68 nm after 26 days. (c) The core-shell QDs show only a 0.13 nm decrease in size.

luminescence after deposition, with a reduction of the normalized quantum yield of only 14% with respect to the suspension.

Surprisingly, the PbS QD absorbance spectrum and the peak position of the luminescence show a blue shift of about 50 nm immediately after deposition. This indicates that either the LB deposition leads to the oxidation of the PbS QDs, or that the PbS monolayers are sensitive to oxidation under ambient conditions. We investigated this further by measuring the change in luminescence of PbS LB layers with time during storage in air at room temperature. Figure 6.9 shows the emission spectrum of a PbS QD suspension - kept under ambient conditions as a reference - and that of a PbS LB monolayer. While the peak wavelength of the suspension does not shift with time, the PbS LB monolayer keeps shifting and broadening after the deposition. In 1 month time, the peak wavelength has shifted by 215 and 225 nm for 3.7 and 5.2 nm PbS QDs, respectively. This corresponds to an effective diameter decrease of 0.9 nm and 1.1 nm, which is aproximately 1.5 monolayers. Surprisingly, the progressive oxidation of the PbS LB films

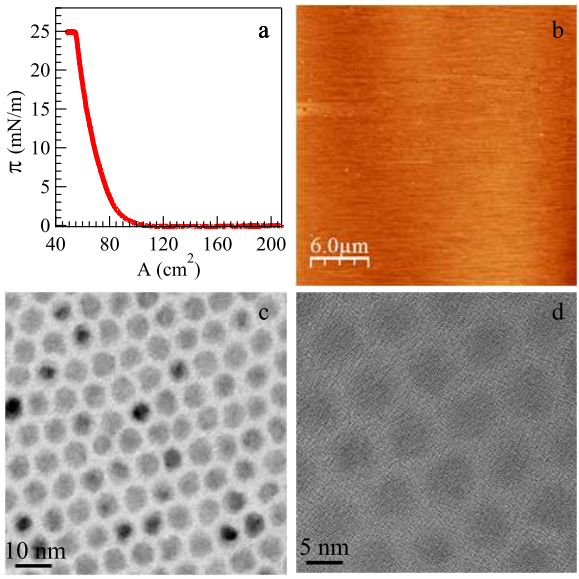

Figure 6.7: (a) ($\pi-$A) isotherm obtained during LB deposition of PbSe/CdSe QDs. (b) AFM image of PbSe/CdSe QD LB layer, deposited at 25 mN/m on mica.(c and d) TEM images of a PbSe/CdSe LB layer at different magnifications.

does not quench completely the QD luminescence. A possible explanation for this could be due to the fact that the PbS QDs were synthesized using $PbCl_2$ as reactant. Moreels et al.[33] studied the composition of the PbS QDs synthesized in this way showing that PbS QDs are nonstoichiometric. Moreover, a significant amount of Cl was also present despite the absence of unreacted $PbCl_2$. From the approximate 2:1 ratio of Cl to excess of Pb, they suggested that the excess Pb atoms most probably reside at the QD surface, with the Cl atoms bound to them. These Cl atoms could act as a protective layer that slows down the PbS QDs oxidation.

6.4 Conclusions

In this chapter, we have analyzed the formation of monolayers of PbS core, PbSe core QDs and of PbSe/CdSe core-shell QDs using Langmuir-Blodgett deposition and we have compared the photoluminescence properties of these LB films. In spite of qualitative differences in initial spreading, densely packed monolayers of both

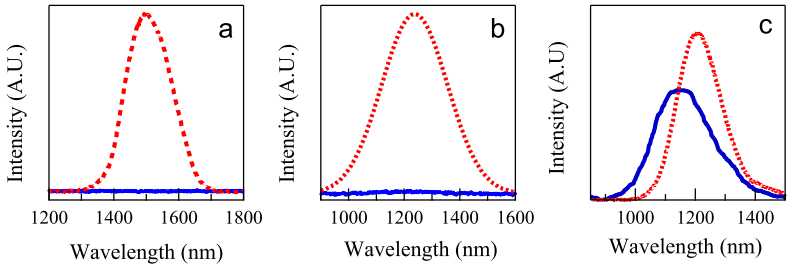

Figure 6.8: Photoluminescence of the colloidal solution (dotted line) and monolayer (full line), relative to the absorbance at 400 nm. (a) PbSe QDs, (b) PbSe/CdSe QDs, (c) PbS QDs.

PbSe and PbS QDs can be obtained. While PbS QDs exhibit good, local ordering in the LB monolayer, PbSe QDs show a fusion of particles, probably related to the oxidation of these QDs either in suspension or in the Langmuir film. This can be prevented by the growth of a CdSe shell around the PbSe core. The improved stability of the QDs leads to a well ordered hexagonally close-packed structure. In spite of the improved film quality for PbSe/CdSe and PbSe QDs, only the PbS QD LB films retain their photoluminescence after LB processing. For both PbSe and PbSe/CdSe, the LB film luminescence is almost completely quenched. Although PbS QDs films are luminescent, they undergo oxidation under ambient conditions, causing a blueshift of the photoluminescence peak. Although this oxidation leads to a final decrease in effective size of about 1 nm after one month, the films maintain their photoluminescence. These results indicate that PbS QDs are the preferred material for near-infrared light-emitting applications based on lead chalcogenide LB films.

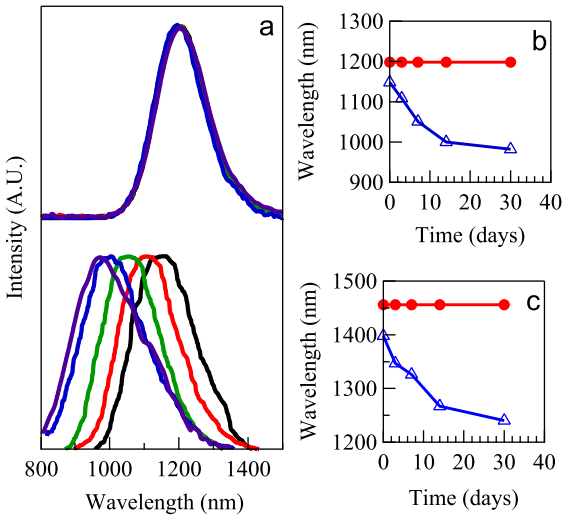

Figure 6.9: Effect of oxygen in PbS QDs. (a) Luminescence of a 3.7 nm colloidal solution (top) and monolayer (bottom) at different times. Evolution of the peak position vs time in colloidal QDs (dots) and monolayer (open triangles) in 3.7nm QDs (b) and 5.2 nm QDs (c)

Bibliography

[1] Steckel, J. S.; Snee, P.; Coe-Sullivan, S.; Zimmer, J. R.; Halpert, J. E.; Anikeeva, P.; Kim, L. A.; Bulovic, V.; Bawendi, M. G. Color-saturated green-emitting QD-LEDs. *Angewandte Chemie-international Edition* **2006**, *45*, 5796–5799.

[2] Rogach, A. L.; Gaponik, N.; Lupton, J. M.; Bertoni, C.; Gallardo, D. E.; Dunn, S.; Pira, N. L.; Paderi, M.; Repetto, P.; Romanov, S. G.; O'Dwyer, C.; Torres, C. M. S.; Eychmuller, A. Light-emitting diodes with semiconductor nanocrystals. *Angewandte Chemie-international Edition* **2008**, *47*, 6538–6549.

[3] Malko, a. V.; Mikhailovsky, a. a.; Petruska, M. a.; Hollingsworth, J. a.; Htoon, H.; Bawendi, M. G.; Klimov, V. I. From amplified spontaneous emission to microring lasing using nanocrystal quantum dot solids. *Applied Physics Letters* **2002**, *81*, 1303.

[4] Schaller, R. D.; Petruska, M. A.; Klimov, V. I. Tunable near-infrared optical gain and amplified spontaneous emission using PbSe nanocrystals. *Journal of Physical Chemistry B* **2003**, *107*, 13765–13768.

[5] Klimov, V. I.; Ivanov, S. a.; Nanda, J.; Achermann, M.; Bezel, I.; McGuire, J. a.; Piryatinski, A. Single-exciton optical gain in semiconductor nanocrystals. *Nature* **2007**, *447*, 441–6.

[6] Sargent, E. H. Infrared photovoltaics made by solution processing. *Nature Photonics* **2009**, *3*, 325–331.

[7] McDonald, S. a.; Konstantatos, G.; Zhang, S.; Cyr, P. W.; Klem, E. J. D.; Levina, L.; Sargent, E. H. Solution-processed PbS quantum dot infrared photodetectors and photovoltaics. *Nature materials* **2005**, *4*, 138–42.

[8] Rauch, T.; Boberl, M.; Tedde, S. F.; Furst, J.; Kovalenko, M. V.; Hesser, G. N.; Lemmer, U.; Heiss, W.; Hayden, O. Near-infrared imaging with quantum-dot-sensitized organic photodiodes. *Nature Photonics* **2009**, *3*, 332–336.

[9] Lambert, K.; Wittebrood, L.; Moreels, I.; Deresmes, D.; Grandidier, B.; Hens, Z. Langmuir-Blodgett monolayers of InP quantum dots with short chain ligands. *Journal of colloid and interface science* **2006**, *300*, 597–602.

[10] Tanaka, A.; Imamura, M.; Yasuda, H. Interface electronic structure of alkanethiolate-passivated Au nanoparticles studied by photoelectron spectroscopy. *Physical Review B* **2006**, *74*, 113402.

[11] Shevchenko, E. V.; Talapin, D. V.; Murray, C. B.; O'Brien, S. Structural characterization of self-assembled multifunctional binary nanoparticle superlattices. *Journal of the American Chemical Society* **2006**, *128*, 3620–3637.

[12] Brezesinski, T.; Groenewolt, M.; Gibaud, a.; Pinna, N.; Antonietti, M.; Smarsly, B. Evaporation-Induced Self-Assembly (EISA) at Its Limit: Ultrathin, Crystalline Patterns by Templating of Micellar Monolayers. *Advanced Materials* **2006**, *18*, 2260–2263.

[13] Norsten, T. B.; Frankamp, B. L.; Rotello, V. M. Metal Directed Assembly of Terpyridine-Functionalized Gold Nanoparticles. *Nano Letters* **2002**, *2*, 1345–1348.

[14] Shenton, W.; Pum, D.; Sleytr, U. B.; Mann, S. Synthesis of cadmium sulphide superlattices using self-assembled bacterial S-layers. *Nature* **1997**, *389*, 585–587.

[15] Hoogenboom, J. P.; Retif, C.; de Bres, E.; de Boer, M. V.; van Langen-Suurling, A. K.; Romijn, J.; van Blaaderen, A. Template-induced growth of close-packed and non-close-packed colloidal crystals during solvent evaporation. *Nano Letters* **2004**, *4*, 205–208.

[16] Lambert, K.; Moreels, I.; Thourhout, D. V.; Hens, Z. Quantum dot micropatterning on si. *Langmuir : the ACS journal of surfaces and colloids* **2008**, *24*, 5961–6.

[17] Zhou, H. P.; Zhang, C.; Yan, C. H. Controllable Assembly of Diverse Rare-Earth Nanocrystals via the Langmuir-Blodgett Technique and the Underlying Size- and Symmetry-Dependent Assembly Kinetics. *Langmuir* **2009**, *25*, 12914–12925.

[18] Khomutov, G. B. Interfacially formed organized planar inorganic, polymeric and composite nanostructures. *Advances in colloid and interface science* **2004**, *111*, 79–116.

[19] Lambert, K.; Capek, R. K.; Bodnarchuk, M. I.; Kovalenko, M. V.; Thourhout, D. V.; Heiss, W.; Hens, Z. Langmuir-Schaefer Deposition of Quantum Dot Multilayers. *Langmuir* **2010**, *26*, 7732–7736.

[20] Dabbousi, B. O.; Murray, C. B.; Rubner, M. F.; Bawendi, M. G. Langmuir-blodgett Manipulation of Size-selected Cdse Nanocrystallites. *Chemistry of Materials* **1994**, *6*, 216–219.

[21] Tao, A. R.; Huang, J. X.; Yang, P. D. Langmuir-Blodgettry of Nanocrystals and Nanowires. *Accounts of Chemical Research* **2008**, *41*, 1662–1673.

[22] Lee, Y.-L.; Du, Z.-C.; Lin, W.-X.; Yang, Y.-M. Monolayer behavior of silica particles at air/water interface: a comparison between chemical and physical modifications of surface. *Journal of colloid and interface science* **2006**, *296*, 233–41.

[23] Santhanam, V.; Liu, J.; Agarwal, R.; Andres, R. P. Self-assembly of uniform monolayer arrays of nanoparticles. *Langmuir* **2003**, *19*, 7881–7887.

[24] Murray, C. B.; Sun, S. H.; Gaschler, W.; Doyle, H.; Betley, T. A.; Kagan, C. R. Colloidal synthesis of nanocrystals and nanocrystal superlattices. *Ibm Journal of Research and Development* **2001**, *45*, 47–56.

[25] Moreels, I.; Lambert, K.; De Muynck, D.; Vanhaecke, F.; Poelman, D.; Martins, J. C.; Allan, G.; Hens, Z. Composition and Size-Dependent Extinction Coefficient of Colloidal PbSe Quantum Dots. *Chemistry of Materials* **2007**, *19*, 6101–6106.

[26] Moreels, I.; Fritzinger, B.; Martins, J. C.; Hens, Z. Surface chemistry of colloidal PbSe nanocrystals. *Journal of the American Chemical Society* **2008**, *130*, 15081–6.

[27] Pietryga, J. M.; Werder, D. J.; Williams, D. J.; Casson, J. L.; Schaller, R. D.; Klimov, V. I.; Hollingsworth, J. A. Utilizing the lability of lead selenide to produce heterostructured nanocrystals with bright, stable infrared emission. *Journal of the American Chemical Society* **2008**, *130*, 4879–4885.

[28] Lambert, K.; De Geyter, B.; Moreels, I.; Hens, Z. PbTe/CdTe Corel/Shell Particles by Cation Exchange, a HR-TEM study. *Chemistry of Materials* **2009**, *21*, 778–780.

[29] Cademartiri, L.; Montanari, E.; Calestani, G.; Migliori, A.; Guagliardi, A.; Ozin, G. a. Size-dependent extinction coefficients of PbS quantum dots. *Journal of the American Chemical Society* **2006**, *128*, 10337–46.

[30] Moreels, I.; Lambert, K.; Smeets, D.; De Muynck, D.; Nollet, T.; Martins, J. C.; Vanhaecke, F.; Vantomme, A.;

Delerue, C.; Allan, G.; Hens, Z. Size-dependent optical properties of colloidal PbS quantum dots. *ACS nano* **2009**, *3*, 3023–30.

[31] Cho, K.-S.; Talapin, D. V.; Gaschler, W.; Murray, C. B. Designing PbSe nanowires and nanorings through oriented attachment of nanoparticles. *Journal of the American Chemical Society* **2005**, *127*, 7140–7.

[32] Koh, W. K.; Bartnik, A. C.; Wise, F. W.; Murray, C. B. Synthesis of Monodisperse PbSe Nanorods: A Case for Oriented Attachment. *Journal of the American Chemical Society* **2010**, *132*, 3909–3913.

[33] Moreels, I.; Lambert, K.; Smeets, D.; De Muynck, D.; Nollet, T.; Martins, J. C.; Vanhaecke, F.; Vantomme, A.; Delerue, C.; Allan, G.; Hens, Z. Size-Dependent Optical Properties of Colloidal PbS Quantum Dots. *ACS Nano* **2009**, *3*, 3023–3030.

Chapter VII

Langmuir films: mechanism of formation and properties

7.1 Introduction

Langmuir-Blodgett (LB) or Langmuir-Schaefer (LS) deposition is a nanocrystal (NC) deposition technique in which a NC Langmuir film is transferred either vertically (LB) or horizontally (LS) to a substrate. Important advantages are that well-defined, large area NC monolayers with a tunable particle density can be obtained and that the deposition is not limited to flat substrates. Especially for colloidal quantum dots (QDs), this is a highly attractive processing method since applications such as LEDs,[1] photodetectors,[2] biosensors[3] and light-harvesting devices[4] require high-quality QD mono- or multilayers. In this chapter, we show how the formation of high quality Langmuir films enabled us to study the formation of different quantum dots mono and multilayers, and use them for analyzing the properties of quantum dots in close packed films.

In the first part, it is shown that the continued compression of monolayers of a variety of colloidal QDs leads to a sequence of plateaus in the $\pi - A$ isotherm. Using Transmission Electron Microscopy (TEM) and Atomic Force Microscopy (AFM), we find that these plateaus correspond to the consecutive formation of a QD double and triple layer. Moreover, we argue that these transformations correspond to phase transitions in the Langmuir film that can be rationalized based on thermodynamic considerations. This work has been initiated by dr. K. Lambert and finalized in

the course of this PhD research.
The second part compares the absorbance cross section of PbS and CdSe QDs in colloidal solutions and in close packed monolayers.[5,6] As compared to literature data on the cross section in diluted dispersions ($\sigma_{0,s}$) of both materials, we find that σ_f can be enhanced up to a factor of 4 (CdSe) or 5 (PbS). Especially in the case of PbS QDs, the enhancement $\mathcal{E} = \sigma_f/\sigma_{0,s}$ shows a marked, resonance-like diameter dependence, with a maximum value for QDs of around 4 nm. This work was possible thanks to a close collaboration with Pieter Geiregat, who performed the modeling needed to understand the absorption enhancement.
Finally we have investigated layers of PbSe/CdSe core/shell NCs by means of scanning tunneling spectroscopy (STS) at low temperatures. Here, we show that the potential drop across both potential barriers is rather symmetric when we study PbSe/CdSe core-shell NCs with an intended shell thickness of 0.4 nm. As a result, for the majority of the NCs we find that the peaks observed in the tunneling spectra at both negative and positive voltages are related to the same charge carriers, corresponding to a unipolar transport regime. As the nature of the charge carriers contributing to the tunneling current varies from NC to NC, the shell structure of the PbSe/CdSe core-shell NCs has also been investigated by photoemission spectroscopy. It reveals the existence of a partial shell, which accounts for the fluctuations of the potential drop measured across the tunnel barriers, depending on the orientations that the NCs have adopted on the substrate. This work has been performed in close collaboration with T. H. Nguyen and B. Grandidier from the IEMN in Lille, France.

7.2 Experimental

Synthesis

CdSe synthesis. Q-CdSe particles are synthesized following Jasieniak et al.[7] Cadmium oxide (CdO, 0.36 mmol, 99.99 %, Strem), oleic acid (OA, 3.6 mmol, 90 %, Aldrich) and n-octadecene (ODE, 12 mL, 90 % Alfa Aesar) are mixed and degassed for 1 h at 100 ℃ under nitrogen, followed by heating to 265 ℃ until all CdO dissolves. A room-temperature selenium stock solution (16 mL, 0.1 M in ODE) is injected. The reaction continues at 235 ℃ for 16 min. Equal volumes of toluene and isopropanol are added to

the crude synthesis mixture, which is then washed four times by precipitating with methanol, and redispersion in toluene.

PbS synthesis. Oleylamine (OLA) capped PbS QDs were synthesized using the procedure described by Cademartiri et al.[8] and modified by Moreels et al.[9] After synthesis, the OLA ligand shell is substituted by OA. An exchange to OA is typically performed by adding OA to a toluene suspension of PbS QDs in a ratio of 1.5:10 OA/toluene. After precipitation with EtOH and centrifugation, the Qdots are resuspended in toluene and the exchange is repeated.

PbSe synthesis Monodisperse colloidal PbSe QDs were synthesized by a high-temperature synthesis developed by Murray et al.[10] and described previously in this thesis.

PbSe/CdSe cation exchange PbSe/CdSe core-shell QDs were synthesized starting from PbSe core QDs by means of a cation exchange reaction.[11] In this reaction, Cd-oleate (0.3M stock solution) is added to a PbSe QD suspension in toluene at 100°C (the typical Pb:Cd ratio used is 1:10). After 40 minutes, the reaction is quenched using a mixture of MeOH and BuOH (1:2) and precipitated twice.

Langmuir depositions

Quantum dot Langmuir films are made using a Nima 312D trough. Typically, 20-50 μL of a QD suspension is spread drop wise on the water surface (250 cm^2), resulting in a submonolayer which is then compressed at a rate of 10 $cm^2 min^{-1}$. The layers are transferred on glass or silicon substrates by LS or LB (5 $mm.min^{-1}$) deposition.

Absorbance measurements

The absorption and reflection of the monolayers is measured using a commercial spectrophotometer (Perkin-Elmer Lambda 950 UV-VIS-NIR) equipped with an absolute reflectance measurement (URA) tool.

Microscopy analysis

TEM samples are made by LS deposition on a carbon-coated copper grid and studied with a Jeol 2200 FS microscope. AFM analysis is done with a Molecular Imaging PicoPlus system in AC AFM mode.

7.3 Phase transitions in quantum-dot Langmuir films

7.3.1 Experimental observations

A typical $\pi - A$ isotherm of 4.0 nm CdSe QDs (Q-CdSe), standard deviation (σ) 6.9% on the air/water interface shows different regions (figure 7.1). Regions I and II represent the usual transition from monolayer islands into a full monolayer (see chapter VI). Around 17 mN/m the slope of the isotherm decreases, indicating layer collapse (i.e., transfer of particles out of the monolayer). However, further compression only leads to a minor pressure increase, creating a plateau in the isotherm (III). When the surface area of the trough is reduced to half the area of the initial full monolayer (A_1), a second increase of the surface pressure is observed (IV), followed by another plateau (V) and again a pressure increase (VI) starting at about $A_1/3$. Q-CdSe Langmuir films in the steep parts of the isotherm (II, IV, VI) were transferred to silicon substrates using LB deposition. Analysis of such samples reveals microscopic cracks in the multilayer films which are convenient for film thickness determination using AFM. Height profiles show a stepwise increase in layer thickness going from region II to IV and VI, indicative of a transition from a monolayer to a bi- and a trilayer. The multilayer roughness is higher than that of the monolayers. It corresponds to monolayer-thick terraces on top of the multilayer, forming longitudinal domains perpendicular to the direction of compression. The cracks are avoided using LS deposition instead of LB, meaning that they are due to the vertical transfer and are not present at the air/water interface. In contrast with CdSe monolayers,[6] CdSe multilayers do not dewet upon LS deposition on hydrophilic substrates. Therefore, LS is favorable over LB deposition of the multilayers.

TEM images of CdSe monolayers show a close-packed layer with local hexagonal order (figure 7.2a, right). Layers deposited

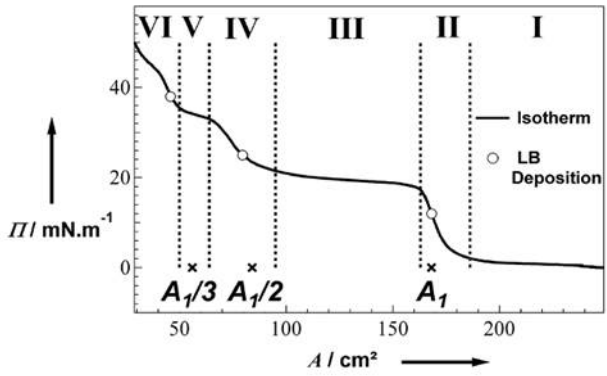

Figure 7.1: Pressure-area isotherm of a Q-CdSe suspension spread on a water surface, showing different regimes.

at 25 mNm^{-1}, i.e, the second steep rise of the isotherm show a bilayer, with a more disordered particle stacking (figure 7.2b). Compression to 38 mNm^{-1} leads to trilayers with complex structures (figure 7.2c). Within the plateau regions, lower resolution TEM images show that the Langmuir films consist of a variety of isolated double (figure 7.3a) or triple (figure 7.3b) layer regions in the first and second isotherm plateau, respectively. These regions can contain a few QDs only or can extend over several hundreds of nanometers. This strongly indicates that an additional monolayer is formed by locally lifting QDs from the Langmuir film and that these on-top QDs have sufficient mobility to assemble in monolayer islands. Although the overall transition from an n to an $n+1$ layer film ($n \rightarrow n+1$ transition) is not reversible – upon releasing the surface pressure, multilayers do not form monolayers again – these observations indicate that the succession of n→n+1 transitions of the QD Langmuir film can be understood using thermodynamic arguments.

7.3.2 Interpretation using a thermodynamic model

When a QD is transferred from a monolayer to a double layer, the free energy change involves the loss of lateral QD-QD interactions within the monolayer and the vertical interactions between the QD and the water surface underneath (binding energy u_1), while one gains lateral QD-QD interactions in the second QD layer together with the total vertical interaction energy of a QD in the second

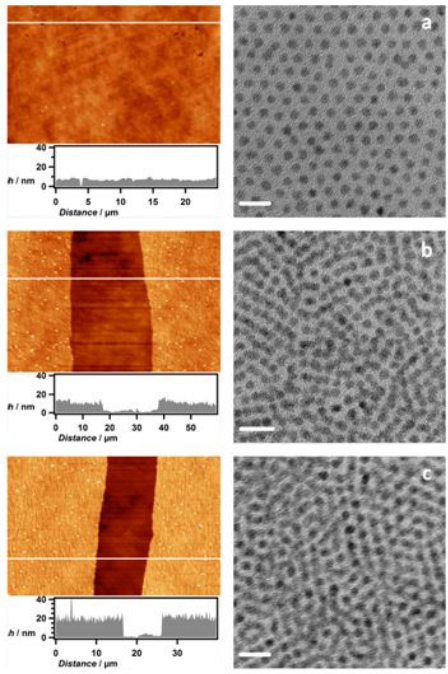

Figure 7.2: (a-c) AFM images, corresponding height (h) profiles and TEM images of Langmuir-Blodgett (a) monolayer, (b) bilayers and (c) trilayers. The TEM scale bar corresponds to 10 nm.

layer (binding energy u_2). For the 1→2 transition, one can show that the change in lateral QD-QD interaction is a minor contribution, meaning that the pressure at which the phase transition occurs is largely given by equation 7.1

$$\pi_{1\to 2} = \frac{u_2 - u_1}{a_0} \tag{7.1}$$

Here, a_0 is the surface area of a single QD in the monolayer. Equation 7.1 yields a positive surface pressure when $u_1 < u_2$. Since these are negative numbers (it requires energy to break the interactions), this implies that u_1 must be more negative than u_2, hence the 'vertical' interactions must be stronger for a QD in the first layer than for a QD in the second layer. The fact that the QDs initially spread on the water surface in monolayer islands shows that this is indeed the case.

If equation 7.1 provides an interpretation for the collapse of a QD monolayer, it remains to be demonstrated under what condi-

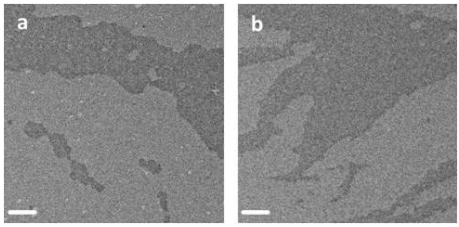

Figure 7.3: TEM images of Q-CdSe Langmuir films transferred in (a) the first isotherm plateau and (b) the second isotherm plateau. The scale bare corresponds to 150 nm.

tions this results in the formation of a double layer. Defining u_3 as the vertical interaction of particles in a trilayer (i.e., with the underlying QD layers and the water surface), an expression similar to equation 7.1 can be derived for the bilayer-trilayer transition. Since this involves the gain of 2 times u_3 at the expense of u_1 and u_2, we have:

$$\pi_{2\to3} = 2\frac{u_3 - u_2}{a_0} + \frac{u_2 - u_1}{a_0} = 2\frac{u_3 - u_2}{a_0} + \pi_{1\to2} \tag{7.2}$$

We see that $\pi_{2\to3}$, that is the pressure where a triple layer is formed, will differ from $\pi_{1\to2}$ if the u_3 interaction is weaker than the u_2 interaction. Hence, the successive formation of multiple QD layers by compressing a QD Langmuir film requires a gradient in the vertical interactions. The fact that the successive pressure steps are progressively smaller indicates that this gradient disappears with increasing layer number. Hence, we can infer that the energy difference $u_{\mathrm{n}+1} - u_{\mathrm{n}}$ tends to zero with increasing n, which limits the number of successive $n \to n+1$ transitions.

7.3.3 Conclusions

In summary, we demonstrate that the compression of QD Langmuir layers beyond their documented collapse pressure results in a successive set of phase transition into bi- and trilayers. These transitions are seen as plateaus in the isotherms. Their occurrence can be rationalized using thermodynamic considerations, which link the pressure required for a phase transition to the difference in vertical interaction energy. From a practical perspective, the occurrence of phase transformations in Langmuir films enable a

more efficient use of the LS technique, as the results clearly show that large-scale, high-quality QD multilayers can be transferred to a substrate of choice using a single deposition step.

7.4 Absorption enhancement in colloidal quantum dots Langmuir films

7.4.1 Experimental observations

This work makes use of monodisperse batches of CdSe and PbS QDs stabilized by oleate ligands. They have been synthesized with diameters d_{QD} ranging from 2.5 to 5 nm for CdSe and 2.5 to 8 nm for PbS. In both cases, QD monolayers are formed by spreading a QD dispersion on a Langmuir through, followed by the transfer of the Langmuir film to a glass substrate using Langmuir-Blodgett deposition. As shown in figure 7.4, this results in homogeneous monolayers over cm^2 areas, with typical surface coverages as determined by atomic force microscopy (AFM) of 95% or more. In addition, transmission electron microscopy (TEM) demonstrates that the monolayers have a locally hexagonal ordering. The QD surface density (N_s) is determined from TEM micrographs (figure 7.4(c)), while the QD interdistance – written as $d_{QD} + 2l$ where l denotes the thickness of the ligand shell – is obtained from more detailed TEM analysis (see figure 7.4(d)). In our case oleic acid is used, an 18 carbon fatty acid. The length of the chain is around 2.1 nm. However, during monolayer compression in the LB technique, the nanocrystals get pressed together resulting an intermixing of adjacent ligands. This results in increased packing, i.e. more particles per unit surface area.

Using the TEM images (see figure 7.5), we can obtain the real superlattice spacing by taking a simple spatial FFT (Fast Fourier Transform) (software: ImageJ 1.44). The reciprocal lattice of a simple hexagonal lattice is again hexagonal. From the reciprocal lattice parameters, the real lattice parameters can be easily evaluated. We confirm this by taking statistical (average over 10 measurements) averages of the spacing in the real lattice. This analysis amounts to an average ligand length of 1.50 nm in the layer, much smaller than the 2.1 nm of the 'free' oleic acid molecule.

The absorption cross section σ_f of a QD in these close packed monolayers is calculated from the absorbance A and the reflectance R:

$$\sigma_f = \ln 10 \times \frac{A - R}{N_s} \tag{7.3}$$

In this expression, scattering is neglected since the wavelengths used (> 350 nm) are much larger than the quantum dot diameter.

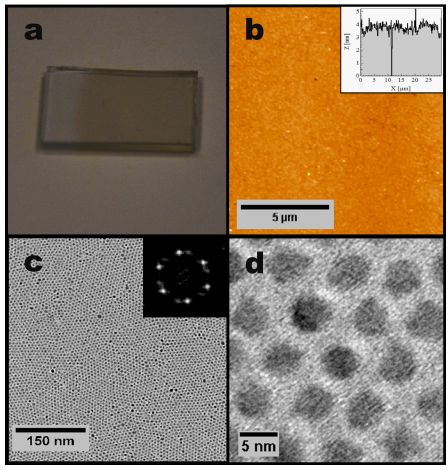

Figure 7.4: Langmuir-Blodgett monolayer of PbS quantum dots. (a) Contrast picture of a monolayer of PbS quantum dots ($d = 5\,\mathrm{nm}$) on a glass surface ($2\,\mathrm{cm} \times 1\,\mathrm{cm}$) showing homogeneous cm^2 coverage. (b) Atomic force microscope scan of the same PbS monolayer indicating excellent area uniformity (inset: cross section). (c) Larger area TEM image showing the PbS quantum dot superlattice with local hexagonal ordering (inset: Fourier transform image). (d) zoomed-in TEM image showing the individual quantum dots and their interdistance.

The absorbance in a regular spectrophotometer always includes contributions of reflection. Especially for thin layers, these corrections can be quite substantial. Therefore, we collect absolute reflectance data (collection angle of incidence = 8°) for all our samples (see figure 7.6). The corrections are quite small however, typically <10% of the measured absorbance is due to net reflectance of the nanocrystal monolayer. The absorption is set to zero beyond the band gap (i.e., $A_{2000} = 0$) to correct for any background absorption. To calculate the absorption enhancement, we combine the experimental values of σ_f with published values for $\sigma_{0,s}$, where we work at 400 nm for PbS and at 335 nm for CdSe.

Figure 7.7a and b shows the absorption enhancement $\mathcal{E}$ for PbS and CdSe QDs as a function of their diameter at 400 and 335 nm, respectively. For PbS, we find that $\mathcal{E}$ initially increases with increasing particle size up to a maximum of 5 at a core size of around 4 nm. For larger sizes, $\mathcal{E}$ goes down and reaches values of about 1 for 8 nm particles. In the case of CdSe, $\mathcal{E}$ steadily increases within the diameter range studied to level off at a value of around

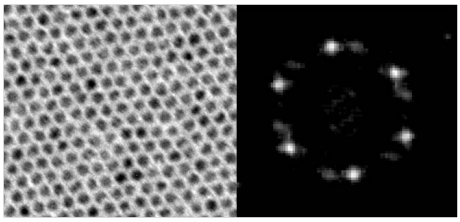

Figure 7.5: Packing density from (left) real space lattice and (right) typical Fourier image of a simple hexagonal lattice used to determine the interparticle spacing.

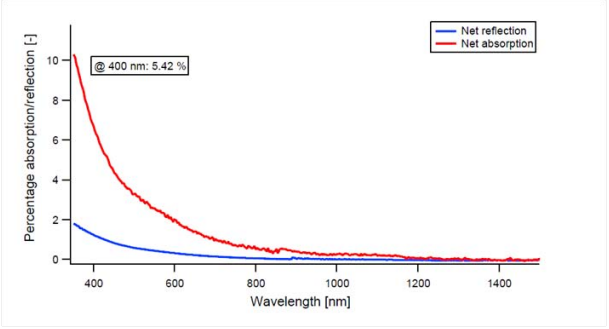

Figure 7.6: Absorbance and reflectance measured for a 4.3 nm PbS monolayer on glass. The inset gives the percentage of the 'measured absorbance' (red line) that is actually reflectance (blue line).

4 for a diameter of 6.2 nm. We also investigated the influence of the thickness of the ligand shell l. In particular, for a fixed size of CdSe nanocrystal (4.4 nm), the ligand shell was exchanged from oleic acid to shorter chain carboxylic acids (palmitic, myristic and dodecanoic acid). The enhancement as function the ligand length (determined from TEM analysis) is shown in figure 7.7c. We notice a steep decrease in $\mathcal{E}$ for increasing ligand length (or equivalently "interparticle spacing").

7.4.2 Interpretation using the coupled dipole model

Colloidal nanocrystals properties (e.g. absorption cross sections, exciton lifetime, etc.) are typically evaluated in solution using effective medium approaches such as the Maxwell-Garnett model. These models assume that the individual nanocrystals behave as uncoupled dipoles embedded in a host medium with given permit-

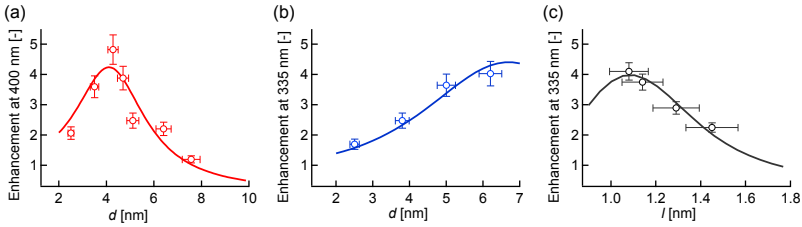

Figure 7.7: Absorption enhancement $\mathcal{E}$ for (a) PbS quantum dots at 400 nm and (b) CdSe quantum dots at 335 nm as a function of QD diameter. The markers indicate experimental values, while the solid lines represents the enhancement predicted by the coupled dipole model. The horizontal error bars are based on the particle size dispersion, which is typically 5–10%.

tivity. However, it is clear that this assumption no longer holds for a close packed film of QDs where the dipoles can couple through electromagnetic multipolar interactions. Using properties measured in solution to evaluate the performance and physics of thin film devices is therefore incorrect, or at least a serious simplification.

We proposed to treat the coupling of QDs in thin films using the 'coupled dipole model'. This model was developed to understand the localised plasmonic response of coupled arrays of metallic nanoparticles. Its basic idea is that the internal field of a particle in close proximity to other dipoles will be a superposition of the external field and the induced dipolar fields of the neighboring particles. We apply this theory to hexagonally close packed monolayers of QDs. To compare light absorption by particles in a close packed monolayer with that of particles dispersed in a dielectric, we define an 'enhancement factor' $\mathcal{E}$, being the ratio between the absorption cross section in film to that in solution. We consider QDs of PbS and CdSe, both passivated with oleic acid, as model systems since these show a bulk like dielectric function at energies well above the first exciton transition. In this way, we calculate $\mathcal{E}$ in close packed monolayers as a function of particle size within the CD model. The only free parameter in this procedure is the dielectric constant of the film environment which we chose to be 3.5, resembling an environment of air, glass and other nanoparticles.

7.4.3 Conclusions

In summary, we have demonstrated strong optical coupling phenomena in close packed monolayers of colloidal QDs, leading to giant enhancement of the absorbance per QD up to a factor of 5. On top of the cheap bottom-up fabrication and processing, a collective property like absorption enhancement makes colloidal QDs extremely suited for applications in photovoltaics and photodetection, where a trade-off between layer thickness and light absorption restricts conversion efficiencies.

7.5 Charge carrier identification in tunneling spectroscopy of core/shell colloidal quantum dots Langmuir films

7.5.1 Theoretical background

When a QD on a conductive substrate is approached with the tip of a scanning tunneling microscope, a double barrier tunnel junction (DBTJ) is formed. Under specific conditions, the differential conductivity (dI/dV) of this junction yields a sequence of peaks as a function of the tip-to-substrate voltage, which correspond to the onset of tunneling in successive QD energy levels.[12,13] However, the interpretation of such a scanning tunneling spectrum strongly depends on the potential distribution in the DBTJ. This is typically characterized by the lever arm η, a quantity corresponding to the ratio between the potential drop across the NC-tip junction and the voltage applied to the gold surface with respect to the tip held at virtual ground. Based on the capacitance model shown in figure 7.8a where the core-shell NC exhibits the properties of a type-I heterostructure, the lever arm is given by the ratio between the capacitance C_1 and the sum of the capacitance C_1 and C_2:

$$\eta = C_1/(C_1 + C_2) \tag{7.4}$$

When the tip is far from the NC, C_2 is usually much smaller than C_1 and the lever arm is close to 1. In this case the transmission probability across the second potential barrier is much smaller than the transmission probability across the first potential barrier (see figure 7.8b), and the measurements of peaks in the tunneling spectra correspond to single-electron energy levels. In such a regime, usually named the shell-tunneling regime, the lowest peaks observed on both sides of the apparent band gap, also called the zero-conductance region, are related to the electron (positive bias) and hole (negative bias) ground states, respectively.[12]

An alternative tunneling regime may occur when C_2 becomes comparable to C_1, which means that the lever arm approaches 0.5. In the simplified model of figure 7.8, this can arise when the thickness of both tunnel barriers are similar. Then, the transmission probability across the barriers becomes comparable (figure 7.8c), a situation favorable for charging the NC. However, the same situation $\eta \approx 0.5$ also favors bipolar transport, i.e., hole tunneling at positive bias and/or electron tunneling at negative bias.

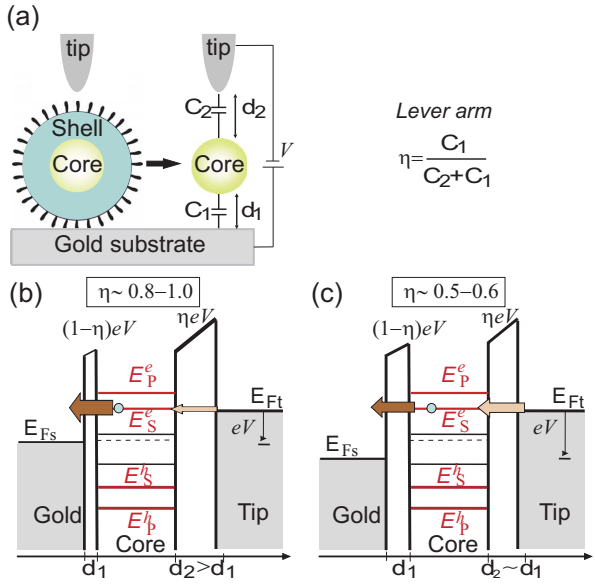

Figure 7.8: (a) Schematic and equivalent circuit of a double barrier tunnel junction, where a core-shell NC is inserted between a STM tip and a gold substrate. The lever arm, the applied voltage, the capacitance, and the thickness of both barriers are labeled η, V, C_1, C_2, d_1, and d_2, respectively. (b), (c) Energy-band diagrams of the system when η is high or low. The electron/hole S and P energy levels of the core, the Fermi levels of the tip E_{Ft}, substrate E_{Fs}, and NC (dashed segment) are indicated, as well as the magnitude of the transmission probability across both barriers (arrows with different widths).

Here, we use scanning tunneling spectroscopy (STS) in an attempt to identify the electronic energy levels in PbSe/CdSe core/shell QDs. Since STS on single, isolated QDs is often hampered by the (mechanical) instability of tip-dot-substrate DBTJ, we use QDs embedded in a close packed monolayer made by Langmuir-Blodgett deposition.

7.5.2 Experimantal results and discussion

PbSe/CdSe core/shell with a mean diameter of 7.9 nm and a 0.4 nm shell where analyzed by means of scanning tunneling spectroscopy. The NCs were deposited on flame-annealed Au(111) substrates and loaded in an ultra high vacuum (UHV) system. In

a typical STS experiment, the size of the QD probed is first estimated by imaging the dot and its neighbors by STM. Next, a series of tunneling spectra with increasing tunneling current setpoints is recorded to analyze to dependence of the spectrum on the lever arm.

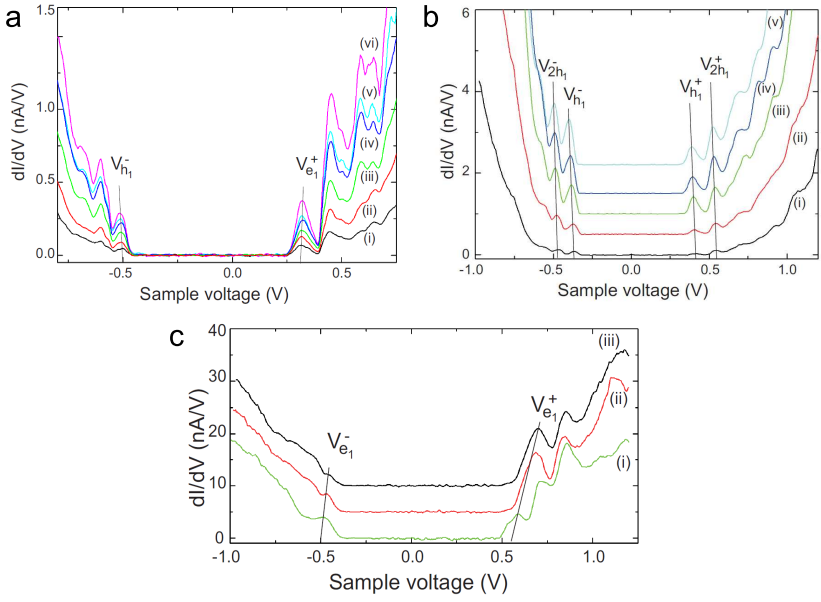

Figure 7.9: Set of differential conductance spectra measured on a PbSe/CdSe NC with a diameter of 8.5 nm. a) The feedback parameters were V_S =+1.2 V and I_{set} = 0.5 nA (i), 1.0 nA (ii), 1.5 nA (iii), 2.0 nA (iv), 2.5 nA (v), and 3.0 nA (vi). The peaks labeled V_{h1}^-, V_{e1}^+ correspond to the tunneling of holes and electrons through the hole and electron ground states, respectively. The oblique segments are used as guides to the eye to highlight the shift of the peak positions with increasing I_{set}. b) The feedback parameters were V_S = +1.2 V and I_{set} = 0.5 nA (i), 1.0 nA (ii), 2.0 nA (iii), 2.5 nA (iv), and 3.0 nA (v). The peaks labeled V_{h1}^-, V_{2h1}^-, V_{h1}^+, V_{2h1}^+ correspond to tunneling through the hole ground state with zero and one hole at negative and positive bias. The oblique segments are used as guides to the eye to highlight the shift of the peak positions with increasing I_{set}. c) The feedback parameters were V_S = +1.2 V and I_{set} = 1 nA (i), 2.5 nA (ii), and 2.8 nA (iii). The peaks labeled V_{e1}^-, V_{e1}^+ correspond to the tunneling of electron from the electron ground state at negative and positive bias. The oblique segments are used as guides to the eye to highlight the shift of the peak position with increasing I_{set}.

Figure 7.9a-c shows three typical examples of STS spectra recorded on different QDs. They all feature a rather symmetric spectrum with a zero conductance gap that markedly increases the QD bandgap (estimated at $\approx 0.55 - 0.6$ eV), yet the spectra change differently when the lever arm is decreased. In figure 7.9a, the conductance peak at positive and negative bias shown an opposite shift, in the direction of more positive and more negative potential differences, respectively. Opposite from this, figure 7.9b and c show examples where all peaks shift to more positive or more negative potentials, respectively, when the lever is reduced.

To understand this behavior, we start from the expression that relates the onset of electron tunneling at positive bias ($V_{e_1}^+$) to the first electron level (written as the sum of the level energy e_1 and the polarization energy Σ_e) and the lever arm:

$$V_{e_1}^+ = \frac{e_1 + \Sigma_e}{e\eta} \tag{7.5}$$

A similar expression holds for the onset of hole tunneling at negative bias ($V_{h_1}^-$), where we the energy h_1 of the first hole state has a negative value:

$$V_{h_1}^- = \frac{h_1 - \Sigma_h}{e\eta)} \tag{7.6}$$

Importantly, with a lever arm close to 0.5, also electron tunneling at negative bias and hole tunneling at positive bias are feasible. The respective onset energies $V_{e_1}^-$ and $V_{h_1}^+$ read:

$$V_{e_1}^- = -\frac{e_1 + \Sigma_e}{e(1-\eta)} \tag{7.7}$$

$$V_{h_1}^+ = -\frac{h_1 - \Sigma_h}{e(1-\eta)} \tag{7.8}$$

One easily shows that the derivatives $dV_{e_1}^+/d\eta$ and $dV_{e_1}^-/d\eta$ are negative, while $dV_{h_1}^-/d\eta$ and $dV_{h_1}^+/d\eta$ are positive. Hence, upon reduction of η, electron tunneling peaks shift to positive potentials while hole tunneling peaks shift to negative potentials.

Returning to figures 7.9a-c, one finds that only figures 7.9a describes the regular situation where electrons tunnel at positive bias and holes tunnel at negative bias. Figures 7.9b and c on the other hand represent situations of hole-only and electron-only

tunneling. Focusing on figure 7.9b, it follows from eqs. 7.6 and 7.8 that the lever arm is obtained as:

$$\eta = \frac{V_{h_1}^{+} - V_{h_1}^{-}}{V_{h_1}^{+}} \tag{7.9}$$

For the example shown in figure 7.9b, we thus obtain a lever arm changing from 0.53 to 0.49 with increasing setpoint current, i.e., an almost symmetric junction. A similar exercise on the spectrum shown in figure 7.9c yields a lever arm decreasing from 0.43 to 0.4.

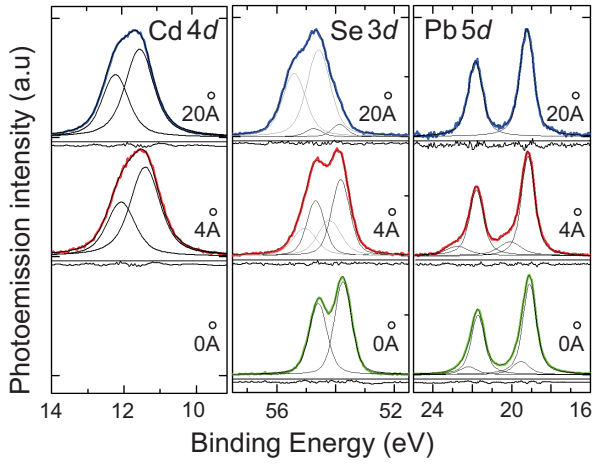

Figure 7.10: Background-substracted Cd 4d, Se 3d, and Pb 5d core-level spectra and fits of PbSe/CdSe NCs with different CdSe shell thickness given in angstrom, as indicated in the graph. The residual plots are also shown below each core-level spectrum.

The different spectra obtained at different dots suggest that different PbSe/CdSe core/shell QDs are present on the substrate, which complicates a consistent attribution of the STS features to QD energy levels. In order to clarify this point, x-ray photoemission spectroscopic experiments have been performed on the same sample. For comparison, two additional types of NCs were investigated: a sample consisting of PbSe NCs only and a sample with PbSe/CdSe core-shell NCs, where the thickness of the shell was 2 nm.

When the XPS spectra of all three samples are compared (figure 7.10), the successful cation exchange between Pb and Cd, at

the surface of the NCs considered in the STS study, is demonstrated through (i) the presence of Cd 4d photoelectron lines for both types of NCs containing Cd, and (ii) the occurrence of a Se 3d peak that shows an intermediate lineshape between the lineshape obtained for the PbSe NCs and the PbSe NCs surrounded by a thick CdSe shell.

Indeed, as Se atoms are bound to both Pb and Cd atoms, two spin-orbit split doublets are required in order to decompose the Se 3d core level (binding energies of 53.82 and 54.21 eV for the two first peaks). Moreover, the fitting procedure shows that the lineshape of the PbSe/CdSe NCs with a thin shell is closer to the lineshape of the Se 3d peak for PbSe NCs, suggesting that the NCs contain a higher quantity of Se atoms bound to Pb atoms than Se atoms bound to Cd atoms. Such a result is consistent with a thin layer of CdSe.

As for the Pb 5d core level, the Pb $5d_{5/2}$ (lower binding energy) and Pb $5d_{3/2}$ (higher binding energy) peaks are decomposed with a single component that is related to the Pb atoms bound to Se atoms in the core for the NCs with the thick shell. For the Pb $5d_{5/2}$ peak, this component is centered at a binding energy of 19.27 eV and has a FWHM of 0.84 eV. Conversely, the Pb $5d_{5/2}$ peak of the PbSe NCs requires the use of two components. From the comparison of the peak position with the one obtained for the PbSe/CdSe NCs with a thick shell, we attribute the component at the lowest binding energy, centered at 19.10 eV (FWHM 0.80 eV), to the bulk contribution of the NCs. The second peak with the highest binding energy, centered at 19.53 eV (FWHM 1.05 eV), is thus related to the surface. Its position as well as its width would correspond to surface Pb atoms bound to oxygen, in agreement with results reported for the oxidation of PbSe. Such PbO species exist due to the passivation of the NC surface with ligands and also because the surface of the NCs might oxidize during the transfer of the NCs in air. The observation of this shoulder means that a part of the NC surface exposed uncovered PbSe facets, where the Pb atoms are bound to O species.

In summary, these results indicate that a large number of NCs have a partial CdSe shell, leaving one or several PbSe facets unprotected, in agreement with TEM images of similar NCs where the shell was even thicker. Such variations in the shell thickness from one NC to another might explain why three types of tunneling

spectra have been found.

Conclusions

In conclusion we have measured scanning tunneling spectra on PbSe/CdSe core-shell NCs. For part of the NCs, we have found a unipolar transport regime, where only one type of charge carriers contribute to the tunneling current on each side of the zero-conductance gap. However, situations of hole-only and electron-only transport are equally found. In these cases, a lever-arm of around 0.5 is typically calculated. Based on XPS analysis, we conclude that at least part of the PbSe/CdSe QDs analyzed only have a partial CdSe shell. Therefore, differences in shell homogeneity and in NC orientation relative to tip and substrate will strongly affect the tunneling spectra and can explain why three types of tunneling spectra have been found.

Bibliography

[1] Anikeeva, P. O.; Halpert, J. E.; Bawendi, M. G.; Bulovic, V. Quantum Dot Light-Emitting Devices with Electroluminescence Tunable over the Entire Visible Spectrum 2009. *Nano Letters* **2009**, *9*, 2532–2536.

[2] Konstantatos, G.; Clifford, J.; Levina, L.; Sargent, E. Sensitive solution-processed visible-wavelength photodetectors. *Nature Photonics* **2007**, *1*, 531–534.

[3] Li, X.; Zhou, Y.; Zheng, Z.; Yue, X.; Dai, Z.; Liu, S.; Tang, Z. Glucose Biosensor Based on Nanocomposite Films of CdTe Quantum Dots and Glucose Oxidase. *Langmuir* **2009**, *25*, 6580–6586.

[4] Rogach, A. L.; Klar, T. a.; Lupton, J. M.; Meijerink, A.; Feldmann, J. Energy transfer with semiconductor nanocrystals. *Journal of Materials Chemistry* **2009**, *19*, 1208.

[5] Justo, Y.; Moreels, I.; Lambert, K.; Hens, Z. Langmuir Blodgett monolayers of colloidal lead chalcogenide quantum dots : morphology and photoluminescence. *Nanotechnology* **2010**, *21*, 295606.

[6] Lambert, K.; Capek, R. K.; Bodnarchuk, M. I.; Kovalenko, M. V.; Thourhout, D. V.; Heiss, W.; Hens, Z. Langmuir-Schaefer Deposition of Quantum Dot Multilayers. *Langmuir* **2010**, 6352–6353.

[7] Jasieniak, J.; Bullen, C.; van Embden, J.; Mulvaney, P. Phosphine-free synthesis of CdSe nanocrystals. *The journal of physical chemistry. B* **2005**, *109*, 20665–8.

[8] Cademartiri, L.; Bertolotti, J.; Sapienza, R.; Wiersma, D. S.; von Freymann, G.; Ozin, G. a. Multigram scale, solventless, and diffusion-controlled route to highly monodisperse PbS nanocrystals. *The journal of physical chemistry. B* **2006**, *110*, 671–3.

[9] Moreels, I.; Justo, Y.; De Geyter, B.; Haustraete, K.; Martins, J. C.; Hens, Z. Size-Tunable, Bright, and Stable PbS Quantum Dots: A Surface Chemistry Study. *ACS Nano* **2011**, *5*, 2004–2012.

[10] Murray, C. B.; Sun, S. H.; Gaschler, W.; Doyle, H.; Betley, T. A.; Kagan, C. R. Colloidal synthesis of nanocrystals and nanocrystal superlattices. *Ibm Journal of Research and*

Development **2001**, *45*, 47–56.

[11] Pietryga, J. M.; Werder, D. J.; Williams, D. J.; Casson, J. L.; Schaller, R. D.; Klimov, V. I.; Hollingsworth, J. a. Utilizing the lability of lead selenide to produce heterostructured nanocrystals with bright, stable infrared emission. *Journal of the American Chemical Society* **2008**, *130*, 4879–85.

[12] Liljeroth, P.; van Emmichoven, P.; Hickey, S.; Weller, H.; Grandidier, B.; Allan, G.; Vanmaekelbergh, D. Density of States Measured by Scanning-Tunneling Spectroscopy Sheds New Light on the Optical Transitions in PbSe Nanocrystals. *Physical Review Letters* **2005**, *95*, 1–4.

[13] Grinbom, G. a.; Saraf, M.; Saguy, C.; Bartnik, a. C.; Wise, F.; Lifshitz, E. Density of states in a single PbSe/PbS core-shell quantum dot measured by scanning tunneling spectroscopy. *Physical Review B* **2010**, *81*, 1–7.

Chapter VIII

Multiple dot-in-rod PbS/CdS heterostructures

8.1 Introduction

Colloidal quantum rods (QRs) are an attractive class of nanocrystals. Either grown out of a single material or as a heterostructure, the combination of quantum confinement and shape anisotropy results in materials with tunable, anisotropic opto-electronic properties. A typical example are heterogeneous CdSe/CdS dot-in-rods.[1,2] These materials exhibit a highly efficient, polarized photoluminescence (PL) tunable from green to red and their homogeneity allows to assemble them in close-packed ordered arrays.[3] However, with bulk bandgaps of 1.74 (CdSe) or 2.40 eV (CdS), cadmium chalcogenide (CdX) QRs are mainly of interest for applications involving visible light. In this communication, we extend the PL wavelength range of colloidal QRs to the near infrared (NIR) by demonstrating the formation of efficiently emitting heteronanorods that feature multiple PbS dots in a single CdS rod. In the case of CdX, rod growth is made possible by the combination of an anisotropic crystal structure (wurtzite) and specific surface ligands (phosphonic acids).[4] The synthesis of QRs active in the NIR ($\sim$ 800-3000 nm) has proved to be more challenging. Lead chalcogenides (PbX), the most widely used NIR quantum dots (QDs), have a cubic crystal structure. In that case, rod or wire growth has only been achieved with indirect methods such as chelation of the precursors,[5] heterogeneous seeding,[6] cationic exchange[7] or oriented attachment of QDs.[8] In the case of cationic

exchange, it was shown that CdS QRs can be transformed into PbS QRs by two successive exchange steps. This has the advantage that the enormous variety of sizes, aspect ratios and materials accessible via CdX QR synthesis can transferred to PbX QRs. However, by repeating the procedure proposed by Luther et al.[7] we found that an important drawback of the resulting PbS QRs is a low PL quantum yield (PLQY). This makes these materials, unlike CdSe/CdS dot-in-rods, not appropriate for high end applications such as wavelength down-conversion or optical amplification. Here, we show that NIR QRs with high PLQY can be made by extending the cationic exchange approach with one additional step in which Pb is partially replaced by Cd. By controlling the exchange conditions, this results in PbS/CdS QRs with a PLQY of 45-55%. Moreover, high angle annular dark field scanning transmission electron microscopy (HAADF-STEM) makes clear that the resulting heterostructures are composed of a chain of multiple PbS dots embedded in a CdS rod. Although in this case, electronic coupling between the different PbS dots appears to be small, the synthesis procedure provides extensive freedom for tuning. Hence, the approach presented here not only leads to anisotropic NIR QRs with a high PLQY yet may also enable the formation of electronically coupled QDs embedded in a single colloidal QR.

8.2 Experimental

The starting material are CdS QRs synthesized with a seeded growth approach following Carbone et al.[2] The exchange into PbS rods is done with an intermediate step of Cu_2S rods and it is based on the procedure of Luther et al.[7] The successive Cd/Cu and Cu/Pb exchanges are promoted by methanol and tributylphosphine, respectively. In the first step, CdS rods are mixed with tetrakis(acetonitrile)copper(I) hexafluorophosphate dissolved in methanol. A Cu:Cd excess of 20:1 is used. The reaction is performed inside a nitrogen-filled glovebox at room temperature. After washing the sample, the Cu_2S rods obtained are transformed into PbS rods by injecting a mixture of lead acetate and tri-n-butylphosphine. The final product is washed twice with methanol and stored in toluene under vacuum.

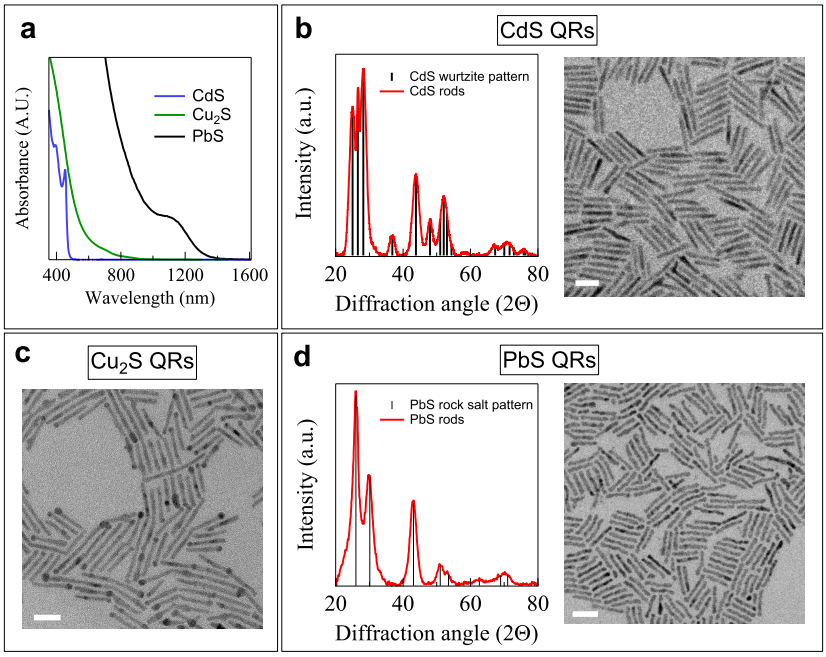

Figure 8.1: a) Absorption spectra of all the successive cationic exchange steps. b) XRD difractrogram and TEM overview of the CdS QRs. c) TEM overview of Cu_2S QRs. d) XRD and TEM overview of PbS QRs. All the scale bars are 20 nm.

8.3 Results

8.3.1 From CdS to PbS nanorods

The initial CdS rods have dimensions of (diameter:length) 3.7:28 nm. As shown in figure 8.1a, these rods have a pronounced absorption peak at 480 nm, which is characteristic of the CdS band gap transition. They have the wurtzite crystal structure and the TEM overview image shows that they are regular and monodisperse (see figure 8.1b). After the exchange of Cd for Cu, the absorption spectrum loses its features (figure 8.1a) and in the TEM overview image, it can be seen that some of the QRs contain clusters at the tip (figure. 8.1c). We find that the successive exchange steps transform the absorption peak of the CdS bandgap transition in the visible in a shoulder at 1100 nm, which is characteristic of PbS (figure 8.1a).

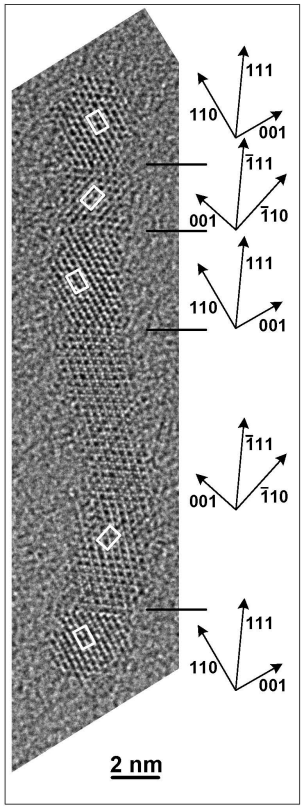

Figure 8.2: HR_TEM image of a PbS QR on a [110] zone axis. The white rectangles indicate the ⟨110⟩ unit cell, and the arrows show the three major crystal directions in the five crystal segments that constitute the rod.

Figure 8.2 shows that the PbS QRs thus formed are polycrystalline, with the different crystallites separated by [111] twin planes. A similar observation was reported by Luther et al.[7] who interpreted this as a result of the formation of two PbS segments at either end of the rod, resulting in a grain boundary where the reaction fronts meet. Here, high resolution TEM indicates that the PbS QRs can be composed of more than two segments (figure 8.2). In the example given, five segments can be discerned but their actual number changes depending on, e.g., the length of the QR. This indicates that the exchange can also start at the sides of the QRs. Possibly, this is driven by stacking faults in the original CdS rods. Figure 8.3 shows a high resolution TEM image of a starting CdS rod and the presence of multiple wurtzite/zincblende

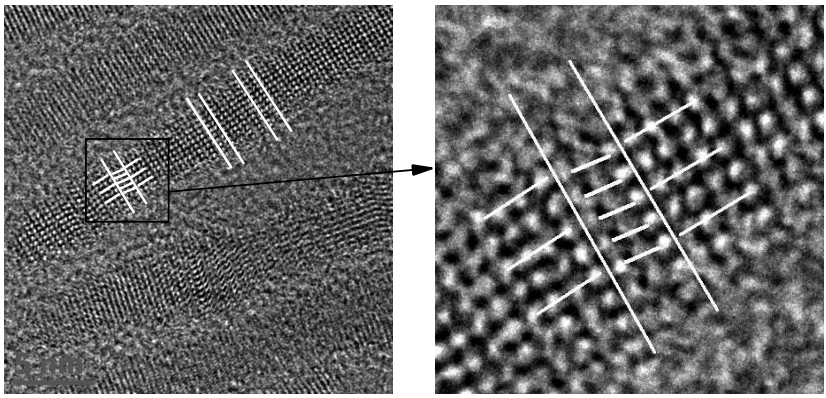

Figure 8.3: HR_TEM pictures of CdS rods where stacking faults are present and marked between the lines.

stacking faults in successive ⟨110⟩ planes perpendicular to the c-axis. The distance between different stacking faults is similar to that between twin planes in the final PbS rods. All the TEM images were taken by Dr. John Sundar Kamal.

STEM-EDX indicates that the rods made by successive cationic exchange only contain Pb and S. Nevertheless, STEM-HAADF imaging (figure 8.4) shows that small, 1-2 nm clusters are present at their surface. Since the STEM-HAADF signal intensity increases with the atomic weight of the element probed, these clusters are Pb rich as compared to the PbS QRs. Possibly, these are PbS clusters with a Pb surface termination or metallic Pb particles. Luther et al.[7] reported a PbS exchange made at room temperature. We performed the exchange form Cu to Pb at 0℃. Figures 8.4d,e show an overview of PbS QRs exchanged at 0℃. The images indicate that the exchange at low temperature leads to more homogeneous QRs that show less small clusters in solution. However, the STEM-HAADF image in figure 8.4f shows that the PbS QDs still have particles at the surface of the QRs. HAADF-STEM images were taken by Bart Goris at the EMAT unit of Prof. Sara Bals at the University of Antwerp.

8.3.2 Cationic exchange on PbS QRs

The main drawback of the resulting PbS QRs is their low PLQY of about 9%. In the case of PbX QDs, growth of a CdX shell by cationic exchange has been proposed as a way to enhance and

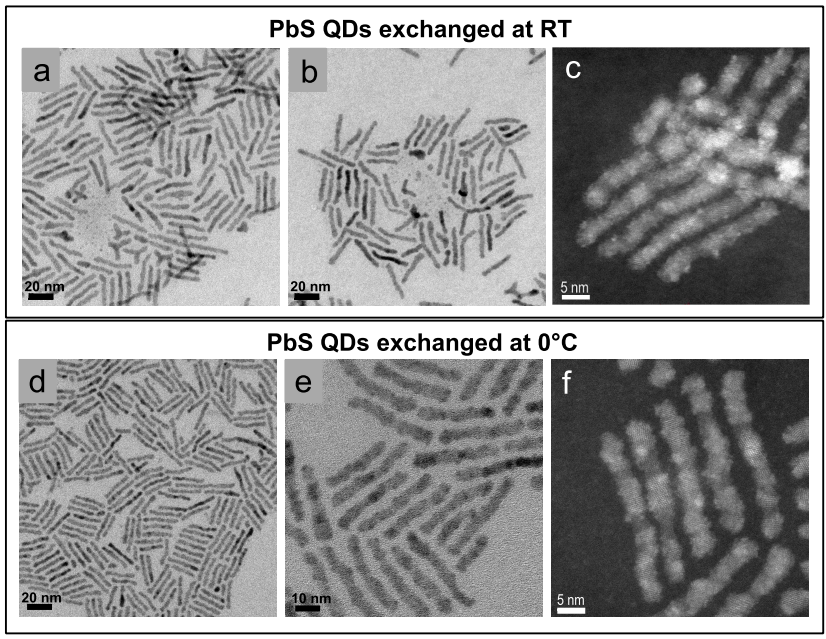

Figure 8.4: a,b) TEM overview of PbS QRs made at RT, c) HAADF image showing also small clusters attached to the surface of the QRs. d, e) Overview of PbS QRs exchanged at 0℃. f) HAADF image shows that the PbS QDs still have particles at the surface of the QRs.

stabilize the PLQY.[9,10] In line with this result, we have exposed a suspension of PbS QRs in toluene to an excess of Cd oleate at elevated temperature. Elemental analysis by TEM-EDX shows that this leads to a progressive replacement of Pb by Cd, which is more pronounced the longer the reaction time or the higher the temperature (figure 8.5a). For exchange temperatures of 65 to 100℃, 45-95% of the Pb atoms are replaced by Cd, corresponding to a nominal shell thickness of 0.4-1.2 nm, respectively. As compared to the original PbS QRs, the PL spectrum of the PbS/CdS heterorods shifts to shorter wavelengths and, more importantly, the PLQY increases sharply. After 120 min of shell growth, it reaches 45 or 55% if the exchange is done at 65 or 80℃, respectively (figure 8.4b).

The morphology of the QRs was studied in detail using STEM-HAADF. With core/shell PbS/CdS heterorods, this should result in images showing a bright (PbS) core and a darker (CdS) shell.

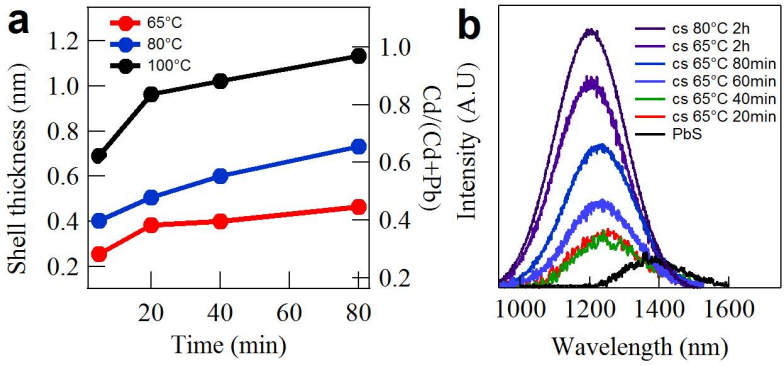

Figure 8.5: (a) Evolution of the ratio Cd/(Pb+Cd) and the nominal CdS shell thickness as a function of the reaction time for different reaction temperatures. (b) Evolution of the PL spectrum with reaction time for an exchange reaction at 65°C, and final PL spectrum for an exchange reaction at 80°C

This is not what is observed. Figure 8.6 shows several rods with the final Pb for Cd exchange done at 65°C, the overview image (figure 8.6a) already shows that each rod is composed of a series of brighter and darker segments, featuring 4-5 bright parts. Figure 8.6b demonstrates that the bright segments are embedded in the darker rod. We interpret this as evidence for the formation of multiple PbS dots in a single CdS rod. Similar results are obtained when starting from CdS rods with different aspect ratios like figure 8.6d with dimensions of 4:14 nm, or with dimensions of 5:16.5 nm (figure 8.7). In the latest case, the absorption and emission peak are shifted towards longer wavelengths because of the larger diameter (figure 8.7d, e). This proves the fact that the synthesis has a lot of room for tuning. A high-resolution STEM image (figure 8.6c) shows that the polycrystallinity of the original PbS QRs is maintained in the PbS/CdS heterorods. Moreover, it appears that each PbS segment is transformed into a single PbS/CdS segment. This follows more clearly from the STEM-HAADF image of a sample with shorter rods 4:14 nm (figure 8.6d), where the resulting PbS/CdS rod features two segments that contain a single PbS dot each. This indicates that the multiple dot-in-rod heterostructures form because the cationic exchange proceeds quickly along the (defect rich) interfaces between the original PbS segments. Importantly, this suggests that the morphology of these

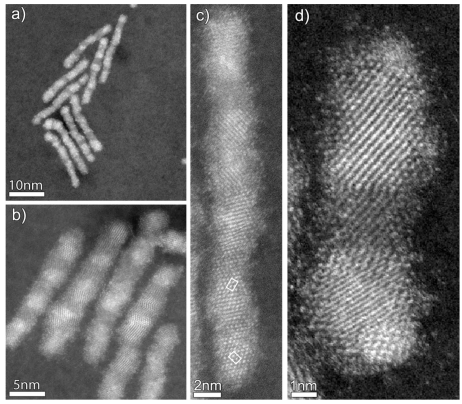

Figure 8.6: STEM-HAADF images of PbS/CdS rods showing multiple PbS QDs inside the rods recorded on (a-c) sample A and (d) sample B. The white rectangles in (c) indicate the ⟨110⟩ unit cell.

multiple dot-in-rod heterostructures can be tuned by adjusting the size of the PbS segments in the original PbS rods. Possibly, these reactive interfaces account for the difference with PbX rods made by oriented attachment, where partial Pb/Cd exchange rarely leads to multiple dot-in-rods.[11]

8.3.3 Electronic properties of multiple PbS/CdS dot-in-rods

Averaging over 150 embedded PbS dots of the sample shown in figure 8.6a,b,c, we find an effective average diameter of 3.7 nm with a size dispersion of 15%. Similar results, albeit with less homogeneous PbS dots, are obtained with a Pb for Cd exchange at 80°C (figure 8.8). Spherical PbS QDs of the same size have their first exciton absorption and emission at 1100 and 1200 nm, respectively. For the multiple dot-in-rods, we obtain a shoulder in the absorption spectrum at 1050 nm and a PL maximum at 1200 nm. This correspondence suggests that electronic coupling between the PbS dots in a single PbS/CdS multiple dot-in-rod is limited.

To analyze this further, we used effective mass modeling as a crude approximation to calculate the electron and hole states. The model solves the stationary Schrödinger equation in three dimensions under the effective mass approximation using a finite

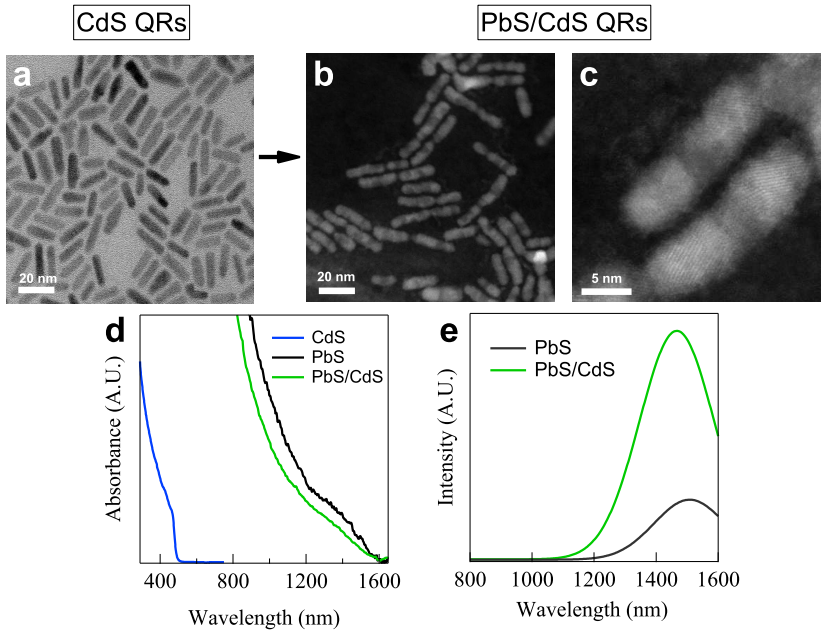

Figure 8.7: Cation exchange made on sample with dimensiond 5:16.5nm. a) CdS rods. b), c) STEM-HAADF pictures of PbS/CdS rods after the cationic exchange. c) Absorption spectra of the QRs at the different steps of the cationic exchange. d) Comparison of the PL intensity of the PbS and PbS/CdS QRs exchanged at 65C for 2hours.

element solver. The geometrical parameters are obtained from HR-TEM analysis. Band offsets of 1.2 eV and 0.9 eV for the valence and conduction band respectively are based on literature values for the PbS/CdS heterojunction. Effective mass parameters are taken from the bulk semiconductors.[12]

The electron and hole wave functions are shown in figure 8.9 for the case of 4 dots in rod and comparable single dot samples. For the electron in the dots-in-rod, 4 states with similar energies are found around 800 meV. Similar values are found for the single dot geometry. A splitting of about 20 meV is observed between the symmetric and anti-symmetric states E1 and E2. In figure 8.9, one can clearly see the electron leakage in the shell regions. Based on the amplitude of the wavefunction, the probability to find the electron localized in the core region is about 60%. For the hole in the dots-in-rod, also 4 states with similar energy are found around 340 meV. Again, similar values are found for the core/shell single

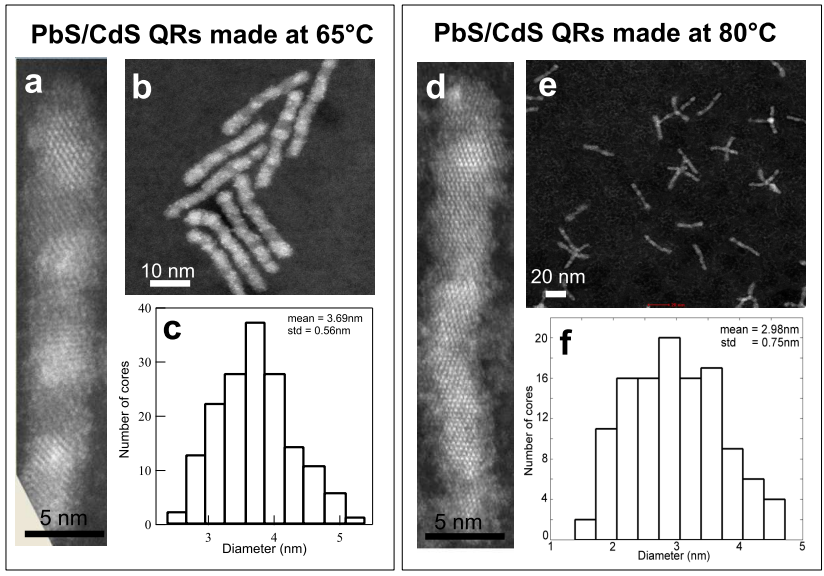

Figure 8.8: Comparison between PbS/CdS QRs exchanged at 65℃and at 80℃. a), b) overview of the QRs exchanged at 65℃, c) histogram of the dots inside the QRs exchanged at 65℃. d), e) overview of the QRs exchanged at 80℃, f) histogram of the dots inside the QRs exchanged at 80℃.

	Electron mass	Hole mass
PbS	0.04	0.04
CdS	0.1	0.8

Table 8.1: Electron and hole effective masses used in simulations.

dot geometry. At the level of the hole wavefunctions, the dots are truly decoupled as there is only a limited wavefunction leakage and almost no energy splitting (not even on a meV scale as for the electron). In figure 8.9, one can see this limited hole leaking into the shell region. We find the probability of hole core-localization to be around 80%.

To understand the coupling of dots in more detail, we perform a sweep of the dot radius and separation length. For numerical simplicity, we calculate the coupling for a hypothetical 3.7:28 nm CdS rod containing two PbS dots of radius R separated by a distance L_{sep} (figure 8.10a). The resulting states thus correspond to

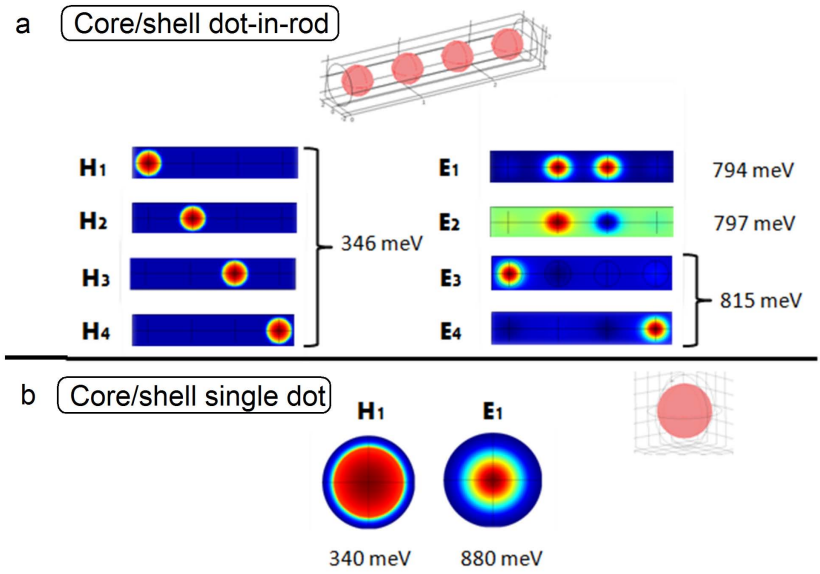

Figure 8.9: Effective mass simulation geometry and output for core/shell dot-in-rod (a) and single dot (b) samples. The lowest energy hole (Hi) and electron (Ei) states are plotted with their respective eigenenergies.

the E1 and E2 states of figure 8.9. Electronic coupling between conduction and valence band states is quantified by the energy splitting between the resulting bonding and anti-bonding states in this double-dot geometry (figure 8.10b). Similar to what was found with PbSe/CdSe, we find that the hole states remain confined in the PbS dots due to the large mismatch between the hole effective masses in PbS and CdS.[13] As shown in figure 8.10c, the hole coupling is negligible unless L_{sep} reaches the dot diameter $2R$. On the other hand, the smaller difference between the electron effective masses leads to leakage of the electron wavefunction outside the PbS dots (figure 8.10d), resulting in a more significant coupling. For $R = 1.85$ nm, an energy splitting comparable to k_BT is achieved for a center-to-center distance less than 5 nm. This suggests that a 28 nm CdS rod containing 4-5 PbS dots is at the edge of the regime where quantum coupling between adjacent dots influences the optical properties of a multiple dot-in-rod PbS/CdS at room temperature. This model was performed by Pieter Geiregat.

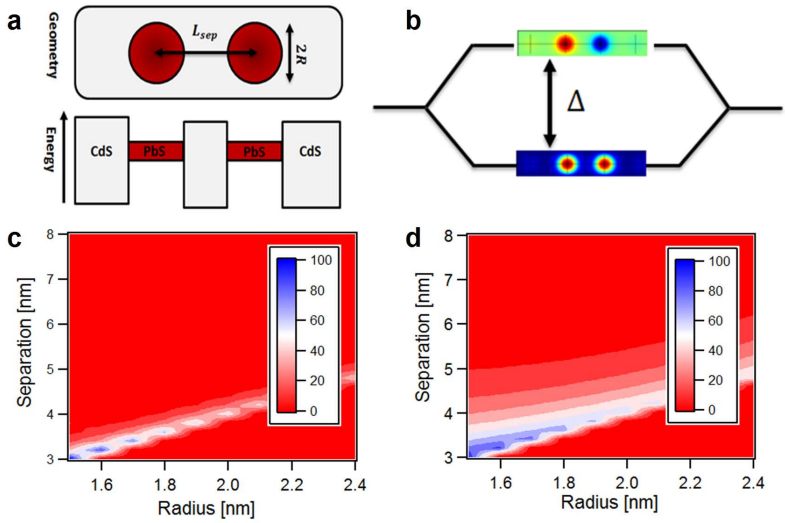

Figure 8.10: (a) Simulation geometry of (red) two PbS dots of radius R in a (grey) CdS rod separated by Lsep. (b) Energy diagram of the bonding and antibonding states obtained after electronic coupling of the two dots. (c,d) Energy difference between the bonding and antibonding states as a function of dot radius (x axis) and dot-dot separation (y axis) for (c) the higher energy hole state and (d) the lowest energy electron state. Only the region where Lsep > 2R is physically relevant.

8.4 Conclusions

In conclusion, we have used successive cationic exchange steps to synthesize colloidal PbS/CdS heterorods with a high PLQY in the NIR out of CdS quantum rods. The successive, complete Cd/Cu and Cu/Pb exchanges lead to polycrystalline PbS QRs with a limited PLQY. A final Cd/Pb partial exchange raises the PLQY up to 55%. Instead of simple core/shell structures, this results in the formation of multiple dot-in-rod heterostructures, probably because each PbS segment in the original PbS QR is transformed into a single PbS/CdS unit. The number of PbS dots in a single rod depends on the original CdS rod length. Since further tuning is possible by limiting the extent of the final cationic exchange,[7] this shows that successive cationic exchange is a versatile approach to form complex anisotropic heteronanostructures active in the IR. The correspondence between the first exciton absorption and emission wavelength of the PbS/CdS multiple dot-in-rods and

simple PbS dots suggests that quantum coupling between the dots in a single rod is limited for the geometries studied here, a conclusion supported by effective mass calculations. Nevertheless, the novel nanostructures developed here - providing unique colloidal QRs with high photoluminescence quantum yield in the NIR - can spark a wide range of follow-up research. This may involve pushing the system towards quantum coupling, extending the approach to other materials systems like PbSe/CdSe, a detailed analysis of the exciton fine structure, quantum coupling and the properties of multiple excitons and the development of applications in, e.g., solar concentrators and QD based NIR light sources.

Bibliography

[1] Talapin, D. V.; Koeppe, R.; Go, S.; Kornowski, A.; Lupton, J. M.; Rogach, A. L.; Benson, O.; Feldmann, J.; Weller, H. Highly Emissive Colloidal CdSe / CdS Heterostructures of Mixed Dimensionality. *Nano* **2003**, 0–4.

[2] Carbone, L. et al. Synthesis and micrometer-scale assembly of colloidal CdSe/CdS nanorods prepared by a seeded growth approach. *Nano letters* **2007**, *7*, 2942–50.

[3] Zanella, M.; Gomes, R.; Povia, M.; Giannini, C.; Zhang, Y.; Riskin, A.; Van Bael, M.; Hens, Z.; Manna, L. Self-assembled multilayers of vertically aligned semiconductor nanorods on device-scale areas. *Advanced materials (Deerfield Beach, Fla.)* **2011**, *23*, 2205–9.

[4] Peng, X.; Manna, L.; Yang, W.; Wickham, J.; Scher, E.; Kadavanich, a.; Alivisatos, A. Shape control of CdSe nanocrystals. *Nature* **2000**, *404*, 59–61.

[5] Lifshitz, E.; Bashouti, M.; Kloper, V.; Kigel, a.; Eisen, M. S.; Berger, S. Synthesis and Characterization of PbSe Quantum Wires, Multipods, Quantum Rods, and Cubes. *Nano Letters* **2003**, *3*, 857–862.

[6] Yong, K.-T.; Sahoo, Y.; Choudhury, K. R.; Swihart, M. T.; Minter, J. R.; Prasad, P. N. Shape control of PbSe nanocrystals using noble metal seed particles. *Nano letters* **2006**, *6*, 709–14.

[7] Luther, J. M.; Zheng, H.; Sadtler, B.; Alivisatos, a. P. Synthesis of PbS nanorods and other ionic nanocrystals of complex morphology by sequential cation exchange reactions. *Journal of the American Chemical Society* **2009**, *131*, 16851–7.

[8] Koh, W. K.; Bartnik, A. C.; Wise, F. W.; Murray, C. B. Synthesis of Monodisperse PbSe Nanorods: A Case for Oriented Attachment. *Journal of the American Chemical Society* **2010**, *132*, 3909–3913.

[9] Pietryga, J. M.; Werder, D. J.; Williams, D. J.; Casson, J. L.; Schaller, R. D.; Klimov, V. I.; Hollingsworth, J. A. Utilizing the lability of lead selenide to produce heterostructured nanocrystals with bright, stable infrared emission. *Journal of the American Chemical Society* **2008**, *130*, 4879–4885.

[10] Lambert, K.; Geyter, B. D.; Moreels, I.; Hens, Z.

PbTe—CdTe Core—Shell Particles by Cation Exchange, a HR-TEM study. *Chemistry of Materials* **2009**, *21*, 778–780.

[11] Casavola, M.; Huis, M. A. V.; Bals, S.; Lambert, K.; Hens, Z.; Vanmaekelbergh, D. Anisotropic Cation Exchange in PbSe/CdSe Core/Shell Nanocrystals of Different Geometry. *Chemistry of Materials* **2012**, *24*, 294–302.

[12] Schliiter, M. No Title. *Phys. Rev. B* **1975**, *11*, 651–659.

[13] De Geyter, B.; Justo, Y.; Moreels, I.; Lambert, K.; Smet, P. F.; Van Thourhout, D.; Houtepen, A. J.; Grodzinska, D.; de Mello Donega, C.; Meijerink, A.; Vanmaekelbergh, D.; Hens, Z. The different nature of band edge absorption and emission in colloidal PbSe/CdSe core/shell quantum dots. *ACS nano* **2011**, *5*, 58–66.

English Summary

Nanoscale materials frequently show behavior which is intermediate between that of a macroscopic solid and that of an atomic or molecular system. Due to their small sizes, they exhibit quantum confinement. This results in size-dependent properties, different from the bulk material. As an example, smaller QDs have an absorption spectrum that is shifted to shorter wavelengths with respect to larger QDs and to the bulk material. Depending on the band gap of the bulk material, the band gap of quantum dots can be tuned from the ultra violet to the infrared part of the electromagnetic spectrum. This work focuses on QDs active in the infra red, with emission wavelengths between 800 and 2500 nm. Applications operating in this wavelength range involve for example optical data communication, bio-imaging, photovoltaics or photodetection. Among the different NIR active QDs, this work is focused on IV-VI lead chalcogenides (PbX, X=S, Se, Te). Bulk PbX have a rocksalt crystal structure and their band gap lies at the L point instead of the Γ point of the Brillouin zone. Hence, the resulting first electron ($1S_e$) and hole ($1S_h$) levels are both 8-fold degenerate and optical gain or population inversion will therefore require 4 electron-hole pairs (excitons) in a quantum dot. This is a considerable complication since Auger recombination is a very efficient, non-radiative decay path for multiple excitons in semiconductor nanocrystals. The limitations Auger recombination can be overcome by changing the QD geometry or by the growth of core/shell heterostructures. These approaches have inspired most of the synthetic work in this study.

The synthesis method in this work is based on the hot injection synthesis developed in 1993. This synthesis route does not require any substrate and results in QD dispersions which allow for a flexible processing. However, the dispersions can not be used as such for their application in devices such as LEDs. For these purposes,

high-quality QD thin films are required. In this thesis, we first focus on QD synthesis and characterization. We then explore the possibilities of Langmuir-Blodgett (LB) and Langmuir-Schaefer (LS) deposition for the production of QD mono- and multilayers. In chapter II, we adapt the PbS QDs synthesis described by Cademartiri *et al.*, more specifically by employing TOP during the synthesis, a strongly enlarged range of QD sizes can be synthesized. Monodisperse suspensions with an average size between 3 and 10 nm can now be prepared *via* a one-step synthesis. However, a ligand exchange is needed in order to exchange OLA by OA. The OA ligands are tightly bound to the QD surface as oleate ions, hereby strongly enhancing the luminescence yield to values of up to 90%. The PbS QDs are air-stable in suspension, offering prospects for operation of PbS QD-based photonic devices under ambient conditions.

In chapter III we explore the possibilities of the cationic exchange reaction to develop PbX heterostructures. Our experimental data shows that the thickness of the shell can tuned by modifying several reaction parameters. Variations on the reaction time or the excess of Cd lead to a certain shell thickness which reaches a saturation value after exchanging few atomic layers. Temperature is the only parameter that can be tuned to get thicker shells. In literature, there are several attempts to explain the mechanism of the exchange reaction. After exploring them, we propose a diffusion model that is limited by the different mean square displacement of the atoms on the surface of the QDs compared to that of the inner ones. This difference increases the activation energy barrier, stopping the reaction. An increase in temperature leads to a decrease of the height of the energy barrier, giving rise to thicker shell thickness.

In chapter IV and V, we study the opto-electronic properties of PbSe/CdSe and PbS/CdS QDs respectively. In the case of PbSe/CdSe QDs we show that both the energy and the absorption oscillator strength of the first absorption peak in PbSe/CdSe quantum dots follow the same trend with core diameter as PbSe QDs. On the other hand, PL lifetime measurements yield an oscillator strength in emission that is reduced by at least 75%, compared to the PbSe/CdSe oscillator strength from absorption and the PbSe QD oscillator strength in absorption and emission. This result in combination with the significantly increased Stokes

shift of PbSe/CdSe QDs compared to that of PbSe, we conclude that the band gap emission in PbSe/CdSe QDs comes from fundamentally different states with lower oscillator strength that are energetically well separated from the absorbing states at room temperature. Moreover, these emitting states are different than the emitting states in PbSe QDs.

In the case of PbS/CdS QDs, we obtain their intrinsic absorption coefficient as a function of V_s/V_{tot}. Moreover, we can use this value to calculate the volume fraction or the concentration of dispersed PbS/CdS core/shell QDs. Regarding the time-resolved PL, for PbS and PbS/CdS QDs, smaller cores yield longer lifetimes with typical values between 1 and 3 μs. Oscillator strength in absorption and emission coincide for PbS/CdS QDs with d>5 nm. However, for smaller sizes, emission oscillator strength is markedly smaller than that of absorption. This indicates that the exciton is trapped in states with lower oscillator strength due to an increase on level spacing. A similar trend, although less pronounced, is also found for PbS QDs. Similar behavior of PbS/CdS and PbS QDs regarding lifetimes and oscillator strength indicate that the electron and hole in a PbS/CdS core/shell QD are both confined inside the PbS core. Hence, we can conclude that the CdS shell growth around the PbS core leads to a simple type-I regime.

In chapter VI, we analyze the formation of monolayers of PbS core, PbSe core QDs and of PbSe/CdSe core/shell QDs using Langmuir-Blodgett deposition and we have compared the photoluminescence properties of these LB films. In spite of qualitative differences in initial spreading, densely packed monolayers of both PbSe and PbS QDs can be obtained. While PbS QDs exhibit good, local ordering in the LB monolayer, PbSe QDs show a fusion of particles, probably related to the oxidation of these QDs either in suspension or in the Langmuir film. This can be prevented by the growth of a CdSe shell around the PbSe core. The improved stability of the QDs leads to a well ordered hexagonally close-packed structure. In spite of the improved film quality for PbSe/CdSe and PbSe QDs, only the PbS QD LB films retain their photoluminescence after LB processing. For both PbSe and PbSe/CdSe, the LB film luminescence is almost completely quenched. Although PbS QDs films are luminescent, they undergo oxidation under ambient conditions, causing a blueshift of the photoluminescence peak. Although this oxidation leads to a

final decrease in effective size of about 1 nm after one month, the films maintain their photoluminescence. These results indicate that PbS QDs are the preferred material for near-infrared light-emitting applications based on lead chalcogenide LB films.

In chapter VII, we take advantage of the excellent quality of the LB films to study the formation of different quantum dots mono and multilayers, and use them for analyzing the properties of quantum dots in close packed films. On one hand, we show that the continued compression of monolayers of a variety of colloidal QDs leads to a sequence of plateaus in the $\pi - A$ isotherm. Using Transmission Electron Microscopy (TEM) and Atomic Force Microscopy (AFM), we find that these plateaus correspond to the consecutive formation of a QD double and triple layer. Moreover, we argue that these transformations correspond to phase transitions in the Langmuir film that can be rationalized based on thermodynamic considerations. On the other hand, we compare the absorbance cross section of PbS and CdSe QDs in colloidal solutions and in close packed monolayers. We find that it can be enhanced up to a factor of 4 (CdSe) or 5 (PbS). Especially in the case of PbS QDs, the enhancement shows a marked, resonance-like diameter dependence, with a maximum value for QDs of around 4 nm. Finally, we have investigated layers of PbSe/CdSe core/shell NCs by means of scanning tunneling spectroscopy (STS) at low temperatures. Here, we show that the potential drop across both potential barriers is rather symmetric when we study PbSe/CdSe core-shell NCs with an intended shell thickness of 0.4 nm. It reveals the existence of a partial shell, which accounts for the fluctuations of the potential drop measured across the tunnel barriers, depending on the orientations that the NCs have adopted on the substrate.

In chapter VIII, we use successive cationic exchange steps to synthesize colloidal PbS/CdS heterorods with a high PLQY in the near IR out of CdS quantum rods. A final Cd/Pb partial exchange raises the PLQY up to 55%. Instead of simple core/shell structures, this results in the formation of multiple dot-in-rod heterostructures, probably because each PbS segment in the original PbS QR is transformed into a single PbS/CdS unit. The number of PbS dots in a single rod depends on the original CdS rod length. This shows that cationic exchange is a versatile approach to form complex anisotropic heterostructures in the IR.

Nederlandstalige Samenvatting

Materialen op nanoschaal vertonen frequent eigenschappen die zich intermediair bevinden tussen een macroscopische vaste stof en een atomair of moleculair systeem. Dankzij hun kleine afmetingen vertonen ze kwantumopsluiting. Dit resulteert in grootte-afhankelijke eigenschappen, die verschillen van het bulk materiaal. Kleinere QDs vertonen een absorptiespectrum dat verschoven is naar kortere golflengten in vergelijking met grotere QDs en het bulk materiaal. Afhankelijk van de verboden zone van het bulk materiaal, kan de verboden zone van de QDs gevarieerd worden van het ultraviolette tot het infrarode deel van het elektromagnetisch spectrum. Dit werk focust zich op QDs actief in het infrarood, met emissie golflengten die variëren tussen 800 en 2500 nm. Toepassingen in dit golflengtegebied zijn onder andere optische data communicatie, bio-beeldvorming, fotovoltaïsche zonne-energie en fotodetectie. Onder verschillende NIR actieve QDs richt dit werk zich op IV-VI lood chalcogeniden (PbX, X = S, Se, Te). Bulk PbX bezit een steenzoutstructuur met een verboden zone die zich op het L punt in plaats van het Γ punt van de Brillouin zone bevindt. Hierdoor worden het eerste electron ($1S_e$) en gat ($1S_h$) niveau elk 8-voudig gedegenereerd en optische winst of populatie inversie zal hierdoor 4 elektron-gat paren (excitonen) vereisen in een QD. Dit is een aanzienlijke complicatie omdat Auger recombinatie een zeer efficiënt, niet-radiatief verval pad is voor meerdere excitonen in halfgeleider nanokristallen. De limitaties van Auger recombinatie kunnen overwonnen worden door het veranderen van de QD geometrie of door de groei van kern/schil heterostructuren. Deze benaderingen hebben het grootste deel van het synthetisch werk in deze studie geïnspireerd. De gebruikte synthesemethode in dit werk is gebaseerd op de heteinjectie methode ontwikkeld in 1993. Deze syntheseroute vereist geen substraat en resulteert in QD dispersies die op een flexibele

manier verwerkt kunnen worden. Dispersies op zich kunnen echter niet gebruikt worden voor applicaties zoals LEDs. Hiervoor zijn QD dunne filmen nodig van hoge kwaliteit. In deze thesis richten we ons eerst op de synthese en karakterisatie van QDs. Vervolgens onderzoeken we de mogelijkheden van Langmuir-Blodgett (LB) en Langmuir-Schaefer (LS) depositie voor de productie van QD mono- en multilagen.

In hoofdstuk II passen we de PbS QD synthese aan beschreven door Cademartiri *et al.* Door het gebruik van TOP gedurende de synthese, vergroten we het bereik van QD afmetingen dat gesynthetizeerd kan worden. Hierdoor kunnen monodisperse suspensies met een gemiddelde afmeting tussen 3 en 10 nm aangemaakt worden in een n-stapssynthese. Hierbij dient wel een ligand uitwisseling te gebeuren waarbij OLA uitgewisseld wordt door OA. Deze OA liganden zijn sterk gebonden op het QD oppervlak als oleaat ionen, waardoor de luminescentie-opbrengst verhoogt wordt tot waarden die 90% benaderen. In oplossing zijn de PbS QDs stabiel aan lucht, wat mogelijkheden biedt voor het gebruik van fotonische apparaten gebaseerd op PbS QDs onder atmosferische omstandigheden.

In hoofdstuk III onderzoeken we de mogelijkheden van een kationenuitwisselingsreactie om PbX heterostructuren te ontwerpen. Onze experimentele data toont dat de dikte van de schil gevarieerd kan worden door verschillende reactieparameters. Variaties van de reactietijd of de overmaat Cd leiden tot een bepaalde schildikte die een verzadigingswaarde bereikt na de uitwisseling van enkele atoomlagen. De temperatuur is de enige parameter die gevarieerd kan worden om dikkere schillen te bekomen. In de literatuur zijn reeds verschillende pogingen beschreven om het reactiemechanisme van de kationenuitwisseling op te helderen. Nadat deze werden onderzocht, stellen wij een diffusie model voorop dat gelimiteerd is door verschillende kwadratische gemiddeldes van verplaatsing van atomen aan het oppervlak van de QDs vergeleken met de binnenste atomen. Dit verschil verhoogt de activeringsenergie waardoor de reactie stopt. Een verhoging van de temperatuur leidt tot een afname van de energiebarrière, wat leidt tot dikkere schillen.

In hoofdstuk IV en V bestuderen we de foto-elektrische eigenschappen van respectievelijk PbSe/CdSe en PbS/CdS QDs. In het geval van PbSe/CdSe QDs tonen we dat de energie en de

oscillator sterkte van de eerste absorptiepiek dezelfde trend vertonen in functie van kern diameter als in PbSe QDs. Daarentegen geven PL levensduur metingen een oscillator sterkte in emissie die gereduceerd is met minstens 75%, vergeleken met de oscillator sterkte van PbSe/CdSe uit absorptie en deze van PbSe QDs uit absorptie en emissie. Dit resulteert, in combinatie met de significant verhoogde Stokes verschuiving van PbSe/CdSe QDs vergeleken met PbSe, in een verboden zone emissie in PbSe/CdSe die uit fundamenteel verschillende niveaus met lagere oscillator sterkte komen, die energetisch gescheiden zijn van absorberende niveaus bij kamertemperatuur. Bovendien zijn deze emitterende niveaus verschillend van deze in PbSe QDs.
In het geval van PbS/CdS QDs bekomen we de intrinsieke absorptiecoëfficiënten in functie van V_s/V_{tot}. Bovendien gebruiken we deze waarde om het volume of de concentratie van gedispergeerde PbS/CdS kern/schil QDs te berekenen. Wat betreft tijdsafhankelijke PL van PbS en PbS/CdS QDs, geven kleinere kernen een langere levensduur met typische waarden tussen 1 en 3 μs. Oscillator sterkte in absorptie en emissie vallen samen voor PbS/CdS QDs met d>5 nm. Voor kleinere afmetingen is de oscillator sterkte in emissie echter sterker dan deze in absorptie. Dit duidt aan dat het exciton wordt vastgehouden in niveaus met een lagere oscillator sterkte door een toename in niveau afstand. Een vergelijkbare trend, hoewel minder uitgesproken, vinden we voor PbS QDs. Het vergelijkbaar gedrag van PbS/CdS en PbS QDs met betrekking tot levensduur en oscillator sterkte geeft aan dat het elektron en het gat in een PbS/CdS kern/schil QD beiden opgesloten zijn in de PbS kern. Hieruit besluiten we dat de CdS schil groei rond de PbS kern leidt tot een simpel type-I regime.
In hoofdstuk VI analyzeren we de vorming van monolagen uit PbS en PbSe kern QDs, en PbSe/CdSe kern/schil QDs, door het gebruik van LB depositie. Eveneens vergelijken we de fotoluminescentie-eigenschappen van de bekomen monolagen. Ondanks de kwalitatieve verschillen in initiële spreiding bekomen we dichtgepakte monolagen van zowel PbSe als PbS QDs. Terwijl PbS QDs goede lokale ordening vertonen in de LB monolaag, vertonen PbSe QDs een versmelting van deeltjes, wat waarschijnlijk gerelateerd is aan de oxidatie van deze QDs in dispersie of in de Langmuir film. Dit kunnen we voorkomen door de groei van een CdSe schil rond de PbSe kern. De verbeterde stabiliteit

van de QDs leidt tot een goed geordende hexagonaal dichtgepakte structuur. Ondanks de verbeterde kwaliteit van PbSe/CdSe en PbSe QD filmen ten opzichte van PbS QD LB filmen, behouden enkel deze laatste hun fotoluminescentie na het LB proces. Voor zowel PbSe als PbSe/CdSe is de luminescentie van de LB film bijna volledig verdwenen. Hoewel PbS QD filmen luminescent zijn, ondergaan ze oxidatie onder atmosferische omstandigheden, wat een blauwverschuiving van de fotoluminescentie piek veroorzaakt. Ondanks dat deze oxidatie leidt tot een finale afname van de effectieve afmeting tot ongeveer 1 nm na een maand, behouden deze filmen hun fotoluminescentie. Deze resultaten wijzen erop dat PbS QDs het geprefereerd materiaal zijn voor nabij-infrarode licht-emitterende toepassingen gebaseerd op lood chalcogenide LB filmen.

In hoofdstuk VII gebruiken we de verdienste van de excellente kwaliteit van de LB filmen om de formatie van verschillende mono- en multilagen uit QDs te bestuderen. De LB filmen worden ook gebruikt om de eigenschappen van QDs in dichtgepakte filmen te analyseren. Hierbij tonen we dat opeenvolgende samendrukking van monolagen van een variëteit aan colloïdale QDs aanleiding geeft tot een aaneenschakeling van plateaus in de $\pi - A$ isotherm. Door het gebruik van transmissie elektronenmicroscopie (TEM) en atoomkrachtmicroscopie (AFM) vinden we dat deze plateaus overeenkomen met de opeenvolgende vorming van een QD dubbel- en tripellaag. Bovendien argumenteren we dat deze transformaties in overeenstemming zijn met fase transities in de Langmuir film die kunnen begrepen worden gebaseerd op thermodynamische overwegingen. Ook vergelijken we de absorptie doorsnede van PbS en CdSe QDs in colloïdale oplossingen en in dichtgepakte lagen. We vinden dat deze vermeerderd kan worden met een factor 4 (CdSe) of 5 (PbS). Vooral in het geval van PbS QDs toont de verbetering een resonerende diameter afhankelijkheid, met een maximale waarde voor QDs van ongeveer 4 nm. Tenslotte hebben we lagen van PbSe/CdSe kern/schil QDs onderzocht met behulp van rastertunnel spectroscopie (STS) bij lage temperatuur. Hierbij tonen we aan dat de potentiaalval tussen beide potentiaal barrires eerder symmetrisch is wanneer we PbSe/CdSe kern/schil QDs bestuderen met een schildikte van 0.4 nm. Dit onthult het bestaan van een partiële schil, die zorgt voor de fluctuaties van de potentiaalval gemeten tussen de tunnel barrires, afhankelijk van

de oriëntaties die de QDs hebben aangenomen op het substraat. In hoofdstuk VIII gebruiken we opeenvolgende kationenuitwisselingsstappen voor de synthese van colloïdale PbS/CdS heterostaafjes met een hoge PLQY in het nabije IR vertrekkende van CdS kwantum staafjes. Een finale Cd/Pb partiële uitwisseling verhoogt de PLQY tot 55%. In de plaats van gewone kern/schil structuren resulteert dit in formatie van meerdere deeltje-in-staafje heterostructuren, waarschijnlijk omdat elk PbS segment in het originele kwantum staafje getransformeerd is in een enkele PbS/CdS eenheid. Het aantal PbS deeltjes in n staafje hangt af van de lengte van het originele CdS staafje. Aangezien verder afstemmen mogelijk is, toont dit aan dat kationenuitwisseling een veelzijdige benadering is voor het vormen van complexe, anisotrope heterostructuren in het IR.

List of publications

1. Geiregat P., Justo Y. and Hens Z. *Giant and Broadband Absorption Enhancement in Colloidal Quantum Dot Monolayers through Dipolar Coupling.* Submitted to ACS Nano.

2. Justo, Y., Goris, B., Kamal, J. S., Geiregat, P., Bals, S and Hens, Z. *Multiple Dot-in-Rod PbS/CdS Heterostructures with High Photoluminescence Quantum Yield in the Near-Infrared.* Journal of the American Chemical Society, **2012** *134(12)*, 5484-5487.

3. Lambert, K., Justo, Y., Kamal, J. S. and Hens, Z. *Phase Transitions in Quantum-Dot Langmuir Films.* Angewandte Chemie (International ed. in English), **2011**, *50(50)*, 12058-12061.

4. Nguyen, T., Habinshuti, J., Justo, Y., Gomes, R., Mahieu, G., Godey, S., Nys, J., et al. *Charge carrier identification in tunneling spectroscopy of core-shell nanocrystals.* Physical Review B, **2011** *84(19)*, 18.

5. Moreels, I., Justo, Y., De Geyter, B., Haustraete, K., Martins, J. C. and Hens, Z. *Size-Tunable, Bright, and Stable PbS Quantum Dots: A Surface Chemistry Study.* ACS Nano, **2011** *5(3)*, 2004-2012.

6. De Geyter, B., Justo Y., Moreels I., Lambert K., Smet P. F., Van Thourhout D., Houtepen A. J., Grodzinska D., de Mello Donega C., Meijerink A., Vanmaekelbergh D. and Hens Z. *The Different Nature of Band Edge Absorption and Emission in Colloidal PbSe/CdSe Core/Shell Quantum Dots.* ACS Nano, **2011**, *5*, 58-66.

7. Justo Y., Moreels I., Lambert K. and Hens Z. *Langmuir-Blodgett monolayers of colloidal lead chalcogenide quantum*

dots: morphology and photoluminescence. Nanotechnology **2010**, *21*, 295606.

Acknowledgments

The acknowledgments, at last!!! This is what I thought when I finished writing this manuscript and before I realized that this is actually the most difficult part to write. These have been four really intense years, during which I evolved from knowing nothing about quantum dots to know at least a little. But this would not have been possible without the help of various people and I might forget someone, so my apologies beforehand.
First of all I thank my supervisor, prof. Hens for giving the opportunity to a barely-English-speaking-Spanish-person to start this work, even if once I told you that I would be very difficult. Thanks for all your ideas, you always had an answer to all my questions that actually were a lot.
Secondly, I would like to thank Iwan for his help and support specially the first years of my PhD, certainly I could not have done this without you. Likewise, thanks to Bram, for teaching me how to synthesize PbSe QDs, for all the Physics I learnt from you and for the nice parties.
I would like to thank the members of the examination commission for the time spent reading this manuscript and for helping me improve it.
During these four years I produced a lot of mainly black samples that had to be analyzed. To do so I have been helped by a lot of people. For instance, before getting the super new photoluminescence set-up in S3, I spent innumerable amount of hours in S1 trying to see some light out of my samples. Surely, this would not have been possible without the always kind help of Prof. Smet. From the same group I would also like to thank Katleen, Nursen and Jonas Botterman specially for cooling down the Ge detector. Thanks to Prof. Van Deun and his super new photoluminescence set-up for making my life more comfortable since I don't need to go to S1 any more. Thanks to Olivier for his always perfect XRD

diffractograms and to Karen for her ICP-MS measurements that allowed me to finish that bachelor project. Also, thanks to Bart and Prof. Bals from the university of Antwerp for the always excellent HAADF-STEM images of my rods. Thanks to Prof. Vanmaekelbergh, Dr. de Mello-Donega, Dominika, Francesca and Marianna for all their kind help during my stay at the Debye Institute in Utrecht. Thanks to Hai, Gautier, Maxime, Justin and Prof. Grandidier from IEMN-CNRS in Lille, for their patience and help to perform STM and UPS measurements on an infinite amount of samples.

Thanks to Yvette, Pierre and Claudine for all the help with administrative issues. Danny and Els, for all the safety and cleanliness. Pat, for solving all the IT problems. Bart, thanks for being always there to help, even if sometimes it was a lot!

Of course I would also like to thank my colleagues, first of all to the ones who already left. Kamal and Karel, thanks for a lot of things but specially for the always nice TEM pictures. Thanks to Raquel for the perfect rods and for being such a nice workshop roommate. Thanks to Marina for allowing me to speak Spanish from time to time. Of course I would also like to thank the ones that are still here. Thanks to Stijn for the TEM pictures, thanks to Sofie also for the TEM pictures and for keeping the lab in such a good shape, thanks to Pieter G. for all your simulations, thanks to Marco for being always willing to help me and for giving me a ride when needed. Thanks to Tangi for being such a nice post-doc and for your nice beer. Thanks to Ruben for the commonly shared addiction to the m&m's during the writing of this manuscript. Thanks to Abdoulghafar for the title of this manuscript. Thanks to Chen for being the sweetest person ever. Thanks to the new generation (Pieter A. and Kim) for your youth and contagious energy. Thanks to Katrien, Marcos, Jonas, Glenn and Kenny for the awesome parties at pi-nuts.

Antti, we have been through a lot together. I would need four layers of paper to include all that I want to say but unfortunately it is not possible. However, you know it all, don't you? Thanks for supporting me, for being my best friend. During these four years I gained much more than a PhD and I hope it can last much longer.

Thanks to all my friends in Spain who I had to leave and for the new ones I made here, especially to the ones who organized that

piano concert at my place. Thanks to my really nice friend Fernando; you have been always there for me. Thanks to my family, mum, dad, sister thanks for your unconditional support (papis y Maite gracias por todo, estoy muy orgullosa de donde provengo y eso es solo gracias a vosotros). Thanks to Sandra for the huge amount of visits here. Thanks to the new family I already had but that I "gained *in-law*" during this PhD (Marisa, Pedro and Luisa) gracias por vuestro apoyo.
And last but not least, thanks to my dear Jon, thanks for standing me (not always easy), thanks for supporting me, during these four years you made me become a better person, certainly this thesis would not have been possible without you. The future, always unclear for me, looks much better when I think that I will spend it next to you, taking care of you, loving you. My friend, my family, my love ...